Università degli Studi di Napoli Federico II
Dipartimento di Fisica

PhD Program in
Novel Technologies for Materials, Sensors and Imaging
Cycle: XXVII

Femtosecond Laser Ablation of Solid Targets using Gaussian and Vortex Beams

PhD Candidate
Anoop Kiliyanamkandy

Supervisor
Prof. Salvatore Amoruso

Coordinator
Prof. Antonio Cassinese

Academic Year: 2014/2015

Femtosecond Laser Ablation of Solid Targets using Gaussian and Vortex Beams

Abstract

This thesis presents a detailed investigation of laser ablation of solid targets with femtosecond (fs) pulses, focusing on three prominent aspects: 1) spatial and temporal evolution of the laser produced plume, in high vacuum condition; 2) nanoparticles generation in high vacuum and applications of nanostructured films in material science; 3) surface micro/nanostructure formation, in ambient condition. Most of the experiments were carried out on pure copper and silicon targets, and some of the results were compared with other metals as well. While the first two investigations were performed with a standard, fs laser beam with Gaussian spatial intensity profile, material surface structuring was carried out with spatially shaped optical vortex pulses, which are recently gaining an increasing interest in the field of fs laser ablation.

The study mainly dealt with a pure copper target in both moderate (0.5–10 J/cm^2) and high fluence (0.5–75 J/cm^2) regimes. A spectrally resolved imaging technique, coupled to an intensified charge coupled device, allowed investigating the spatial and temporal evolution of different plasma plume components (ions, atoms, and nanoparticles). The analysis of the plume clearly showed the presence of a sizeable population of fast ions flying ahead of the main neutral component, which becomes still more marked in the high fluence case. A simple model indicates that the formation of the fast ion component can be explained in terms of a dynamic ambipolar diffusion process occurring in the early stage of the LPP formation. The dynamics of ions in ultrafast laser ablation of metals is studied over fluences ranging from the ablation threshold up to ≈75 J/cm^2 by means of three well-established diagnostic techniques. Langmuir probe, Faraday cup, and spectrally resolved intensified charge coupled device imaging simultaneously monitored the ions produced during ultrafast laser ablation of a pure copper target with 800 nm, ≈50 fs, Ti:Sapphire laser pulses. The fluence dependence of ion yield was analyzed, resulting in the observation of three different regimes. Multidiagnostic analysis of fs LPP over a large fluence range gave more insights onto the fundamentals of fs laser ablation, and its possibilities in numerous applications.

A combined theoretical (based on molecular dynamics calculations coupled to a two-temperature model), and experimental approach was carried out to analyze the nanoparticles component produced during fs laser ablation of a bulk copper target with ≈50 fs, 800 nm pulses, in

an interval of laser fluencies going from ≈2×F_{th} to ≈20×F_{th}. Both experimental and numerical findings agree on a size distribution characterized by a significant fraction (≈90%) of small nanoparticles, and a residual part (≈10%) spanning over a rather large size interval, evidencing a weak dependence of nanoparticles size on the laser pulse fluence. Moreover, nanoparticles generation was used to fabricate nanostructured films for applications in the field of bio-sensing, via deposition of gold nanoparticles on a quartz crystal microbalance electrode, and in photoelectrochemical cells (PEC) via deposition of TiO_2 NPs on a photoanode.

Finally, direct fs laser interaction with silicon and copper targets using optical vortex beams was investigated. Femtosecond optical vortex ablation is a powerful, novel method for material surface structuring at the micro- and nano-scale. The experimental findings suggest the importance of a cumulative and polarization effect on the formation of periodic ripples (on silicon) and interesting micro/nano patterns (on copper), which are not achievable with more standard Gaussian beams.

Table of Contents

Acknowledgements

Three beautiful years in Italy!, surely has been a fruitful period of my academic and personal life. As an international PhD student here in the department of physics, University of Naples Federico II, I believe it is my responsibility to remember and thank all the beautiful minds I met during this period. First and foremost, working with Prof. Salvatore Amoruso, my supervisor, was an unprecedented experience for me. Being his student, I consider myself one among the luckiest PhD aspirants around the world. The way he handles teaching, research, and family life with ease amazed me a lot. Without his unconditional support I would not have published 12 journal papers and one book chapter during this period. I would like to thank him from the bottom of my heart for giving me, the opportunity to be a part of his group and the freedom to pursue my research interests. The senior person in our group, Prof. Riccardo Bruzzese has always been a support to my PhD program. Even though he was not precisely my tutor, he always cared for me and enquired the status of my research on a regular basis. I express my whole hearted indebtedness for your esteemed guidance, invaluable help and fruitful suggestions during my research work. I also take this opportunity to thank Dr. Xuan Wang for introducing me to the world of programming, providing technical support for my experiments, and all your valuable suggestions during my experimental research. In addition to scientific knowledge, the characters of these three people influenced me a lot. Thank God for positioning me in this excellent group.

I must thank my PhD panel, especially from previous to present coordinators, Prof. Antonello Andreone, Prof. Luciano Lanotte and Prof. Antonio Casinesse for all your support and suggestions to improve my research. I was fortunate enough to work with many collaborators inside and outside Italy during my doctoral study. I would particularly like to acknowledge Prof. Harilal S.S for giving me an opportunity to carry out my summer internship at CUMXE, Purdue University, USA. It was truly an amazing period of my PhD program with lots of experimental research work and new experiences of American life. Timely collaboration with Dr. Giovanni Ausanio (Dipartimento di Fisica - Piazzale Tecchio), Dr. Antonio Vecchione, Dr. Rosalba Fittipaldi (CNR-SPIN Salerno), Prof. Laurent Lewis group (Université de Montréal), Dr. Xiaochang Ni (Tianjin University of Technology and Education) has been an integral part of my research outcome. Internal collaboration with other labs within the department of physics has fastened my research timeframe more than expected. I would like to express my sincere thanks to Prof. Lorenzo Marucci, Dr.

Domenico Paparo, Dr. Andrea Rubano for all their support, for our new experiments on femtosecond optical-vortex laser ablation. I extend my gratitude to *Photonics for Life Group* members (Prof. Raffaele Velotta, Prof. Carlo Altucci, Dr. Bartolomeo della Ventura, and Mr. Riccardo Funari) both for their intellectual support and cordial relationship over the years.

A Big thanks to Dr. Sharafudeen K. N, Dr. Samarth Chandra, Dr. Priya Rose for your friendship, support, and all your inspiration to pursue my PhD abroad. It was always easy for me to get recommendation letters from these close friends and eminent researchers. I specially thank Prof. Reji Philip and Mr. Jinto Thomas, with whom I started my research career at Raman Research Institute, for their guidance and inspiration to continue my research in the field of laser ablation. I also take this opportunity to thank some of my close colleagues at Raman Research institute, Dr. Benoy Anand, Dr. Ann Mary, Ms. Athira, and Mr. Shafkath for your funny and fighting relations. I also wish best of luck to these active researchers.

Friends in Naples made me very comfortable and never felt that I am away from India. Thanks to Dr. Prasanta Kumar Rath, Ms. Nivya, Mr. Jijil and Mr. Sam for your close friendship and respect. They are active science researchers and experts in food preparation, I have always been a taster of these excellent cooks. I would like to specially thank Dr. Nasim Chikhi, Mr. Mario Bianco, Ms. Simona Bianco, Mr. Nello for giving me an introduction to life in Naples and all your warm hospitality. Special thanks to all my friends from China, Mr. He Shutong, Dr. Ming, Dr. He Yuntao, Mr. Song Changbo, Mr. Yu Yue, Ms. Jing, Mr. Zhihua, and Mr. Mou Sen. I express my sincere thanks to Dr. Prasoon Diwakar, Mr. Polek for all your support for my experiments and life at Purdue university. I wish you all success in your current research and future endeavors.

Daily phone calls to my family, was an unavoidable part of my graduate study. My mother might have visited countless temples during this period to pray for my health and education. I thank her for her unconditional love and care, that I never experienced from anyone. I must thank the Italian Education Ministry for the full funding of my PhD program and it was also a partial support for my family. Last but not least, I am extremely obliged to Mr. Guido Celentano, our PhD secretary, for acting as a local guardian. Life in Naples has been easy and comfortable with his timely support.

Naples, Italy *Anoop Kiliyanamkandy*

March, 2015

Citations to Published Work

Articles in Peer-Reviewed International Journals

1. **K. K. Anoop**, Mateusz P Polek, Riccardo Bruzzese, Salvatore Amoruso, and Sivanandan S. Harilal, "Multidiagnostic analysis of ion dynamics in ultrafast laser ablation of metals over a large fluence range", J. Appl. Phys. 117, 083108 (2015).
2. B. Della Ventura, R. Funari, **Anoop K. K**, S. Amoruso, F.Gesuele, R. Velotta, and C. Altucci, "Nano-machining of bio-sensor electrodes through gold nanoparticles deposition produced by femtosecond laser ablation" (In Press, Applied Physics B: Lasers & Optics, 2015).
3. **K. K. Anoop**, A. Rubano, R. Fittipaldi, X. Wang, D. Paparo, A. Vecchione, L. Marrucci, R. Bruzzese, and S. Amoruso, "Femtosecond laser surface structuring of silicon using optical vortex beams generated by a q-plate", Appl. Phys. Lett. 104, 241604 (2014).
4. **K. K. Anoop**, R. Fittipaldi, A. Rubano, X. Wang, D. Paparo, A. Vecchione, L. Marrucci, R. Bruzzese, S. Amoruso, "Direct Femtosecond Laser Ablation of Copper with an Optical Vortex Beam " , J. Appl. Phys. 116, 113102 (2014).
5. **K. K. Anoop**, Xiaochang Ni, Salvatore Amoruso, Xuan Wang, Riccardo Bruzzese, "Fast ions generation in femtosecond laser ablation of a metallic target at moderate laser intensity", Laser Phys. 24, 105902 (2014).
6. **K. K. Anoop**, Xiaochang Ni, M. Bianco, D. Paparo, X. Wang, R. Bruzzese, S. Amoruso, "Two-dimensional imaging of atomic and nanoparticle components in copper plasma plume produced by ultrafast laser ablation" Appl. Phys. A , Volume 117 (1), 313 (2014).
7. **K. K. Anoop**, Xiaochang Ni, X. Wang, R. Bruzzese, S. Amoruso, "Spectrally Resolved Imaging of Ultrashort Laser Produced Plasma", IEEE Transactions on Plasma Science 42 (10), 2698 (2014).
8. N. Tsakiris, **K. K. Anoop**, G. Ausanio, M. Gill-Comeau, R. Bruzzese, S. Amoruso, L.J. Lewis, "Ultrashort laser ablation of bulk metallic targets: dynamics and size distribution of the generated nanoparticles", J. Appl. Phys. 115, 243301 (2014).
9. Lixia Sang, Hongjie Zhang, Xiaochang Ni, **K. K. Anoop**, Rosalba Fittipaldi, Xuan Wang, Salvatore Amoruso, "Hydrogen-evolving photoanode of TiO2 nanoparticles film deposited by a femtosecond laser" , International Journal of Hydrogen Energy 40 (1), 779 (2014).
10. Xiaochang Ni, **K. K. Anoop**, X. Wang, D. Paparo, S. Amoruso, R. Bruzzese, "Dynamics of femtosecond laser-produced plasma ions", Appl. Phys. A, Volume 117 (1), 111(2014).

11. Xiaochang Ni, Sang Li-xia, Zhang Hong-jie, **K. K. Anoop**, S. Amoruso, X. Wang, R. Fittipaldi, Li Tong, Hu Ming-lie and Xu Li-juan, "Femtosecond laser deposition of TiO2nanoparticle-assembled films with embedded CdS nanoparticles ", Optoelectronic Letters.10 (1), (2014).
12. Xiaochang Ni, **K. K. Anoop**, M. Bianco, S. Amoruso, X. Wang, Tong Li, Minglie Hu, Zhenming Song, "Ion dynamics in ultrafast laser ablation of copper target", COL 11(9), 093201 (2013).

Book Chapter

1. **K. K. Anoop**, Xiaochang Ni, Xuan Wang, Giovanni Ausanio, and Salvatore Amoruso, Chapter 5: "Ultrafast laser ablation of solid targets: A versatile method for fast ion generation and nanoparticle synthesis", in book “Laser Ablation– Fundamentals, Methods and Applications”, Christoph Gerhard, Stephan Wieneke, and Wolfgang Viöl (Eds.) Nova Science Publishers, New York (2015).

To

My Loving Parents &

Dedicated Teachers

Chapter 1

General Introduction

The laser invention is recognized as one of the greatest technological achievements of the twentieth century. The initial foundation of laser theory, i.e. stimulated emission of radiation, was laid by A. Einstein in 1917 [1]. In 1960, T. H. Maiman invented the ruby laser considered to be the first successful optical or light laser [2]. This was followed by much basic development of lasers from 1962 to 1968. Almost all important types of lasers including semiconductor lasers, Nd:YAG lasers, CO_2 gas lasers, dye lasers, and other gas lasers were invented in this era. The continuous development of lasers has been an exciting chapter in the history of science, engineering and technology. As a versatile source of highly intense, coherent, and monochromatic electromagnetic radiation, the laser has emerged as an attractive tool and research instrument with potential applications in an extraordinary variety of research and industrial fields [3].

Soon after the invention of the first working laser, it was recognized that a focused laser beam can be used as a tool for material removal. The general term used to represent this phenomenon is known as laser ablation (LA). The first published report of laser ablation came in 1962 by Breech and Cross, in which they collected and spectrally dispersed the emitted light from ruby-laser ablated metals [4]. This work is considered as the origin of the laser microprobe emission spectroscopy technique, which is used for elemental analysis of solid materials. In the same year, W.I. Linlor made measurements of the energy of ejected ions in the laser ablated material via the time-of-flight measurement method [5]. The pioneer work done by these researchers covers the fundamentals of laser ablation, whose mechanisms are still being investigated today with more sophisticated methods. Although the first phase of laser ablation study started fifty years ago, the complete understanding of laser-matter interaction is still a complex procedure because of the advances in the laser system parameters (eg. wavelength, pulse duration, repetition rate, peak power etc.), and the diverse material behavior in these new conditions. One section of this thesis work (Chapter 4) is dedicated to the characterization of laser ablation in a multidiagnostic approach.

The first decade after the invention of lasers was a the fruitful time for research involving laser matter interaction. In particular, many aspects of laser ablation were first studied, and its possible applications were introduced during this decade. More details of these early studies are reported in the books by J.F. Ready [6], J.C. Miller and R.F. Haglund [7]. One of the notable applications of

ablation, laser deposition of thin films, was first demonstrated by Smith and Turner in 1965 [8]. The thin films grown by this pulsed laser deposition (PLD) method were of poor quality compared to other established techniques at that time. So limited efforts continued into the next two decades. Then in late 1980s, PLD became rather popular because of its potential scope in complex oxide thin films research. High-temperature, superconducting, oxide thin films were fabricated via PLD, and these films showed superior quality compared with other established techniques like sputtering [9]. The details of PLD method, attractive features, and its prominent applications are featured, e.g., in a book edited by R. Eason [10, 11]. One part of my thesis work details the deposition of different types of metals, and oxide thin films via PLD with femtosecond laser pulses and its possible applications (chapter 5).

Today laser ablation is under extensive investigation as it is the basic process for many prominent laser applications. Important applications of laser ablation include deposition of nanoparticles, creation of new materials with unique physical properties, laser-induced breakdown spectroscopy (LIBS), micro/nano machining, high-precision drilling, and cutting. Even many medical applications are based on laser ablation (e.g. in ophthalmology, dermatology, surgery, etc.). A recent book edited by Claude Phipps details the mechanisms of laser ablation, and outlines many applications [12]. Traditionally, excimer lasers and Q-switched Nd:YAG lasers, with nanosecond (10^{-9} s) pulse durations, are used for laser ablation and its related applications. But in the last decades, ultrashort lasers, with pulse durations in the femtosecond and picosecond range (10^{-15} to 10^{-12} s), have shown advantages over longer, nanosecond pulses for many material processing techniques [13-16]. The following paragraphs give a brief explanation of ablation mechanisms with long and ultrashort laser pulses.

The laser pulse duration is a critical parameter in driving efficient mass removal. Fig. 1.1 shows the different stages involved in nanosecond (ns), and femtosecond (fs) laser matter interactions. Fig. 1.1(a) shows the spatial representation of ns and fs beams aiming at the sample from right to left. The common values of the laser pulse duration for commercial Nd:YAG and Ti:Sapphire lasers are 6 ns and 100 fs, respectively. At any instant, the 100 fs laser pulse is 30 μm long and the 6 ns laser pulse is 1.8 m long. In short, a nanosecond pulse is ≈60,000 times longer than a fs pulse. Fig. 1.1(b) shows the early stage of laser matter interaction: the optical penetration depths of the two lasers are different even though the sample and laser wavelengths are same. This difference is due to linear (ns) and nonlinear multiphoton absorption (fs) process occurring in the

initial stage of laser ablation. The optical penetration depth depends on the sample and laser irradiance (Energy/Area×Pulse duration). This penetrated energy becomes dissipated into different processes, including electronic excitation, ionization, heating, shock waves, and vaporization. The exact physical mechanisms, from photons to kinetic energy of vapor, photoemission (atomic, ionic, and molecular) to aerosol formation are not completely established and are still investigated theoretically and experimentally with great attention. Images in Fig. 1.1(b) show the shockwaves induced by optical absorption of a ns pulsed laser inside and outside a glass sample (top), and the transient change in nonlinear absorption induced in a transparent sample (bottom).

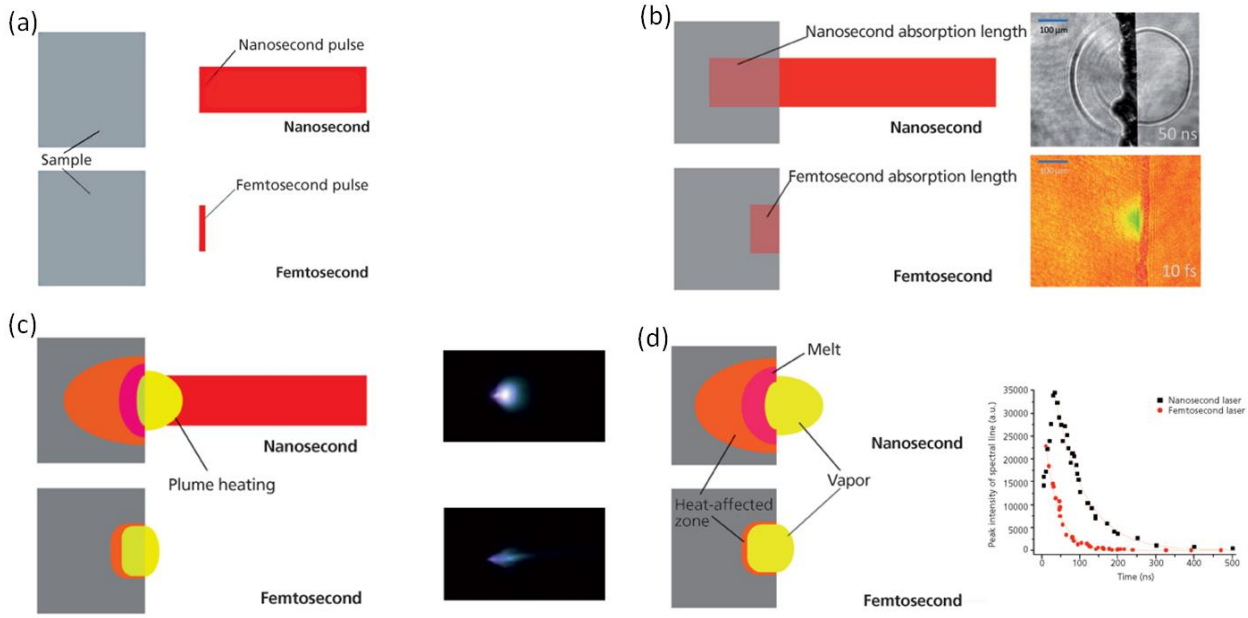

Figure 1.1: (a)-(d) The various stages of nanosecond and femtosecond laser ablation of a solid target. [Images taken from Ref. 17]

Fig. 1.1(c) shows the major difference between ns and fs laser ablation mechanisms. In the ns case, the laser-produced plasma (electrons, atoms, ions, and particles) propagates into the laser beam since it exists for longer time. The proportion of laser energy absorbed or even reflected by this plasma depends on many conditions including time, plasma temperature, electron, and mass density. The laser-plasma interaction offers a more robust, longer persistence plasma. This is the reason why ns lasers are common in LIBS applications. In fs case, the pulse duration is much shorter than the electron-to-ion energy transfer time and heat conduction time in the sample lattice, hence no laser-plasma interaction occurs. Fig. 1.1(d) represents the heat affected zone (HAZ) in both ablation mechanisms, which is proportional to square root of laser pulse duration. Graph in

Fig. 1.1(d) shows the relative decay rates of measured optical emission from ns and fs ablation having all properties equal except the pulse duration. The larger HAZ formed during ns laser ablation limits its involvement in many applications like high precision material processing, and small nanoparticle generation. The smaller HAZ in fs laser ablation indicates that a deposition of more energy per bonds, and a more efficient use of photon energy for ablation is obtained [17]. The physics of plasma plume formation, and its expansion into vacuum or into a background gas is described by several theoretical models. Thermal model is generally used for ns laser ablation [18]. The two-temperature model (TTM), molecular dynamics (MD) model, and hydrodynamic (MD) models are commonly applied to fs laser ablation [18, 19]. Since there are several physical phenomena involved in a wide range of experimental conditions, each of these models has advantages and limitations, and only combinations of these methods can describe the ablation mechanisms in a better way.

Material ablation with spatially shaped laser beams has gained considerable attention in recent years [20]. Light with orbital angular momentum (OAM) exhibits drastic differences with respect to standard Gaussian beams. Such light beams exhibit a corkscrew-like spiraling of the phase around the beam axis with no energy, that is, an optical vortex (OV). This spiraling, or twist in the wavefront, represents a fundamentally new extra degree of freedom that researchers are exploring for a variety of novel applications [20]. The ablation using this type of special beams is generally known as optical-vortex laser ablation, which is starting to show potential applications in material processing [21-23]. Micro/nanoneedle fabrication, generation of sub-wavelength surface ripples on glass and silicon targets are some of the prominent examples. Most of these studies are performed with ns OVs, while fs pulse duration experiments are still rare [23]. A section on this thesis (chapter 6) discusses the laser surface structuring of silicon and copper targets using fs optical vortex beams.

Ultrashort laser ablation (ULA) has been an intensive research area in last two decades as it is the basic process of many technological applications. Researchers have reported many of its uses and advantages over ablation with conventional nanosecond lasers [10-17]. If we go through these reports, it is clear that there are still many features to explore in fs laser ablation, from both the fundamental point of view and that of advanced applications. This thesis work is an experimental and theoretical investigation to understand more of the physics involved in ultrashort laser ablation of solid targets and its possible applications. Following section details the overview of the thesis.

1.1 Organization of the Thesis

The present thesis is an investigation of mechanisms involved in ultrashort laser ablation of solid targets, and some of its possible applications in material science. The characterization of femtosecond laser produced plasma from solid targets, and its two prominent applications, i.e. nanoparticle generation in high vacuum, and surface micro/nanostructuring in ambient conditions are greatly concerned. The thesis is divided into seven chapters and the overview is given below.

Chapter 2 reviews the previous work on ultrashort laser irradiation of solid targets. A brief theoretical explanation of ultrashort laser ablation (ULA) models, the mechanism of nanoparticle generation from ULA, and laser induced surface micro/nanostructuring are presented. The existing theoretical models are used to carry out a comparison with our experimental results.

Chapter 3 gives a general idea of three experimental techniques often employed for the above mentioned studies, and working principles of major experimental components are briefed.

Chapter 4 discusses the characterization of ultrashort laser ablation plasmas from a pure copper target, in high vacuum. The experimental results obtained from spectrally resolved ICCD imaging of the ultrashort laser produced plasma, and ion dynamics in ULA over a wide intensity range ($\approx 1\times10^{13}$ to 2.2×10^{15} W/cm^2) are carefully discussed in this chapter. The ion dynamics was studied using a negatively biased Langmuir probe and Faraday cup. A multidiagnostic analysis of laser produced plasma (LPP) from copper target gives more insights into the fundamental mechanisms involved in fs laser-matter interaction.

Chapter 5 presents different features of nanoparticle (NP) generation in ULA, and its possible applications. The expansion dynamics of the produced copper NPs plume, copper NP deposition, and NP size and shape characterization are studied as function of laser fluence. In a theoretical investigation, the ablation process of copper is studied by exploiting a hybrid atomistic-continuum model that combines molecular dynamics (MD) simulations with the two-temperature model (TTM). Numerical and experimental findings show a weak dependence of the NP sizes on the laser pulse fluence. Two examples of the characteristics of NPs-assembled films for applications in the field of bio-sensing, and photoelectrochemical cells (PEC) are also briefly explained.

Chapter 6 demonstrates the fs laser surface structuring of silicon and copper targets using optical vortex beams generated by a *q*-plate. Here, the variation of the produced surface structures is investigated as a function of the number of incident laser pulses, *N*, and laser polarization, *P*, at

laser fluences slightly above the ablation threshold value. Our experimental findings suggest the importance of laser polarization, and a cumulative effect on the formation of periodic ripples (on silicon), and interesting micro/nano patterns (on copper) which are not achievable by the more standard laser beams with a Gaussian intensity profile.

Finally, Chapter 7 summarizes the main results obtained in this thesis and proposes further experiments to explore the unanswered questions regarding ultrashort laser-matter interaction, and utilization of its possibilities in different fields of material science.

References

[1] A. Einstein, Physik. Z. 18, 121 (1917).
[2] T.H. Maiman, Nature, 187, 4736, 493-494 (1960).
[3] John C. Miller, AIP Conference Proceedings 288, 619 (1993).
[4] F. Breech and L. Cross, Appl. Spectroscopy, 16, 59 (1962).
[5] W.I. Linlor, Bull. Am. Phys. Soc., 7, 440 (1962).
[6] J.F. Ready, *Effects of High-Power Laser Radiation* (Academic Press, New York 1971).
[7] John C. Miller and Richard F. Haglund, Jr., *Laser Ablation and Desorption* (Academic Press, San Diego, CA 1998).
[8] H.M. Smith and A.F. Turner. Appl. Optics, 4, 147 (1965).
[9] Inam, A., Hedge, M. S.,Wu, X. D.,Venkatesan, T., England, P., Miceli, P. F., Chase, E.W., Chang, C. C., Tarascon, J. M., and Wachtman, J. B., Appl. Phys. Lett. 53, 908 (1988).
[10] R. Eason, *Pulsed Laser Deposition of Thin Films, Application-Led Growth of Functional Materials*, Wiley (2006).
[11] Chrisey, D. B., and Hubler, G. K. (Eds.), *Pulsed Laser Deposition of Thin Films*, Wiley Interscience, New York (1994).
[12] C. Phipps, *Laser Ablation and its Applications. Berlin,* (Germany: Springer-Verlag, 2007).
[13] S. Nolte, *"Micromachining."* In M.E. Fermann, A. Galvanauska, G. Sucha (Eds.), *Ultrafast Lasers: Technology and Applications*, pp-359-394. (New York, NY: Marcel Dekker Inc. 2003).
[14] P.P. Pronko, S.K Dutta, D. Du, R.K. Singh, J. Appl. Phys. 78, 6233 (1995).
[15] S. Eliezer, N. Eliaz, E. Grossman, D. Fisher, I. Gouzman, Z. Henis, S. Pecker, Y. Horovitz, M. Fraenkel, S. Maman, and Y. Lereah, Phys. Rev. B 69, 144119 (2004).
[16] S. Amoruso, G. Ausanio, R. Bruzzese, M. Vitiello, and X. Wang, Phys. Rev. B 71, 033406 (2005).
[17] Richard E. Russo, Xianglei Mao, Jhanis J. Gonzalez, Jong Yoo, J. Spectroscopy 28, 24 (2013).
[18] S. I. Anisimov, and B. S. Luk'yanchuk, Physics-Uspekhi 45 (3), 293 (2002).
[19] D. Perez, L.J. Lewis, Phys. Rev. B 67, 184102 (2003).
[20] Juan P. Torres and Lluis Torner (Eds.), *Twisted Photons, Applications of Light with OrbitaAngular Momentum,* (Wiley-VCH Verlag & Co. KGaA, Weinheim, Germany, 2011).

[21] Kohei Toyoda, Fuyuto Takahashi, Shun Takizawa, Yu Tokizane, Katsuhiko Miyamoto, Ryuji Morita, and Takashige Omatsu, PRL 110, 143603 (2013).
[22] Kohei Toyoda, Katsuhiko Miyamoto, Nobuyuki Aoki, Ryuji Morita, and Takashige Omatsu, Nano Lett., 12, 3645 (2012).
[23] Cyril Hnatovsky, Vladlen G. Shvedov, Wieslaw Krolikowski, and Andrei V. Rode, Optics Letters 35, 3417 (2010).

Chapter 2

A Brief Review of Femtosecond Laser Ablation

2.1 Introduction

This chapter is intended to review the mechanism of femtosecond (fs) laser-matter interaction and its potential applications in the field of thin film deposition, and material surface micro/nanostructuring. Even though the research activities to produce ultrashort laser pulses started in the first decade of laser invention [1, 2], a great improvement in ultrafast laser physics happened since 1990s with the commercialization of fs solid-state (Ti:Sapphire) lasers [3-5]. The ease of use and high optical power available from commercial solid state femtosecond lasers is leading to their increasingly widespread applications in material science, industry and medicine. We have used two commercially available solid-state lasers (Ti:Sapphire and Nd:Glass) for the experimental investigation of fs laser ablation of solid targets and its possible applications. The details of these laser systems are given in chapter 3.

The mechanism of fs laser ablation is quite different from conventional method using nanosecond lasers. As mentioned in introduction chapter, the main difference arises from the laser pulse duration, which is much less than the electron-to-ion energy transfer time and heat conduction time in the sample lattice. The following sections review the different aspects of fs laser ablation, especially mechanisms occurring during and after the laser pulse. Fig. 2.1 shows major studies carried out in my thesis work, which includes (i) the early stage mechanism of fs laser ablation, (ii) decomposition of targets, which results in nano-micro clusters and nanoparticles, (iii) fs laser induced material micro-nanostructuring. Brief theoretical notes on these mechanisms are mainly included in this chapter. Section 2.2 details the early stage processes involved in fs laser ablation and target decomposition mechanisms. The concept of two-temperature model (TTM) and molecular dynamics (MD) model are briefly explained in subsections. Section 2.3 reviews the different characterization methods used for fs laser-matter interaction, and its subsequent processes. Finally, section 2.4 reviews the mechanism of surface micro-nanostructures induced by fs laser beams.

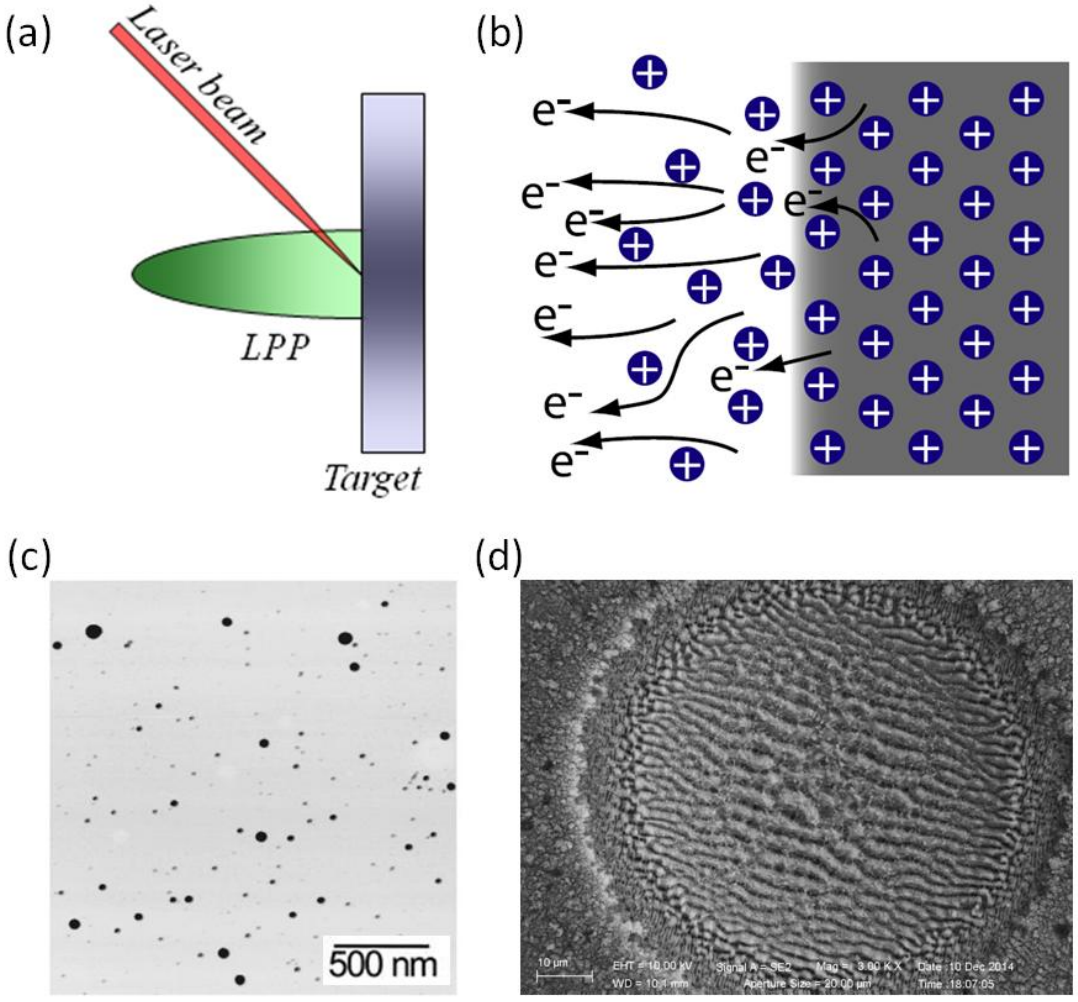

Figure 2.1: Different stages of femtosecond laser ablation studies carried out in the present thesis: (a) The basic sketch of a laser ablation process; (b) Early stage of fs laser ablation process (c); AFM image of Ag nanoparticles produced during fs laser ablation; (d) SEM micrograph of fs laser-induced periodic surface structures (LIPSSs) on silicon target [6, 7].

2.2 Mechanism of Ultrashort Laser Ablation

The term ‘‘ultrashort’’ implies that the pulse duration is shorter than the major relaxation time for electron-to-lattice energy transfer (picoseconds), heat conduction and hydrodynamic expansion in an ablation process (tens of picoseconds to hundreds of microseconds). Usually laser pulses with duration less than 1 ps come under this category. The interaction of ultrashort laser pulses with solid target is a very broad research area because of its multidisciplinary nature. The areas of physics include the interaction of electromagnetic field with solids and plasma, elements of atomic and molecular physics, plasma physics, optics, and statistical mechanics. The major theoretical concepts

of ultrashort laser ablation (ULA) explained in this section are cited from classic works of Anisimov et al. [8, 9], E.G. Gamaly et al. [10, 11], D. Perez and L. J. Lewis [12], Nolte et al. [13], and S. Amoruso et al. [14]. The major characteristics of laser-matter interaction, such as absorbed energy, ionization threshold, electron and lattice temperature, ablation rate etc. are detailed in these works. Following section describes the theoretical formulation of major mechanisms involved in fs laser-matter interaction and its comparison with experimental results.

First condition to remove an atom from a solid target by means of a laser pulse is that one should deliver energy in excess of the binding energy of that atom. With ultrashort laser pulses, the ionization threshold intensity (I_{th}) for majority of metals lies in a range 10^{13}-10^{14} W/cm^2 (λ~1 μm) with strong nonlinear dependence on intensity, and this value decreases with increase in photon energy. When a femtosecond laser pulse with $I > I_{th}$ interacts with a solid target, almost full single ionization occurs at the beginning of the laser pulse. Two major mechanisms of ionization in the moderate laser intensity regime (10^{13}-10^{14} W/cm^2) are electron impact (avalanche) ionization and multiphoton ionization [15]. Following ionization, the laser energy is absorbed by free electrons via inverse Brehmstrahlung and resonance absorption mechanisms that does not depend on the initial state of the target. Consequently, ultrashort laser matter interaction proceeds almost in a similar way for both metals and dielectrics at these intensities. The energy transfer time from the electrons to ions by Coulomb collisions is significantly longer (≥10 ps) than the laser pulse duration. Therefore, conventional laser-plasma interaction and hydrodynamic motion do not occur during the fs interaction time [15].

When the electric field of the laser pulse penetrates into a solid target, part of the incident energy is absorbed, swiftly changing the state of solid and its properties. The laser excitation affects the optical properties of a metal through the changes in the number of conductivity electrons, the electron and lattice temperature, and in the effective electron collision rate. Therefore, optical properties of a solid under the action of powerful laser pulses are time-dependent during the interaction. The laser electric field inside the solid target medium is described by well-known solution for normal skin-effect [16]:

$$E = E_0 \exp\left(i\frac{\omega\sqrt{\varepsilon}}{c}\right) = E_0 \exp\left(i\frac{\omega n x}{c} - \frac{x}{l_s}\right) \quad (2.1)$$

where $\omega = 2\pi c/\lambda$ is the laser field frequency. $\varepsilon = \varepsilon' + i\varepsilon''$; $\varepsilon^{1/2} = n + ik$; where n and k are real and imaginary parts of refractive index. The field penetration depth (absorption depth or skin-depth) l_s is inversely proportional to imaginary part of refractive index:

$$l_s = \frac{c}{\omega k} \tag{2.2}$$

Fig. 2.2(a) shows the laser electric field E penetration into the solid target in normal skin effect; the target surface corresponds to $x = 0$, and Fig. 2.2(b) represents the laser energy distribution into the target material. Typical value of skin-depth is of the order of several tens of nanometers, that comprises hundreds of atomic layers.

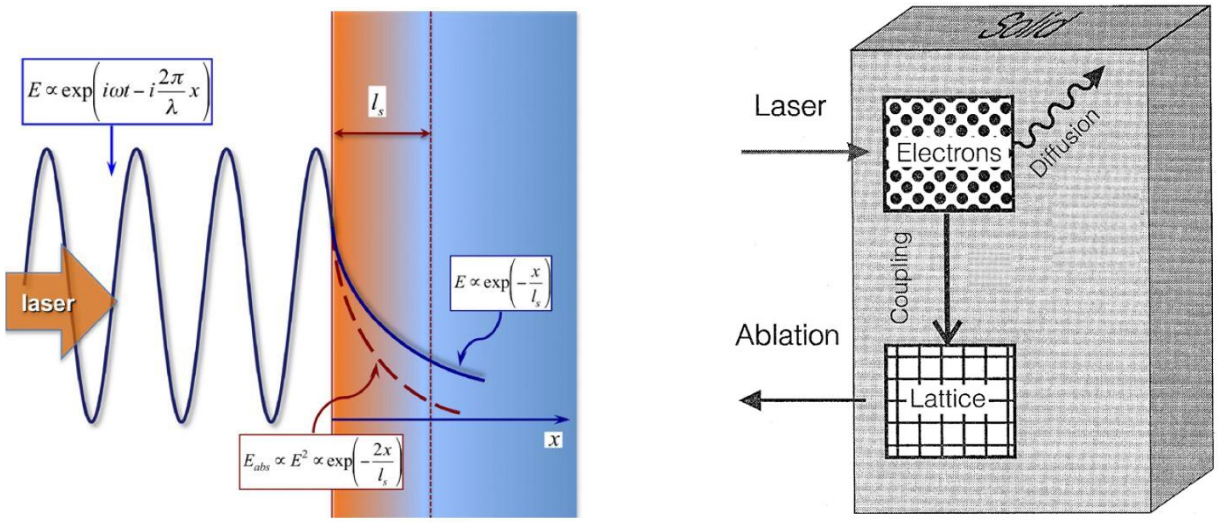

Figure 2.2: (a) Laser electric field E penetration into the solid in normal skin effect and the absorbed laser energy E_{abs} inside the skin layer. (b) Schematic drawing of the laser metal interaction. The laser energy is absorbed by free electrons. Then, energy transfer to the lattice and heat diffusion into the solid ensue [15, 17].

There are two forces responsible for momentum transfer from laser field and energetic electrons to lattice ions in the absorption zone: one is due to electric field of charge separation and another is the ponderomotive force. If the energy absorbed by the electrons exceeds the Fermi energy, which is approximately sum of binding energy and work function, the electrons can escape from the target and create a charge separation near the skin-depth layer of target. The electric field of this charge separation pulls ions out of the target thus creating an efficient non-equilibrium mechanism of ablation. At the same time, the ponderomotive force of the laser field in the skin layer pushes the electrons deeper into the target. Consequently, it creates a mechanism for ion acceleration in the target. The absorbed laser energy is transferred to the lattice on a time scale determined by the electron-phonon coupling in the target material. This quenches the electron

excitation and the lattice temperature rises. The absorption of the laser energy and redistribution of this energy as heat in the lattice under ultrashort laser ablation can be well described by the two-temperature-model [8, 9].

2.2.1 Two-Temperature Model (TTM)

The two-temperature model has been widely used to predict the electron and lattice temperature in ultrashort laser processing of solid targets [8, 9, 13, 14]. Typically laser spot diameters (tens to hundreds of microns) are much greater than the optical penetration depth and electron penetration depth (both are tens of nanometers), hence, a one-dimensional model is accurate enough to describe the physical phenomena. The energy transfer from hot electrons (at temperature T_e) to the initially cold lattice (at temperature T_i) can be described by coupled heat conduction equations as follows [8]:

$$c_e \frac{\partial T_e}{\partial t} = c_e v \frac{\partial T_e}{\partial z} + \frac{\partial}{\partial z}\left(\chi_e \frac{\partial T_e}{\partial z}\right) + Q - \mu(T_e - T_i) \tag{2.3}$$

$$c_i \frac{\partial T_i}{\partial t} = c_i v \frac{\partial T_i}{\partial z} + \frac{\partial}{\partial z}\left(\chi_i \frac{\partial T_i}{\partial z}\right) + \mu(T_e - T_i) \tag{2.4}$$

Here, c_e and c_i are the specific heat capacities [J cm^{-3} K^{-1}] of the electrons and lattice, respectively, χ_e and χ_i are the corresponding thermal conductivity coefficients, and the parameter $\mu = c_e/\tau$ characterizes the rate of energy exchange [W cm^{-3} K^{-1}] between electron and lattice systems (τ is the characteristic exchange time for electron subsystems), and the ablation front travels with a velocity v relative to the immobile material. The absorption of laser energy by electrons is described by the equation,

$$Q = -\frac{\partial I}{\partial z} = \alpha I, \quad I(0,t) = I_s(t) \tag{2.5}$$

where α is the absorption coefficient, and $I_s = A \times I(t)$ is the absorbed laser intensity at the metal surface ($z = 0$), and $A = (1-R)$ is the absorptivity of the material (R is the radiation reflection coefficient). For the model to be suitable for the analysis of experimental data, account must be taken of the temperature dependences of the coefficients c_e, c_i, χ_e, χ_i, A, α, and μ. To find the temporal variation of T_e and T_i the above coupled differential equations can be solved numerically and under certain assumptions, analytical solutions can also be found. Fig. 2.3 is an example of

such calculation performed for the ablation of copper target irradiated by a 120 fs, 800 nm pulse at a laser intensity $I_0 = 5\times10^{12}$ W/cm^2 [13, 17-19].

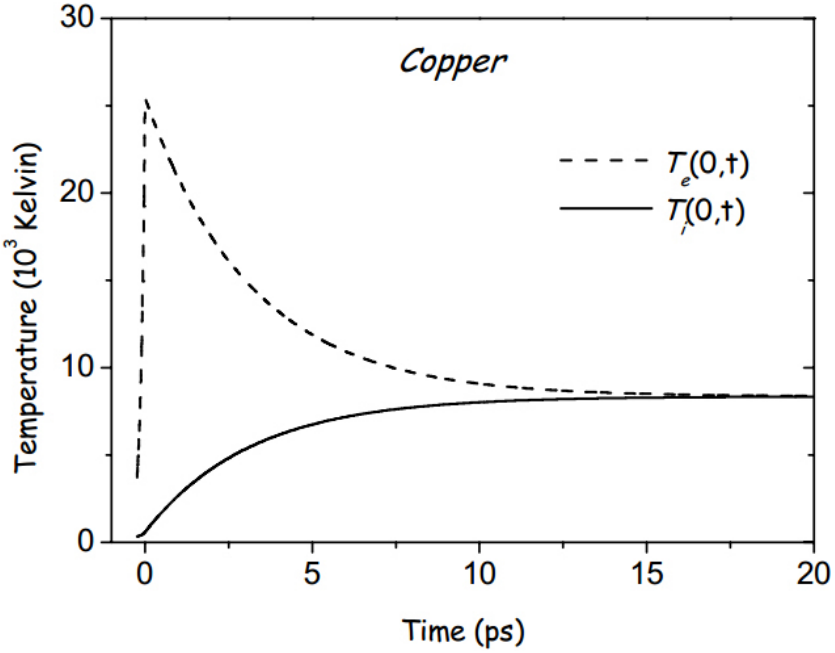

Figure 2.3: Temporal distribution of electron (T_e) and lattice (T_i) surface temperature for a copper target irradiated by a 120 fs, 800 nm pulse at a laser intensity $I_0 = 5\times10^{12}$ W/cm^2 [18].

From this calculation, it can be seen that the electrons are subject to an extraordinary heating rate while the lattice remains comparably cold in the early stages. After a period of time which is determined by energy transfer time between electrons and the lattice, the lattice temperature increases as energy is acquired from the excited electrons. The electron excitation is reduced while the lattice reaches the melting point (T_m = 1357 K) after which the temperature increases and becomes approximately equal to the electron temperature at ~15 ps. Several researchers have predicted the amount of material removed during ablation by using the TTM. An ablation criterion often used is that the lattice energy must exceed the heat of vaporization, $c_i T_i > \rho\Omega_{vap}$ where ρ and Ω_{vap} are the density and enthalpy of vaporization of the target material. Nolte et al. proposed a solution to the TTM of heat diffusion [13], which yields a logarithmic dependence of the ablation depth on the applied laser fluence. For low fluence, where the depth is determined by the optical penetration of the laser, the ablated depth per pulse is given by:

$$d_{opt} = l_s \ln\left(\frac{F}{F_{th}}\right) \tag{2.6}$$

where l_s is a the optical absorption depth and F_{th} is the threshold fluence for ablation. At higher fluence, electronic heat conduction becomes significant and the ablation depth is described by:

$$d_{heat} = l \ln\left(\frac{F}{F_{th}}\right) \tag{2.7}$$

here l is the heat penetration depth, which is related to electron thermal conductivity. These two different regimes in the dependence of the ablation depth/yield on the laser fluence (see Fig. 2.4) have been frequently reported by several experimental investigations [13, 14, 19] and are also a topic of discussions in chapter 4 of the present thesis. A comprehensive study on ablation of copper targets by femtosecond and by picosecond laser pulses is presented by Nolte et al. [13]. The combined theoretical and experimental investigations done in this pioneer work are compared with our experimental results, obtained from ultrafast laser ablation of a copper target with 800 nm, ≈50 fs, Ti:Sapphire laser pulses at moderate laser intensity (Section 4.1).

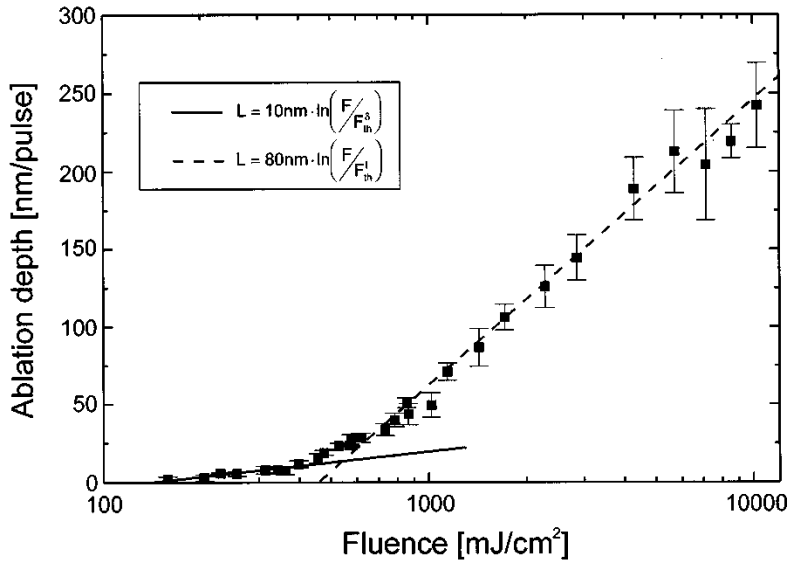

Figure 2.4: Ablation depth per pulse for copper versus the incident laser fluence, for 150-fs laser pulses. The solid and the dashed lines represent the best fits according to Eqs. (2.6) and (2.7) [13].

Even though TTM has been widely used to predict the electron and phonon temperature distributions in ultrashort laser processing of metals, estimations of some important thermal and optical properties in the existing TTM are limited to low laser fluences in which the electron temperatures are much lower than the Fermi temperature [20-22]. So researchers are focusing on improved two-temperature models for better prediction of ultrashort laser ablation process [23].

More complicated modeling can be undertaken in the form of hydrodynamic [24-27] or molecular dynamic (MD) simulations [12, 14, 28, 29] of the ablation process. Hydrodynamic (HD) calculations treat a large scale system through knowledge of the material's equation of state whereas molecular dynamic calculations consider an atomistic system where position, velocity and force between atoms at each time step is calculated. Both are computationally expensive, especially the MD simulations, but can give a deeper insight into the ablation process and the nature of the ablation products which is considerably different when compared to nanosecond laser ablation. In some cases, combination of these models can give better understanding of processes involved in ultrafast laser ablation of solid targets. In the following section, molecular dynamics simulations with two-temperature model (MD-TTM), describe the decomposition of the material through the analysis of the evolution of thermodynamic trajectories in the material phase diagram, and allow estimating the size distribution of the generated nano-aggregates.

2.2.2 Relaxation Dynamics of the Excited Target Material

The transient two-temperature system (hot electrons and cold lattice) developed during fs laser irradiation will tend to reach equilibrium within a few picoseconds through electron-phonon interaction and electron diffusion out of excited region [13, 30-32]. When the lattice temperature is elevated high enough, material ablation starts via different mechanisms. The origin of these mechanisms mainly depends on the thermodynamics relaxation path (phase diagram or thermodynamic trajectory) followed by the material under intense fs laser irradiation. Since the ablation process starts at a few tens of picoseconds and lasts within several nanoseconds, most of the studies carried out in these fields are theoretical. The ablation of solids under fs laser pulses, especially its relaxation dynamics has been extensively studied using molecular dynamics (MD) method [12, 14, 28, 29, 33-35], Direct Simulation Monte Carlo (DSMC) method [36-38], combined MD-DSMC method [39], Combined molecular dynamics-two temperature model (MD-TTM) [40, 41], and hydrodynamics (HD) method [8, 24-27, 42, 43]. Perez and Lewis developed a MD simulation, which shows that ablation involves four different processes-(I) spallation, (II) homogenous nucleation, (III) fragmentation, and (IV) vaporization-depending on the thermodynamic trajectories followed by different regions of the target at given laser intensity [12, 29]. Fig. 2.5 shows the typical thermodynamic trajectories occurring in different regions of a solid target. Roman numerals in Fig. 2.5 represent the mechanism in the corresponding thermodynamic

trajectory. Depending on the incident laser intensity, some of the above mechanisms may predominate in the decomposition mechanism and subsequent plume evolution, or all these mechanisms can occur simultaneously at different portions under the surface of the target. The origin and consequences of each of these mechanisms are comprehensively discussed in several reports [12, 14, 28, 29, 33-35]. The MD simulations done by these authors reveal the exact mechanisms of nanometer-sized particle generation from fs laser ablation.

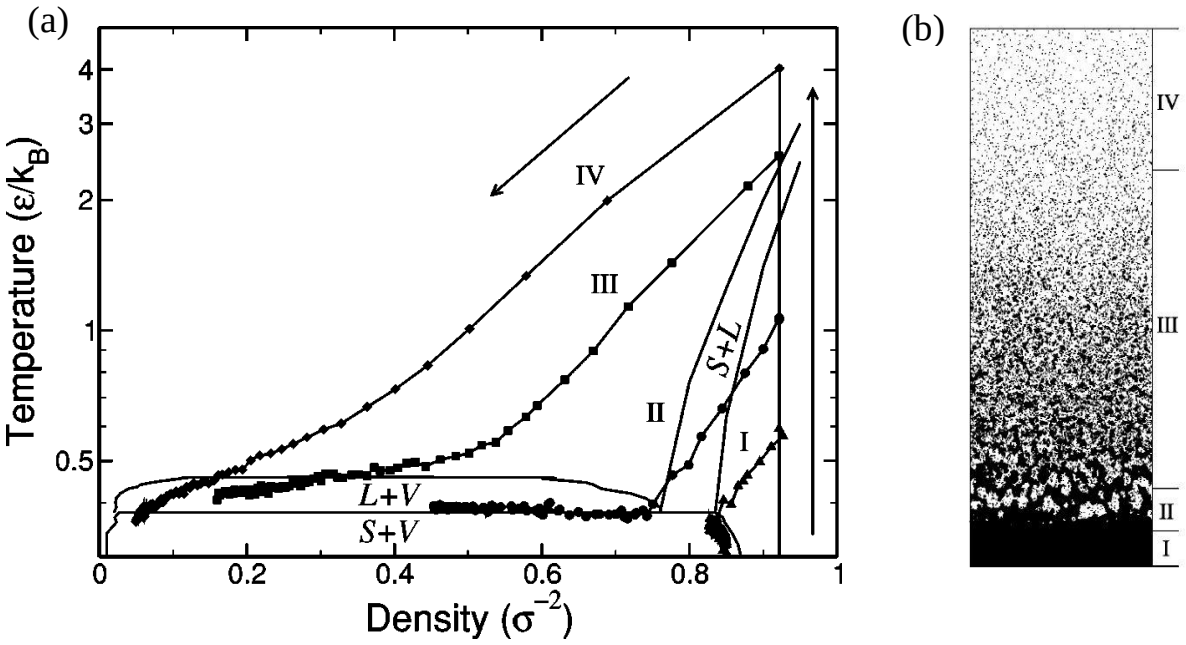

Figure 2.5: (a) Schematic temperature-density diagram of a material, and thermodynamic pathways following ultrashort laser irradiation in different regimes. S+L, S+V, L+V are the solid-liquid, solid-vapor, and the liquid-vapor coexistence regions, respectively. The vertical solid line indicates the isochoric heating occurring at near-solid density. Once heated up at a certain temperature, the material relaxes following a thermodynamic pathway depending on the initial temperature. In the figure four qualitative pathways corresponding to spallation (I), phase explosion (II), fragmentation (III), and vaporization (IV), respectively, are reported [From Ref. 12, 29]. These mechanisms results in a material blow-off composed of neutral atoms, ions, clusters, and nanoparticles of the target material. Arrows indicate the flow of time. (b) Visual plot of MD simulation of target decomposition during fs laser ablation showing how different regions in the target are subject to different decomposition mechanism [12].

In addition to MD method, many reports have been published on material decomposition in fs regime using hydrodynamic model with thermodynamically complete set of equations [8, 24-27, 42, 43]. Compared to MD method, HD model allows calculations for much larger systems and take much shorter computer processing time. According to this model, a major fraction of the ablated material is found to originate from the metastable liquid region, which is decomposed either thermally in the vicinity of the critical point into a liquid-gas mixture or mechanically at high strain

rate and negative pressure into liquid droplets and chunks [44]. The results obtained in this method are in agreement with MD method and can explain recent experimental findings [44]. The plume of the ablated target material is composed of neutral atoms, ions, nanoparticles, and clusters depending on the laser irradiation parameters, nature of target material, and ambient condition. The vacuum expansion of the laser-produced plasma (LPP) plume could be described by means of the three-dimensional hydrodynamic model proposed by Anisimov et al. [8, 45, 46]. This model is based on the solution of the gas-dynamic equations by assuming an adiabatic and isentropic expansion of the plasma plume into vacuum and allows an estimation of several key parameters such as kinetic energy (temperature) of the species and plume divergence. This model was basically developed for the expansion of a neutral gas cloud generated by nanosecond laser ablation in vacuum, but it has also been successfully used to describe the expansion of both the plasma part [47] and the overall plume (ions and neutrals) [48] for ns LPP. By comparing the expansion velocity and the rate of heat diffusion in a LPP, Lunney et al. [49] estimated that when the electron temperature is less than ~12 eV the expansion is isentropic. Since the plasma temperatures encountered during fs laser ablation is less than this value, this model has been applied in ultrafast laser ablation regime as well [47, 50, 51]. We have used this model in chapter 4 of the present thesis to explain the angular distribution of ions produced during femtosecond laser ablation of a copper target in high vacuum condition.

Multi-scale approach based on the combination of two methods (eg. MD-TTM and MD–DSMC) was developed by several groups and has shown a better agreement of predictions with experimental results in describing the evolution of a metallic target following irradiation by an intense, ultrashort laser pulses [39-41]. In order to study the dependence of nanoparticle size distribution on laser fluence in the moderate laser intensity, we have done MD-TTM simulations of fs laser ablation of copper target (in collaboration with Lewis et al.) and compared with experimental results obtained in our laboratory [52]. In this method, the MD part is responsible for handling the forces among the atoms at all times during the simulations. The TTM part, on the other hand, uses the coupling of electrons and phonons in order to calculate the transfer and diffusion of the energy to the lattice, during and after irradiation. These two methods, combined, allow for a strict and well-defined description of the laser ablation problem. In particular, MD simulations coupled to thermodynamic trajectory analysis allow one to follow the target decomposition history through both visual inspection of the simulated cell and material state evolution in the phase

diagram. The details of this MD-TTM method, i.e. phase diagram of copper target, size distribution and velocity distribution of ablated material under fs laser irradiation are comprehensively discussed in chapter 5.

2.3 Characterization Methods

Since fs laser ablation and its subsequent processes play a prominent role in many technological applications, the characterization of all the underlying phenomena is very important. Optical emission spectroscopy (OES) [54], fast gated intensified charge coupled device (ICCD) imaging [55, 56], probe diagnostic [48, 50, 57-60], shadowgraphy [61, 62], microwave and laser interferometry [63-65], laser-induced fluorescence [66], inductively coupled plasma mass spectroscopy (ICP-MS) [67], optical absorption spectroscopy [68, 69], pump probe method [70], and streak camera [71] are some of the well established techniques used for laser-induced plume diagnostics. In addition to these techniques, recently K. Goda et al. introduced serial time-encoded amplified imaging/microscopy (STEAM) for real-time observation of ultrafast dynamic phenomena [72]. This method can perform continuous real-time imaging at a frame speed of 163 ns (a frame rate of 6.1 MHz) and a shutter speed of 440 ps. They demonstrated the real-time imaging of microfluidic flow and phase-explosion effects that occur during laser ablation [72]. The latest development in this field is sequentially timed all-optical mapping photography (STAMP), introduced by K. Nakagawa et al. [73]. This photography method enables real-time visualization of ultrafast dynamical phenomena that are non-repetitive or difficult to reproduce with equally short frame intervals (4.4 trillion frames per second) and high pixel resolution (450 × 450 pixels). They used it to capture plasma dynamics and lattice vibrational waves, both of which were previously difficult to observe with conventional methods in a single shot and in real time [73]. The other methods used for the characterization of subsequent processes of ultrafast laser ablation (i.e. nanoparticle generation, material surface micro/nanostructuring etc.) are atomic force microscopy (AFM) [52, 53, 74], white light interferometric microscope [67], X-ray diffraction (XRD) [53, 74], X-ray photoelectron spectroscopy (XPS) [74], atomic absorption, emission and fluorescence techniques [74], scanning electron microscope (SEM) [74, 75].

The characterization of fs LPP plume in our experimental conditions is done using four of the above-mentioned techniques. Langmuir probe (LP), Faraday cup (FC), Optical emission spectroscopy (OES), and spectrally resolved intensified charge coupled device (ICCD) imaging

simultaneously monitored the plume produced during ultrafast laser ablation of a pure copper target with 800 nm, ≈50 fs, Ti:Sapphire laser pulses. LP and FC are mainly used in ion dynamics studies, while OES and spectrally resolved ICCD imaging are used for spatial and temporal evolution of atomic components (neutrals and ions) in the LPP. The direct ICCD imaging was used for nanoparticle emission dynamics in fs laser ablation. The details of these sophisticated equipments, and of their use are comprehensively discussed in chapter 3 and chapter 4, respectively. In addition to the characterization of early stage mechanisms in LPP, we have also dealt with two prominent applications of fs laser ablation in the present thesis, i.e. nanoparticle generation in high vacuum, and surface micro/nanostructuring in ambient condition. The characterization of nanoparticle generation, i.e. size distribution, thickness of NP assembled films was done using atomic force microscopy (AFM), morphology of laser induced surface micro/nano structures was recorded using a high resolution field emission scanning electron microscope (FESEM). The basic working principles of AFM and FESEM systems are mentioned in chapter 3, while micrographs of nanoparticle deposition and laser-processed surfaces are discussed in chapters 5 and chapter 6, respectively.

2.4 Micro/Nanostructuring with Femtosecond Laser Beams

Surface morphology plays an important role in controlling optical, mechanical, chemical, biological, and other properties of a solid surface. Recently, fs laser induced surface structuring has emerged as a versatile tool for fabricating a large variety of micro/nano structured materials suitable for a wide range of applications in photonics, plasmonics, optoelectronics, biomedicine, and other areas [76]. The material micro/nano fabrication can be done in different ways with fs lasers. The techniques like nanostructuring by deposition from fs laser ablation plume, direct femtosecond laser ablation, mask projection technique, near field ablation, laser-assisted chemical etching, nanostructuring of thin metal films by fs laser-induced melt, plasmonic nanoablation, and interferometric fs laser ablation have been developed for surface nanostructuring [76]. Among these, direct fs laser ablation gained considerable attention because of its ability to produce nearly all types of material (including metals, semiconductors, glasses, and polymers), capacity of processing non-planar surfaces, ability to produce variety of surface structures in micro and nano scales, and since it is a maskless single-step process at high speed under normal ambient conditions. All these features make direct fs laser ablation a powerful technique for producing a large variety of

surface structures suitable for a wide range of applications [76-95]. The most notable examples in this field are fabrication of black silicon [85], colored silicon [86], black and colored metals [77, 87, 88], and material with strong hydrophobicity [89], hydrophilicity [90], superwicking effect [91], super wetting [92], significant enhancement of X-ray generation and temperature of plasma hot electrons [93], photoelectron emission [94], and thermal radiation from incandescent light sources [95].

The physical processes underlying fs laser ablation have been discussed in the above sections of this chapter. Following ablation, the sample surface cools down to room temperature at very high rate of about 10^{13}-10^{15} K/s [96] and rapidly re-solidifies to give rise to surface structures. The morphology of laser-induced surface structures depends on laser parameters, ambient condition and material properties. Micro/nanoscale surface structures fabricated by direct fs laser processing can generally be grouped into following four categories: (1) laser-induced periodic and quasi-periodic structures, (2) various controlled irregular nanostructures, (3) nanostructure-textured microstructures, (4) single nanoholes and arrays of nanoholes. Among these, first three types of structures induced by fs vortex pulses are greatly concerned in chapter 6 of the present thesis. Figure 2.6 (b)-(f) shows examples of different micro/nano structures fabricated in our laboratory. In the following section, the formation mechanisms of these structures are discussed in detail.

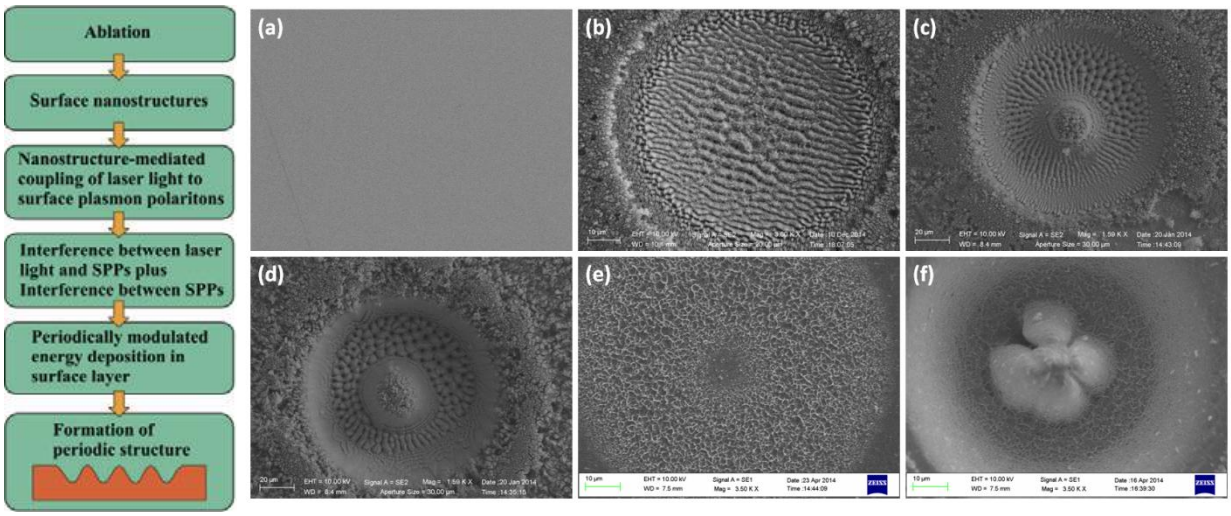

Figure 2.6: Processes involved in fs laser-induced periodic surface structuring (FLIPSS) [left] and different types of micro/nanostructures developed in our laboratory [right]. (a) Silicon surface before laser irradiation (b)-(d) periodic and columnar structures on silicon surface with Gaussian and vortex laser beams. (e)-(f) various controlled irregular micro/nanostructures on copper surface with optical vortex beams. The details of these micro/nanostructures are explained in chapter 6.

Laser-induced periodic surface structures (LIPSSs) are one of the most actively studied surface structures. LIPSS were first observed by Birnbaum, in 1965, on semiconductors following ablation by a ruby laser [97]. The LIPSSs fabricated using long-pulsed (>5 ps) lasers were extensively studied by several authors [98-100]. The typical period of these LIPSSs or surface ripples is of the order of incident laser wavelength and oriented perpendicular to the polarization of laser beam. The formation mechanism of these LIPSSs on metal surface is often explained by the interference between incident laser light and excited surface plasmon polaritons (SPPs) that results in spatial energy distribution on the surface. Following Bonch-Bruevich et al., for a linearly polarized laser light, the period *d* of the LIPSSs on a metal in a dielectric medium is given by [100]

$$d = \frac{\lambda_{las}}{(Re\,[\eta] \mp sin\theta)} \quad \text{with } \mathbf{g}||\mathbf{E} \tag{2.8}$$

where λ_{las} is the incident laser wavelength, θ is the angle of incident light, $\eta = [\varepsilon_d \times \varepsilon_{metal} / \varepsilon_d + \varepsilon_{metal}]^{1/2}$ is the effective refractive index of the dielectric-metal interface for surface plasmons. ε_d is the dielectric constant of the ambient dielectric medium, ε_{metal} is the dielectric constant of the metal, Re[η] is the real part of η, **g** is the grating vector, and **E** is the tangential component of electrical field vector of the incident laser light. The similar structures with more precision and size control can be fabricated using fs laser, which are generally known as fs laser-induced periodic surface structures (FLIPSSs). Fig. 2.6 shows the basic mechanism of FLIPSS formation and some periodic structures [(b) and (c)] obtained in our experiments. Usually, the first few laser shots ($N \approx 10$) produce sparsely and randomly distributed nanostructures on metal surafce. It is known that surface nanoroughness on a metal surface can couple free space light to surface plasmon polaritons (SPPs) due to diffraction [101]. Then, the next laser pulses couple to SPPs via previously produced nanostructures. The interference between the linearly polarized laser light and SPPs causes a periodic spatial modulation of the energy deposited into the irradiated sample [102]. This leads to spatially modulated heating of the surface and formation of the periodic structure. In many applications, it is very important to control the period of these surface structures. This can be achieved (following Eq. 2.8) by changing the incident laser wavelength, incident angle, or the real part of the effective refractive index. Numerous studies have been published in these areas and the obtained results indicate the versatility of direct fs laser surface structuring in a wide range of applications [76-95]. The most notable example is the generation of high and low spatial frequency

FLIPSSs, which is generally represented as HSFLs and LSFLs, respectively. The formation mechanism of LSFLs with period close to laser wavelength are well described by classical interference model [100] and the HSFLs which is observed in many works [76, 79, 81, 82], with period much smaller than laser wavelength can be described by polariton model [103]. This model considers the interference between SPPs and also the interference between spatial harmonics of SPPs [104] for sub-wavelength ripple formation. The self-organization from a laser-induced surface instability [105–107] and second harmonic generation [108, 109] are other proposed models for the HSFLs formation. These models are also appropriate to explain the ripple formation mechanisms in semiconductors and dielectrics because of the similar behavior of these materials under intense fs laser pulses. The other surface structures like various controlled nanostructures [77, 78, 87, 110, 111], nanostructure-textured micro-structures [112-115] on metals, semiconductors, and dielectric have been observed in many works, and is also a topic of discussion in chapter 6 of the present thesis. Though impressive technological applications have been made so far with direct fs laser surface structuring, the complete mechanisms of these surface structure formation in micro/nanoscale are not yet completely understood, and research still continues.

Most of the studies performed in this area are carried out by using standard laser beams with a Gaussian intensity profile. Recently laser ablation with spatially shaped beams has gained considerable interest in material processing applications [116-122]. Most remarkable example is material surafce processing in micro/nanoscale using optical vortex pulses [116, 117]. Optical vortices (OVs) represent a special type of beam carrying orbital angular momentum (OAM) with a twist in wavefront and a point of zero intensity at centre. Omatsu et al. carried out laser ablation of Ta plates using nanosecond optical vortex pulses, for the first time [116]. They demonstrated that owing to OAM of optical vortex, clearer and smoother processed surfaces were obtained with lower ablation threshold fluence, in comparison with the ablation by a nonvortex annular beam modified from a spatially Gaussian beam. They also demonstrated micro-nanoneedle fabrication using laser ablation by nanosecond twisted light with spin. The resulting needle showed a height of at least 10 μm above the target surface and a tip diameter of less than 0.3 μm. The total angular momentum of the twisted light determines the structure of the needle on the processed surface. These fabricated needles can be used to visualize the helicity of an optical vortex. The orbital angular momentum of light determines the chirality of the nanoneedles, since it is transferred from the optical vortex to the metal. Femtosecond OV beams have been used for inducing sub-wavelength ring structures on

glass or silicon surfaces, [117, 118] and the fabrication of graphene micro- and nano-disks [119]. Moreover, the generation of surface ripples has been recently used to analyze the focal intensity distribution and/or polarization structure of optical vortex beams by irradiation of polished target surfaces (silicon and steel), with a fixed number of laser pulses (N = 100) [120, 121]. Several mechanisms have been considered for ripples formation by fs laser pulse irradiation with Gaussian beams. These include excitation of surface plasmon polaritons (SPPs), self-organization of surface instabilities, second-harmonic generation, etc., but no general consensus has been reached until now [76, 122, 123]. However, OVs with fs pulse duration are seldom used for laser ablation and material processing [117]. The present thesis investigate these mechanisms in details (chapter 6) when using a fs optical vortex beam generated via spin-to-orbital conversion of the angular momentum of light by using a *q*-plate [124]. Periodic surface structures, various controlled irregular structures, columnar structures on silicon and copper targets in micro/nanoscale are fabricated and thoroughly investigated.

References

[1] Hargrove L E, Fork R L and Pollack M A, Appl. Phys. Lett. 54 (1964).
[2] Yariv A, Appl. Phys. 36, 388 (1965).
[3] P. F. Moulton, Chapter "*Recent advances in transition-metal-doped lasers*," in *Tunable Solid State Lasers*, Springer Series in Optical Sciences, P. Hammerling, A. Budgor, and A. Pinto, eds. (Springer-Verlag, Berlin, 1985).
[4] P. F. Moulton, J. Opt. Soc. B, vol. 3, p. 125 (1986).
[5] P M W French, Rep. Prog. Piiys. 58, 169-267 (1995).
[6] P Balling and J Schou, Rep. Prog. Phys. 76, 036502 (2013).
[7] S. Amoruso, G. Ausanio, R. Bruzzese, M. Vitiello, and X. Wang, Phys. Rev. B 71, 033406 (2005).
[8] S.I. Anisimov, B.S. Luk'yanchuk, Physics - Uspekhi 45 (3) 293 (2002).
[9] S. I. Anisimov, B. L. Kapelovich and T. L. Perel'man, Zh. Eksp. Teor. Fiz, 66, 779 (1974).
[10] E. G. Gamaly, A. V. Rode, B. Luther-Davies, and V. T. Tikhonchuk, Physics of Plasmas 9, 949 (2002).
[11] E.G. Gamaly, Physics Reports 508, 91–243 (2011).
[12] D. Perez, L.J. Lewis, Phys. Rev. B 67, 184102 (2003).
[13] S. Nolte, C. Momma, H. Jacobs, A. Tünnermann, B. N. Chichkov, B. Wellegehausen, and H. Welling, J. Opt. Soc. Am. B 14 (1997).
[14] S. Amoruso, R. Bruzzese, X. Wang N.N. Nedialkov, P.A. Atanasov, J. Phys. D 40, 331 (2007).

[15] E.G. Gamaly, *Femtosecond Laser-Matter Interaction: Theory, Experiments and Applications*, (Pan Stanford Publishing, Singapore, 2011).
[16] Landau, L.D., Lifshitz, E.M., Pitaevskii, L.P., *Electrodynamics of Continuous Media*, (Pergamon Press, Oxford, 1984).
[17] C. Momma, S. Nolte, B. N. Chichkov, F. v. Alvensleben, A. Tünnermann, Applied Surface Science 109/110, 15-19 (1997).
[18] Marco Vitiello, *Ultrashort pulsed laser ablation of solid targets*, PhD thesis, University of Naples Federico II (2005).
[19] K. Furusawa, K. Takahashi, H. Kumagai, K. Midorikawa, M. Obara, Appl. Phys. A 69 [Suppl.], S359–S366 (1999).
[20] Ashcroft, N. W., and Mermin, N. D., *Solid State Physics*, Holt, Rinehart, and Winston, New York (1976).
[21] Kittel, C., *Introduction to Solid State Physics*, J Wiley, NY (1986).
[22] Qiu, T. Q., and Tien, C. L., *"Short-Pulse Laser Heating on Metals",* Int. J. Heat Mass Transfer, 35, 719 (1992).
[23] Lan Jiang and Hai-Lung Tsai, Journal of Heat Transfer 127, 1167 (2005).
[24] M. E. Povarnitsyn, T. E. Itina, M. Sentis, K. V. Khishchenko and P. R. Levashov, Phys. Rev. B, 75, 235414 (2007).
[25] A.M. Komashko, M.D. Feit, A.M. Rubenchik, M.D. Perry, and P.S. Banks, Appl. Phys. A 69, S95 (1999).
[26] K. Eidmann, J. Meyer-ter-Vehn, and T. Schlegel and S. Huller, Phys Rev. Lett., 62, 1202 (2001).
[27] F. Vidal, T. W. Johnston, S. Laville, O. Barthélemy, M. Chaker, B. Le Drogoff, J. Margot, and M. Sabsabi, Phys Rev. Lett., 86, 2573 (2000).
[28] C. Cheng and X. Xu, Phys. Rev. B, 72, 165415 (2005).
[29] D. Perez and L. J. Lewis, Phys. Rev. Lett., 89, 255504 (2002).
[30] G. L. Eesley, Phys. Rev. Lett. 51, 2140–2143 (1983).
[31] J. G. Fujimoto, J. M. Liu, and E. P. Ippen, Phys. Rev. Lett. 53, 1837–1840 (1984).
[32] H. E. Elsayedali, T. B. Norris, M. A. Pessot, and G. A. Mourou, Phys. Rev. Lett. 58, 1212–1215 (1987).
[33] Zhigilei, LV; Garrison, BJ. Appl. Phys. Lett. 74, 1341 (1999).
[34] Itina, TE; Zhigilei, LV; Garrison, BJ. J. Phys. Chem. B, vol. 106, 303-310 (2002).
[35] Itina, TE; Zhigilei, LV; Garrison, BJ. Nuclear Instr. & Methods in Phys. Res. B , Beam Interaction with Materials and Atoms, 2001, vol. 180, 238-244 (2001).
[36] Itina, TE; Marine, W; Autric, M. J. Appl. Phys., vol. 82(7), 3536 (1997).
[37] Itina, TE; Hermann, J; Delaporte, P; Sentis, M. Phys. Rev. E, vol. 66, 066406 (2002).
[38] Itina, TE; Tokarev, VN; Marine, W; Autric, M. J. Chem. Phys., vol. 106(21), 8905 (1997).
[39] Tatiana E. Itina, Karine Gouriet, Leonid V. Zhigilei, Sylvie Noël, Jörg Hermann, Marc Sentis, Applied Surface Science 253, 7656–7661 (2007).
[40] M. Gill-Comeau and L. J. Lewis, Phys. Rev. B 84, 224110 (2011).

[41] D. S. Ivanov and L. V. Zhigilei, Phys. Rev. B 68, 064114 (2003).
[42] J. P. Colombier, P. Combis, F. Bonneau, R. Le Harzic, and E. Audouard, Phys. Rev. B 71, 165406 (2005).
[43] T.E. Glover, J. Opt. Soc. Am. B 20, 125 (2003).
[44] Tatiana E. Itina, Mikhail E. Povarnitsyn and Konstantin V. Khishchenko, chapter "Modeling of laser ablation induced by nanosecond and femtosecond laser pulses" in "*Laser Ablation: Effects and Applications*", Sharon E. Black (Ed.), Nova Science Publishers, Inc., New York (2011).
[45] S. I. Anisimov, D. Bauerle, and B. S. Luk'yanchuk, Phys. Rev. B 48, 12076 (1993).
[46] S. I. Anisimov, B. S. Luk'yanchuk, and A. Luches, Appl. Surf. Sci. 96-98, 24 (1996).
[47] T. N. Hansen, J. Schou, and J. G. Lunney, Appl. Phys. A: Mater. Sci. Process. 69, S601 (1999).
[48] B. Toftmann, J. Schou, and J. G. Lunney, Phys. Rev. B 67, 104101 (2003).
[49] J. G. Lunney, B. Doggett, and Y. Kaufman, J. Phys.: Conf. Ser. 59, 470 (2007).
[50] T. Donnelly, J. G. Lunney, S. Amoruso, R. Bruzzese, X. Wang, and X. Ni, J. Appl. Phys. 108, 043309 (2010).
[51] K. K. Anoop, X. Ni, X. Wang, S. Amoruso, and R. Bruzzese, Laser Phys. 24, 105902 (2014).
[52] N. Tsakiris, K. K. Anoop, G. Ausanio, M. Gill-Comeau, R. Bruzzese, S. Amoruso, and L. J. Lewis, J. Appl. Phys. 115, 243301 (2014).
[53] C. Phipps (Ed.), *Laser Ablation and its Applications*. Berlin, Germany: Springer-Verlag (2007).
[54] David A. Cremers and Leon J. Radziemski (Eds.), *Handbook of Laser-Induced Breakdown Spectroscopy*, John Wiley & Sons Ltd (2006).
[55] X. Wang, S. Amoruso, J. Xia, Appl. Surf. Sci. 255, 5211 (2009).
[56] K. F. Al-Shboul, S. S. Harilal, and A. Hassanein, J. Appl. Phys. 100, 221106 (2012).
[57] Langmuir, Irving et al., "*The theory of collectors in gaseous discharges*", Physical Review, (1926).
[58] "*Electrical Probes for Plasma Diagnostics*", J. D. Swift and M. J. R. Schwar., American Elsevier, New York (1969).
[59] "*Principles of Plasma Diagnostics*", Hutchinson, I.H., Second Edition. (Cambridge Press, 2002).
[60] "*Langmuir Probe in Theory and Practice*", Evgeny V. Shun'ko, Universal- Publishers (2009).
[61] William Whitty, Jean-Paul Mosnier., Appl. Surf. Sci. 127–129, 1035 (1998).
[62] K. S. Kaur, R. Fardel, T. C. May-Smith, M. Nagel, D. P. Banks, C. Grivas, T. Lippert, and R. W. Eason., J. Appl. Phys 105, 113119 (2009).
[63] G. Neumann and U. Banziger, M. Kammeyer., Rev. Sci. Instrum. M. Lange. 64, 19 (1993).
[64] R. E. Walkup, J. M. Jasinski, and R. W. Dreyfus. , Appl. Phys. Lett. 48, 1690 (1986).
[65] Y. B. S. R. Prasad, P. A. Naik, A. Kumar, and P. D. Gupta., Rev. Sci. Instrum. 77, 093106 (2006).
[66] K. Sasaki, S. Matsui, H. Ito, and K. Kadota., J. Appl. Phys., 92, 11 (2002).

[67] Prasoon K. Diwakar, Jhanis J. Gonzalez, Sivanandan S. Harilal, Richard E. Russo and Ahmed Hassanein, J. Anal. At. Spectrom. 29, 339 (2014).
[68] D. B. Geohegan and A. A. Puretzky, Appl. Sur. Sci. 96-98, 126 (1996).
[69] R. A. AI-Wazzan, J. M. Hendron and T. Morrow, Appl. Sur. Sci. 96-98,170 (1996).
[70] V. V. Bukin ; S. V. Garnov ; A. A. Malyutin ; D. K. Sytchev and N. S. Vorobiev, Proc. SPIE 6606, Advanced Laser Technologies 2006, 660610 (2007).
[71] Ronnie Shepherd, Rex Booth, Dwight Price, Mark Bowers, Don Swan, Jim Bonlie, Bruce Young, Jim Dunn, Bill White, and Richard Stewart, Rev. Sci. Instrum. 66 (1), 719 (2005).
[72] Goda, K., Tsia, K. K. & Jalali, B. Serial time-encoded amplified imaging for real-time observation of fast dynamic phenomena. Nature 458, 1145 (2009).
[73] K. Nakagawa, A. Iwasaki, Y. Oishi, R. Horisaki, A. Tsukamoto, A. Nakamura, K. Hirosawa, H. Liao, T. Ushida, K. Goda, F. Kannari and I. Sakuma, Nature Photonics 8, 695 (2014).
[74] *Pulsed Laser Deposition of Thin Films, Application-Led Growth of Functional Materials*, R. Eason (Ed.), Wiley (2006).
[75] K. K. Anoop, A. Rubano, R. Fittipaldi, X. Wang, D. Paparo, A. Vecchione, L. Marrucci, R. Bruzzese, and S. Amoruso, Appl. Phys. Lett. 104, 241604 (2014).
[76] A.Y. Vorobyev and C. Guo, Laser Photonics Rev., 1–23 (2012). [and the references therein].
[77] A.Y. Vorobyev and C. Guo, Phys. Rev. B 72, 195422 (2005).
[78] T.Y. Hwang, A.Y. Vorobyev, and C. Guo, Appl. Phys. Lett. 95, 123111 (2009).
[79] A. Borowiec and H. K. Haugen, Appl. Phys. Lett. 82, 4462 (2003).
[80] F. Costache, S. Kouteva-Arguirova, and J. Reif, Appl. Phys. A 79, 1429 (2004).
[81] J. Bonse, M. Munz, and H. Sturm, J. Appl. Phys. 97, 013538 (2005).
[82] R. Le Harzic, H. Schuck, D. Sauer, T. Anhut, I. Riemann, and K. Konig, Opt. Express 13, 6651 (2005).
[83] J. Wang and C. Guo, Appl. Phys. Lett. 87, 251914 (2005).
[84] Y. Huang, S. Liu, W. Li, Y. Liu, and W. Yang, Opt. Express 17, 20756 (2009).
[85] C. Wu, C.H. Crouch, L. Zhao, J. E. Carey, R. Younkin, J. A. Levinson, E. Mazur, R.M. Farrell, P. Gothoskar, and A. Karger, Appl. Phys. Lett. 78, 1850 (2001).
[86] A.Y. Vorobyev and C. Guo, Opt. Express 19, A1031 (2011).
[87] A.Y. Vorobyev and C. Guo, Appl. Phys. Lett. 92, 041914 (2008).
[88] A.Y. Vorobyev and C. Guo, J. Appl. Phys. 104, 053516 (2008).
[89] T. Baldacchini, J. E. Carey, M. Zhou, and E. Mazur, Langmuir 22, 4917 (2006).
[90] E. L. Papadopoulou, M. Barberoglou, V. Zorba, A. Manousaki, A. Pagkozidis, E. Stratakis, and C. Fotakis, J. Phys. Chem. C 113, 2891 (2009).
[91] A.Y. Vorobyev and C. Guo, Opt. Express 18, 6455 (2010).
[92] A.Y. Vorobyev and C. Guo, Appl. Phys. Lett. 99, 193703 (2011).
[93] R.V. Volkov, D.M. Golishnikov, V.M. Gordienko, and A. B. Savel'ev, JETP Lett. 77, 473 (2003).
[94] T.Y. Hwang, A.Y. Vorobyev, and C. Guo, Phys. Rev. B 79, 085425 (2009).
[95] A.Y. Vorobyev, V. S. Makin, and C. Guo, Phys. Rev. Lett. 102, 234301 (2009).

[96] I. N. Zavestovskaya, A. P. Kanavin, and N. A. Men'kova, J. Opt. Technol. 75, 353–358 (2008).
[97] M. Birnbaum, J. Appl. Phys. 36, 3688 (1965).
[98] D. C. Emmony, R. P. Howson, and L. J. Willis, Appl. Phys. Lett. 23, 598 (1973).
[99] J. E. Sipe, J. F. Young, J. F. Preston, and H. M. van Driel, Phys. Rev. B 27, 1141 (1983).
[100] M. Bonch-Bruevich, M. N. Libenson, V. S. Makin, and V.V. Trubaev, Opt. Eng. (Bellingham) 31, 718 (1992).
[101] A.V. Zayats and I. I. Smolyaninov, J. Opt. A, Pure Appl. Opt. 5, S16 (2003).
[102] A.Y. Vorobyev, V. S. Makin, and C. Guo, J. Appl. Phys. 101, 034903 (2007).
[103] H. Raether, Surface Plasmons on Smooth and Rough Surfaces and on Gratings (Springer-Verlag, Berlin, 1988).
[104] V. S. Makin, R. S. Makin, A.Y. Vorobyev, and C. Guo, Tech. Phys. Lett. 34, 387 (2008).
[105] J. Reif, O. Varlamova, S. Varlamov, and M. Bestehorn, Appl Phys A 104, 969 (2011).
[106] O. Varlamova, J. Reif, S. Varlamov, and M. Bestehorn, J. Nanosci. Nanotechnol. 11, 9274 (2011).
[107] J. Reif, in: Laser-Surface Interactions for New Materials Production, Springer Series in Materials Science, Vol. 130, , pp. 19–41, edited by A. Miotello and P. Ossi (Springer, Berlin, Heidelberg, 2010).
[108] D. Dufft, A. Rosenfeld, S. K. Das, R. Grunwald, and J. Bonse, J. Appl. Phys. 105, 034908 (2009).
[109] E. M. Hsu, T. H. R. Crawford, C. Maunders, G. A. Botton, and H. K. Haugen, Appl. Phys. Lett. 92, 221112 (2008).
[110] K. Dou, E. T. Knobbe, R. L. Parkhill, B. Irwin, L. Matthews, and K. H. Church, Appl. Phys. A 76, 303 (2003).
[111] X. Li, C. Yuan, H. Yang, J. Li, W. Huang, D. Tang, and Q. Xu, Appl. Surf. Sci. 256, 4344 (2010).
[112] A.Y. Vorobyev and C. Guo, Appl. Surf. Sci. 253, 7272 (2007).
[113] T. H. Her, R. J. Finlay, C. Wu, S. Deliwala, and E. Mazur, Appl. Phys. Lett. 73, 1673–1675 (1998).
[114] V. Oliveira, S. Ausset, and R. Vilar, Appl. Surf. Sci. 255, 7556 (2009).
[115] K. Nayak and M. C. Gupta, Opt. Lasers Eng. 48, 940 (2010).
[116] Junichi Hamazaki, Ryuji Morita, Keisuke Chujo, Yusuke Kobayashi, Satoshi Tanda, and Takashige Omatsu, Opt. Express 18, 2144 (2010).
[117] Cyril Hnatovsky, Vladlen G. Shvedov, Wieslaw Krolikowski, and Andrei V. Rode, Optics Letters 35, 3417(2010).
[118] Hnatovsky, V. G. Shvedov, N. Shostka, A. V. Rode, and W. Krolikowski, Opt. Lett. 37, 226 (2012).
[119] B. Wetzel, C. Xie, P.-A. Lacourt, J. M. Dudley, and F. Courvoisier, Appl. Phys. Lett. 103, 241111 (2013).

[120] K. Lou, S.-X. Qian, X.-L. Wang, Y. Li, B. Gu, C. Tu, and H.-T. Wang, Opt. Express 20, 120 (2012).
[121] Y. Jin, O. J. Allegre, W. Perrie, K. Abrams, J. Ouyang, E. Fearon, S. P. Edwardson, and G. Dearden, Opt. Express 21, 25333 (2013).
[122] Laser Precision Microfabrication, edited by K. Sugioka, M. Meunier, and A. Piqué (Springer, Heidelberg, 2010).
[123] K. Sugioka and Y. Cheng, Light: Sci. Appl. 3, e149 (2014).
[124] L. Marrucci, C. Manzo, and D. Paparo, Phys. Rev. Lett. 96, 163905 (2006).

Chapter 3
Experimental Methods

3.1 Introduction

This chapter covers a brief explanation of experimental methods used for ultrafast laser ablation (ULA) and its subsequent analysis. In order to explore the basic physical mechanism underlying ULA and its possible applications, we have utilized three experimental configurations. Aim of each configuration and setup requirements are illustrated in the following sections.

- Characterization of the laser produced plasma plume, which comprises direct and spectrally-resolved fast gated ICCD imaging of different species emission in the plume, and plasma plume ion dynamics using Langmuir probe and Faraday cup.
- Nanoparticle generation in ULA.
- Optical vortex laser ablation and surface micro/nanostructuring.

Section 3.2 includes the experimental setup and a brief explanation of the major components used for the characterization of ULA of solid targets, in high vacuum condition. This setup is used for spatio-temporal analysis of excited ions and neutrals in the ULA plume at moderate to high intensity (10^{13} to 10^{15} W/cm^2) with different diagnostic techniques. The major components used for this multidiagnostic analysis are ultrashort laser sources (3.2.1), optical detectors (3.2.2), spectrally-resolved ICCD imaging (3.2.3), and charge collection detectors, as Langmuir probe and Faraday cup (3.2.4).

Section 3.3 details the experimental setup used for nanoparticle generation. A brief explanation of nanoparticles imaging with intensified charge coupled device (ICCD), and size characterization using atomic force microscopy (AFM) are presented in this section.

Finally, section 3.4 details the setup used for optical vortex laser ablation. This process is mainly applied to material surface modification or patterning at micro-nano scale, in air. A high-resolution field emission scanning electron microscope (FESEM) is used for characterization of the laser-processed surfaces. A brief explanation of the operating principles of a *q*-plate, which is capable of imparting orbital angular momentum (OAM) to a light beam by exploiting a variation of spin angular momentum (SAM), and other optical and optomechanical components used are given in subsections 3.4.1 and 3.4.2.

3.2 Characterization of Ultrashort Laser Ablation Plasmas

A schematic of the experimental setup used for ULA of solid targets in vacuum is shown in Fig. 3.1. This setup allows simultaneous measurements of ultrafast laser produced plasma (LPP) plume features and expansion dynamics by means of Langmuir probe (LP), Faraday cup (FC) and spectrally resolved ICCD imaging. The LP and FC are used to study ion dynamics, while ICCD cameras are used for direct and spectrally-resolved imaging of the different species emission in LPP. Further details of the experimental setup used for characterization of ULA plasmas are given in chapter 4. This section covers the main components used for LPP characterization.

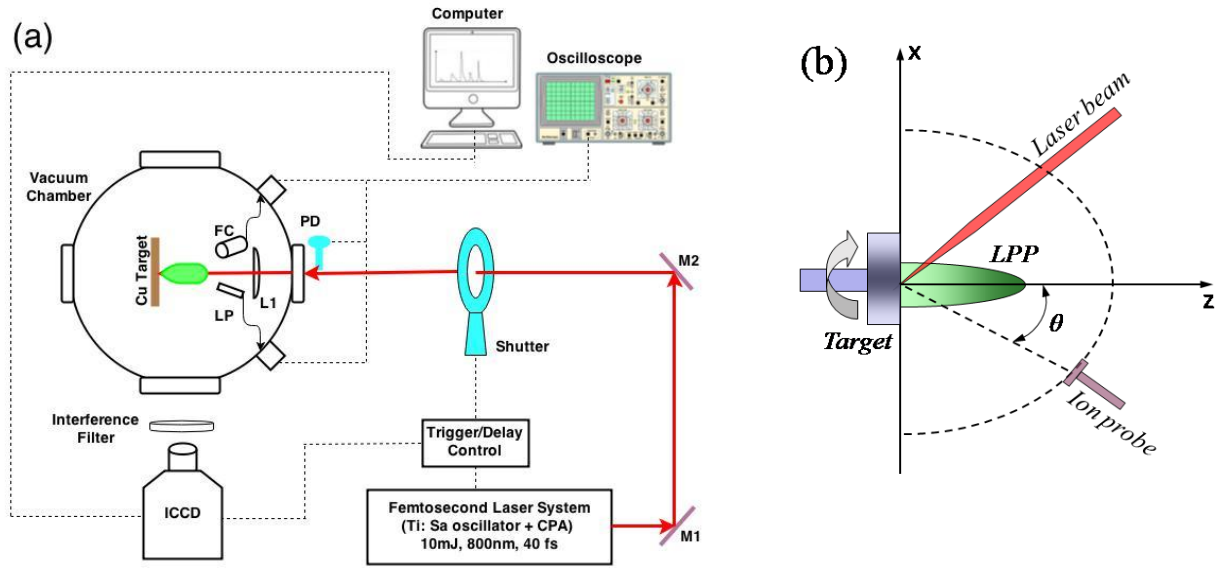

Figure 3.1: (a) Schematic of the experimental setup used for ultrafast laser ablation of solid targets. Dotted lines show the triggering and data acquisition channels. ICCD: Intensified Charge Coupled Device; LP: Langmuir Probe; FC: Faraday Cup; PD: Photo Diode; L1: Lens; M1 and M2: Mirrors. (b) Sketch of the setup used for the ion angular distribution measurements.

All the above set of experiments were performed in high vacuum, which was obtained by operating a turbo molecular pump backed by a rotary pump. The laser entry window of the vacuum chamber was made of quartz with good transmission from UV to IR.

3.2.1 Ultrashort Laser Sources

We have used three solid state laser systems to perform the ultrafast laser ablation experiments [1-3]. The details of each laser system are given in Table 3.1. All the laser sources are based on chirped-pulse amplification (CPA) [4, 5], which enables the generation of high peak power laser pulses with temporal duration in the sub-picosecond range. A single shot autocorrelator [6] is used

to measure the pulse duration. Details of CPA and pulse duration measurement through single shot autocorrelation technique are summarized in Appendix A.

Laser System	**Specifications**	**Model/Company**
Ti:Sapphire I	Repetition rate: 1 kHz Centre wavelength: 800 nm Pulse duration: 50 fs Output Energy: 4 mJ	"Legend Elite" Coherent Inc.
Nd:Glass	Fundamental Beam Repetition rate: 33 Hz Centre wavelength: 1054 nm Pulse duration: 1 ps Output Energy: 4 mJ Second Harmonic Beam Repetition rate: 33 Hz Centre wavelength: 527 nm Pulse duration: 250 fs Output Energy: 1 mJ	"Twinkle" Light Conversion Ltd.
Ti:Sapphire II	Repetition rate: 10 Hz Centre wavelength: 800 nm Pulse duration: 40 fs Output Energy: 12 mJ	"Pulsar" Amplitude Systems.

Table 3.1: Details of laser systems used for ultrafast laser ablation of solid targets.

3.2.2 Light Detectors: Intensified CCD (ICCD) Cameras

Light detectors are essential part of any optical experiments. The LPP is a micro source of light that can be analyzed by an intensified charge-coupled device (ICCD). We have used ICCD cameras in two different modes to record low photon emission process that occurs within a short interval of time (typically nanoseconds to microseconds) during ULA. In the first mode, both direct and spectrally-resolved imaging of LPP was carried out, while in the other mode, time resolved emission spectra of LPP were registered by coupling the ICCD to a Czerny-Turner spectrograph (Acton SP2500i). Two fast gated ICCDs with different specifications (istar Andor Technology Ltd. and PI-MAX Princeton Instruments) were used [7, 8].

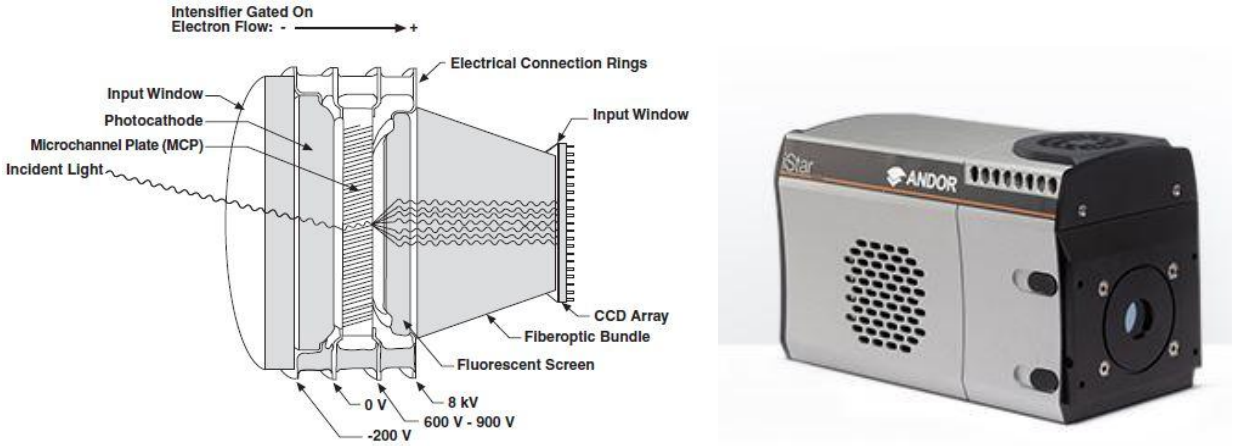

Figure 3.2: Major components of the Intensifier-CCD (on left) and front view of Andor ICCD head (on right)

Fast gating and high gain in optical domain are the two important features of ICCD cameras. As its name implies, an ICCD camera consists of an intensifier tube and a charge coupled device (CCD). The gating and the amplification occurs in the image intensifier tube, which is an evacuated tube comprising a photocathode, a microchannel plate (MCP), and a phosphor screen. The properties of these components determine the overall performance of the device. These components are mounted one close behind other in the mentioned sequence as shown in Fig. 3.2. The photocathode, coated on the inner surface of the input window, captures the incident photons producing photoelectrons, which are then drawn towards the MCP by an electric field. The MCP is a thin disc (about 1mm thick) which is a honeycomb of glass channels of typically 6-10 μm, each with a resistive coating. A high potential is applied across the MCP (600-900 V), enabling the photoelectron to accelerate down one of the channels in the disc. When the photoelectron has sufficient energy, it produces secondary electrons from the channel walls, thus resulting in the electron signal gain. The gain is adjusted by increasing or decreasing the voltage at the MCP output. Gains in excess of 10^4 can be readily achieved. At the exit of the MCP channels, electrons are further accelerated by a constant high voltage (5-8 kV), and eventually strike the phosphor coating on the fluorescent screen causing it to release photons. Because of the MCP gain, there are now many photons for each photon that struck on the photocathode surface.

The output of the intensifier tube is coupled to the CCD, typically by a fiber optics coupler that is physically compact and with low optical distortion level. The charge accumulates in the CCD pixel wells until the intensifier is gated off. At that point, the accumulated charge is shifted to the

serial register where it is read out to an on-chip amplifier that converts the charge to an analog voltage. This voltage is input to the selected analog-to-digital converter (A/D) where it is digitally encoded. The digitalized information is transmitted from camera head to interface card in the host computer, where it is stored in the RAM, and the application software retrieves the information from the RAM, processes it, and displays on the screen according to user defined settings.

An image intensifier inherently includes a 'gating' functionality. If the control voltage between photocathode and the MCP is reversed, the emitted photoelectrons are not accelerated towards the MCP, but return to the photocathode. Thus, no electrons are going to phosphor screen and no light falls onto the CCD. This process of blocking or allowing light for a short duration of time by reversing the control voltage is called 'gating'. The 'gate delay' and 'gate width' are two commonly used parameters in ICCD operation. The former represents the delay time between the zero time of the experiment (time at which laser pulse hits the target, in our case), and the starting time of ICCD operation, while the latter represents the temporal width of the 'on' state of the ICCD. To achieve fast gating a high voltage pulser must be used, which can produce 200 V pulses with sub-picosecond rise and fall times. To improve signal to noise ratio, we usually operate ICCD in a 2x2 binning mode. In order to get accuracy of plasma plume evolution, images were recorded by adjusting the gate delay and gate width with respect to zero time in the experiment.

3.2.3 Spectrally Resolved ICCD Imaging Technique

Spectrally resolved ICCD imaging is a powerful method to investigate the spatial and temporal evolution of different plasma plume components (ions, atoms, and nanoparticles) produced during ULA of solid targets. For example, in our experimental condition, the temporal evolution of neutral (Cu^{*}) and ionic (Cu^{+}) components of Cu LPP are separately imaged by exploiting bandpass interference filters in front of an ICCD camera, whereas for the NPs plume, its broadband emission is imaged. The spectrally resolved analyses of copper fs LPP plasma emission showed intense, characteristic emission lines of Cu neutrals and ions in the visible spectral range [9, 10]. In particular, the most intense emissions are:

i) Cu-excited neutrals at 510.55 nm ($3d^{10}4p\ ^{2}P_{3/2} \rightarrow 3d^{9}4s^{2}\ ^{2}D_{5/2}$), 515.32 nm ($3d^{10}\ 4d\ ^{2}D_{3/2} \rightarrow 3d^{10}4p\ ^{2}P_{1/2}$), and 521.82 nm ($3d^{10}4d\ 2D_{5/2} \rightarrow 3d^{10}4p\ 2P_{3/2}$) [11];

ii) Cu-excited ions in the range ≈490-495 nm, resulting from the overlap of three different Cu^+ strong lines in the visible range, i.e. 490.97 nm, 493.17 nm ($3d^9(2D_{5/2})4f \rightarrow 3d^9 4d$) and 495.37 nm [11-13].

Prior to the spectrally resolved imaging analyses, we confirmed that the above spectral features are valid also in our experimental conditions by optical emission spectroscopy. Then, we used corresponding bandpass interference filters with center wavelength λ_c = 514.5 nm and λ_c = 490 nm (FWHM of 10 nm and out-of-band rejection of OD 4) to register spectrally resolved images of Cu neutrals and ions, respectively. The majority of transitions in the specified filters band are copper neutrals (λ_c = 514.5 nm), and ions (λ_c = 490 nm) emission lines, so we consider that the obtained images are representative of neutrals and ions, respectively. Our spectrally resolved Cu emission spectra also confirm that the contribution of continuum emission is negligible at the investigated delays after the laser pulse. We used the advantages of this method to characterize fundamental features of the interaction of ultrashort laser pulses with solid targets, and of the subsequent expansion of the produced plasma plume. The details of measurements and experimental outcomes are thoroughly discussed in chapter 4.

3.2.4 Charge Detectors: Langmuir probe and Faraday Cup

During femtosecond (fs) laser ablation, ionization of the target occurs at the beginning of the laser pulse and thereby many electrons and ions are generated. These charged particles play an important role in the characterization of LPP. Langmuir probes and Faraday cups have been widely used to diagnose the low temperature plasmas produced by pulsed laser ablation of solid targets. These diagnostic techniques can be used to measure the plasma density and temperature, the plasma flow velocity and the shape of the ablation plume expansion [14]. In our experimental study, we mainly focused on the ion dynamics in the LPP and plume expansion properties.

A planar Langmuir probe facing the plume was used for the investigation. The ion probe area was 5.0×2.5 mm^2. The Langmuir probe was kept at a distance from the target surface of 3 cm to 14 cm, depending to the experimental conditions. The circuit diagram employed to bias the probe and register the collected ion current is schematically shown in Fig. 3.3(a). The bias voltage (Vcc) was maintained using a 1-μF capacitor, and the collected ion current was determined by recording the voltage signal across a 50 Ω load resistor with a digital oscilloscope. Prior to the experiments, the area of the collected ion signal was measured as a function of the bias voltage to determine the ion

saturation region [15], as shown in Fig. 3.3(b). A negative bias voltage on the probe allowed the collection of positive ions. When the voltage was sufficiently high to prevent electrons with the highest thermal energies in the plasma from reaching the probe, the collected charge became saturated at a Vcc lower than approximately –15 V. The ion probe was biased at a constant working voltage within the saturation region, i.e., at Vcc = −20 V, during measurements. The ion velocity can be determined from the ion time of flight (TOF) from the target to the probe and hence the ion density can be found from the magnitude of the ion signal.

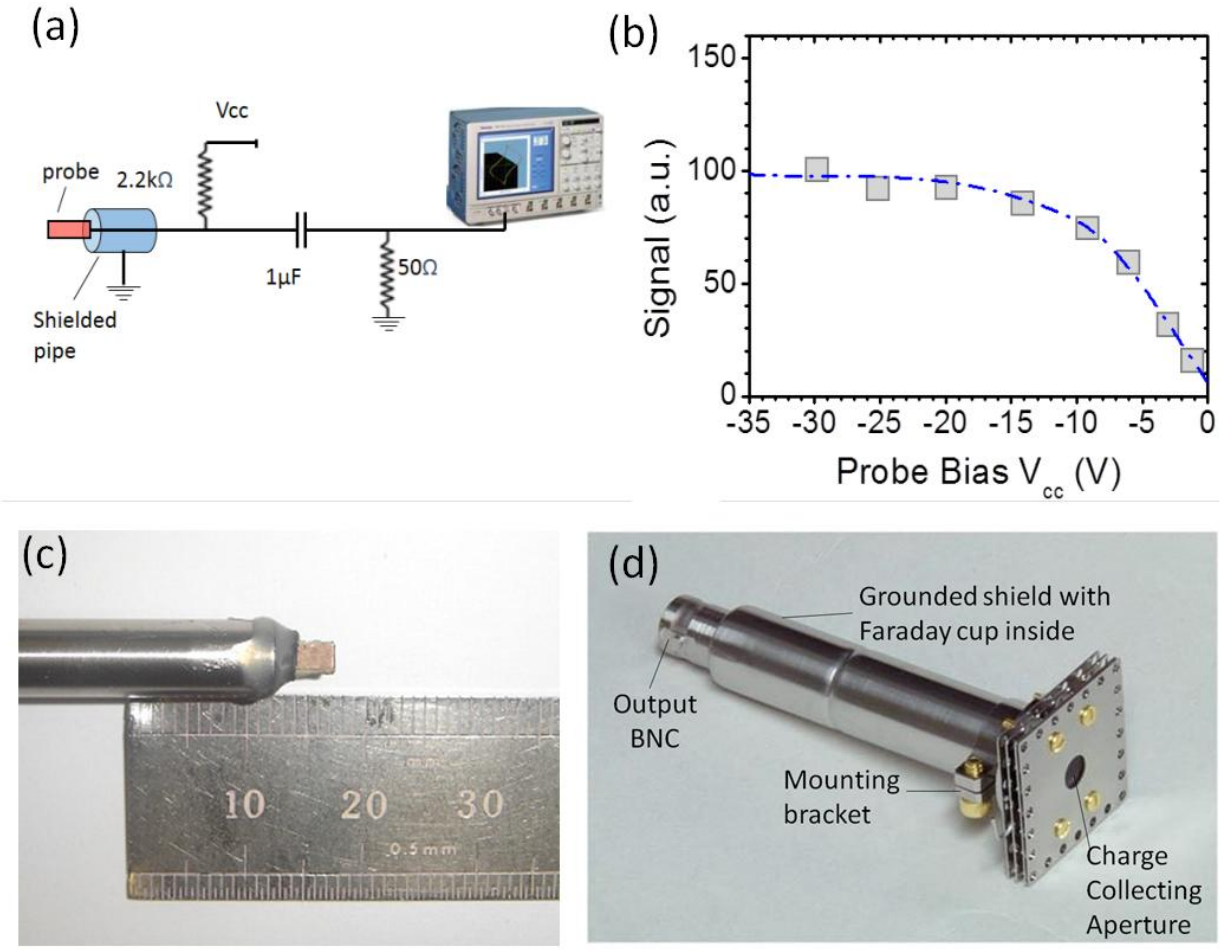

Figure 3.3: (a) Schematic diagram of the ion probe circuit. (b) Integrated intensity of the ion flux collected on probe area versus bias-voltage Vcc showing the occurrence of the ion saturation region for Vcc lower than about -15 V. (c) and (d) are photographs of typical Langmuir probe and Faraday cup.

A Faraday cup is a conductive metal cup designed to collect charged particles in vacuum. The Faraday cup (Kimball Physics Inc. model FC-71A) consists of a hollow stainless steel cylinder

closed at the base, with a 2.54 mm diameter aperture for collecting the electrons or ions [16]. An outer, grounded cylinder provides shielding. An electrical connection is made to the base of the Faraday cup, terminating in a BNC. The current is, then, conducted to a vacuum feedthrough and so to an oscilloscope. The Faraday cup can be electrically biased to reduce scattering of electrons or ions collected in the cup and to reduce secondary electron emission. For electrons or negative ions, +50 V is typically adequate, and for positive ions, –50 V. This can be accomplished by placing a battery between the vacuum feedthrough and the oscilloscope.

3.3 Nanoparticle generation in ultrashort laser ablation

The direct ejection of nanoparticles (NPs) is one of the most striking and intriguing features of ultrashort laser ablation [17, 18]. This phenomenon is related to the capability of inducing non-equilibrium, extreme states in the irradiated material whose relaxation dynamics allows the generation of specific thermodynamic conditions during the decomposition stage, which eventually result in NP formation [19, 20]. Typically, NPs constitute the major part of the material blow-off produced in ULA of a metallic target, the atomic plume accounting for only 10%–20% of the total ablated mass [21]. Therefore, ULA of metals in vacuum is among the most promising prospective techniques for the preparation of NPs and NPs-assembled media.

A schematic of NPs imaging and deposition setup is shown in Fig. 3.4(a). The NPs produced during the ULA process were collected on mica substrates located at a distance of 45 mm in front of the target surface, in high vacuum. The deposition time was selected in such a way that monodispersed, less than one layer deposits of NPs were obtained, thus limiting the influence of particles coalescing on the substrate and obtaining a reliable determination of the NPs size. Moreover, the laser beam on the target was rastered over an annulus with a thickness of about 1 mm in order to avoid possible consequences due to the formation of a deep crater on the target surface on NPs formation after many shots. Copper NPs were deposited at different laser fluences, in the range ≈1-10 J/cm^2, to elucidate the role of the laser fluence on the NPs size. At the same time, NPs population is imaged using a fast gated ICCD at longer delay (10-100 μs) after irradiation. This 2D images provide further information of NPs emission at different laser fluences and delay times.

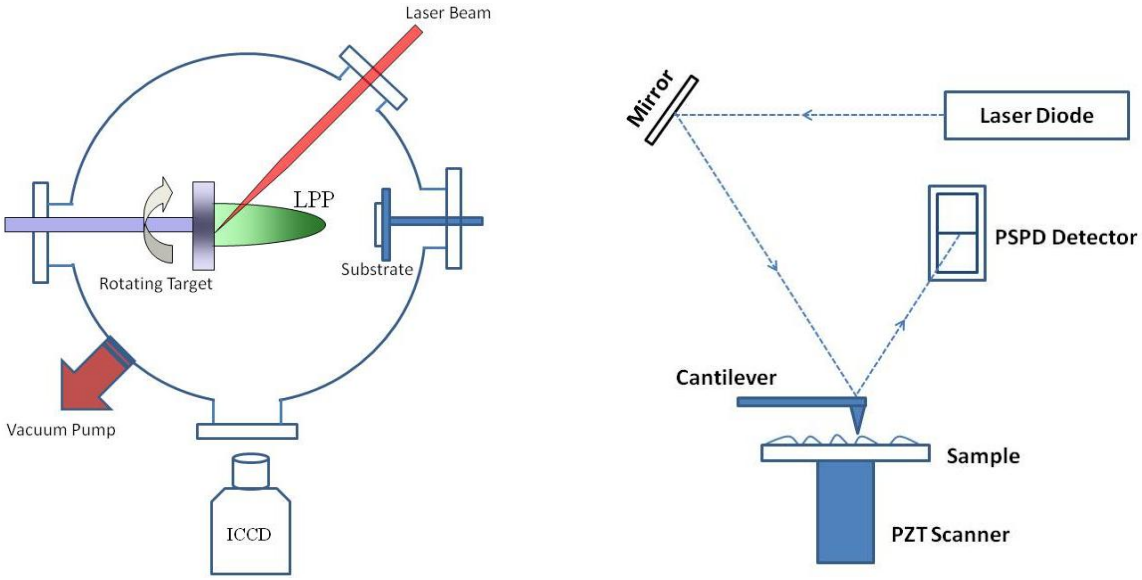

Figure 3.4: (a) Typical setup of nanoparticle imaging and deposition, in high vacuum. (b) Typical optical detection scheme in AFM.

The size characteristics of the NPs were measured by AFM (Digital Instruments Nanoscope IIIa) analysis of the deposits [22]. The AFM images were collected in tapping mode by using a sharpened silicon tip with a radius of less than 5 nm [see Fig. 3.4(b)]. The subsequent data analysis was carried out by exploiting image analysis software. After performing deconvolution on each AFM image, in order to avoid the tip size effect, the particles average size in a plane parallel and orthogonal to the substrate was evaluated. In this way, the three-dimensional view of the deposits was reconstructed and the NPs equivalent spherical diameter (ESD) was estimated. Finally, NPs deposits with different pulse duration in the range ≈50-600 fs, at a fixed fluence, were carried out to explore the possible effect of the ultrashort laser pulse length on the NPs size characteristics. The obtained results of NPs imaging and size characterization are given in chapter 5. Appendix B describes how AFM technology performs size characterization of deposited NPs.

3.4 Optical-Vortex Laser Ablation

The spatial profile of an Optical Vortex (OV) beam is a ring of light with a zero electric field at center. Since OVs possess orbital angular momentum, material ablation using OVs has gained considerable importance in both understanding of underlying physical mechanisms and material processing applications. We studied the laser surface structuring of silicon and copper targets using Ti:Sapphire fs laser ablation with OV beams. A schematic of the experimental setup of fs vortex

beam laser structuring is shown in Fig. 3.5. A *q*-plate is used to generate an OV beam with fs pulse duration through spin-to-orbital conversion of the angular momentum of light [23]. The variation of the produced surface structures is studied as a function of the number of pulses, *N*, and laser polarization, ***P***, and our experimental results are given in chapter 6.

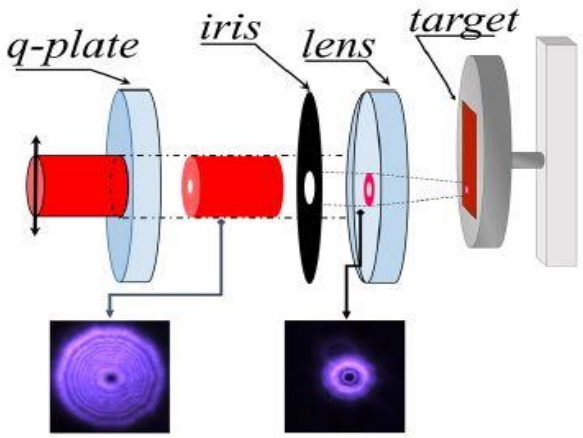

Figure 3.5: Schematic of the experimental setup of fs vortex beam laser structuring.

We have used two types of microscopy techniques to analyze the laser-processed silicon and copper surfaces. They are optical microscopy and scanning electron microscopy (SEM). An optical microscope (Axio Scope A1, ZEISS) gives a clear idea of total magnitude of the processed surface structure and a rough idea of the patterns formed on the surface. The SEM is a versatile, non-destructive technique that reveals detailed information about the morphology and the composition of natural and manufactured materials. The processed silicon and copper targets in our experiments were inspected using a field emission scanning electron microscope (FESEM, Model: ΣIGMA, ZEISS) which delivers advanced analytical microscopy with a nominal resolution of 1.3 nm at 20 kV [24]. A brief explanation about FESEM used in our experiment is reported in Appendix C.

3.4.1 Optical and Optomechanical Devices

A wide range of optical and optomechanical devices are used in our experiments to perform controlled laser ablation with desired laser beam parameters. We know that the pulsed beam coming out of the ultrafast lasers is linearly polarized in specific direction perpendicular to propagation direction and with high peak power. Depending on the laser ablation condition, especially target material, we have to control the pulse energy or peak power falling on the surface. A combination

of a half waveplate and a polarizer in the optical path allows changing energy and polarization of the laser beam.

In the case of orbital angular momentum (OAM) beam laser ablation or vortex laser ablation, we used a quarter waveplate for imparting circular polarization i.e. spin angular momentum (SAM) to the incoming linearly polarized light. A polarizing cube beam splitter can be used to separate the s and p polarization components of the laser beam. A twist in the spherical wavefront can be obtained by introducing a *q*-plate in the optical path. The *q*-plate is a new optical device introduced in 2006 [23], which is capable of imparting OAM to a light beam by exploiting a variation of SAM. More details of q-plate and its working principle are given in section 3.4.2. This combination of polarizing cube beam splitter, quarter waveplate, and a *q*-plate allow the generation of light having OAM starting with an ordinary laser beam. A set of suitable neutral density (ND) filters is used to reduce the energy of OAM beam. The laser beam characterization was performed by taking optical wedge reflection of the beam to the laser beam profiler.

In addition, we used optomechanical components like an optical beam shutter (Uniblitz), iris/aperture (ID12/M, Thorlabs Inc), and a high-precision long travel linear piezo XY stage (PPS-20, Miconix USA) to perform controlled ultrafast laser ablation [25, 26].

3.4.2 The *q*-plate

The angular momentum of light associated with rotation of electric and magnetic fields oscillating within the optical wave is named as spin angular momentum (SAM), while that associated with a spiral wavefront is called orbital angular momentum (OAM). The OAM of light has been an attractive research field because of its possible technological applications in the areas of particle manipulation, optical sensing, and classical and quantum optical communication [27]. The *q*-plate is an optical device to couple spin and twist, i.e., it is capable of imparting OAM to a light beam by exploiting a variation of SAM. This device allows the generation of light having OAM starting with an ordinary light (zero OAM) having circular polarization.

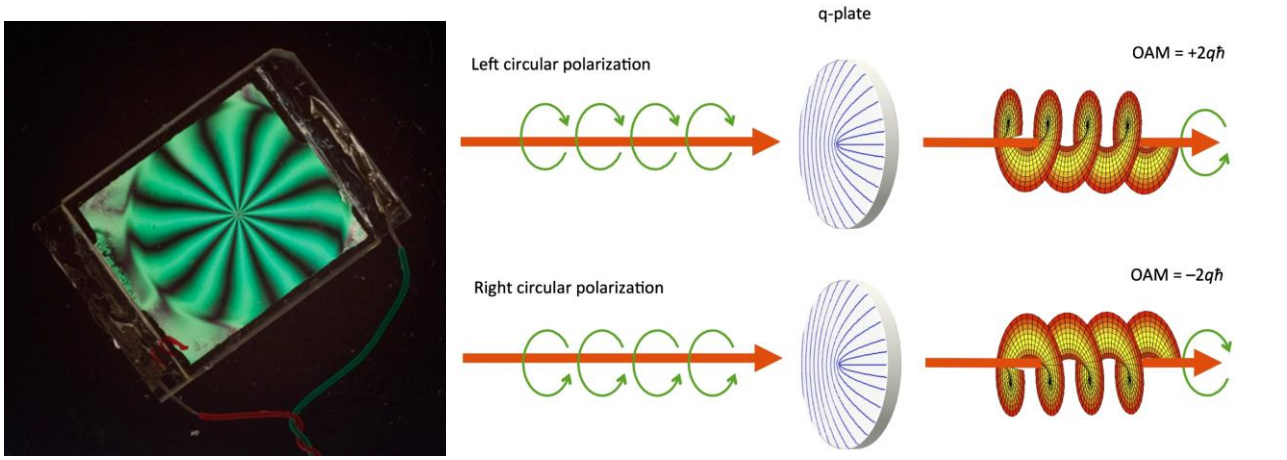

Figure 3.6: A q-plate device with topological charge q = 3 and electric tuning (left image), right image is the schematics of the optical effect of a q-plate. Left (right) circularly polarized light having zero OAM at the input is converted into light carrying an OAM per photon given by +2qℏ (–2qℏ). The circular polarization handedness gets also inverted in the process [courtesy Ref. 28].

The *q*-plate is basically a liquid crystal cell, essentially a thin liquid crystal film sandwiched between two glasses, with a peculiar singular pattern of molecular alignment, obtained by a suitable previous treatment of the containing glass surfaces [see Fig. 3.6(a)]. The pattern is mainly defined by a characteristic number, named topological charge and characterizing the central singularity, that is usually denoted by the symbol *q*, from which the device got its name. In addition, as the optical effect of a liquid crystal can be controlled electrically, the *q*-plates can be tuned for having a partial effect, if desired, or even switched on and off.

References

[1] "Legend Elite" Mode-Locked Ti:Sapphire Laser, User's Manual, Coherent Inc.
[2] "Twinkle" Mode-Locked Nd:Glass Laser, User's Manual, Light Conversion Ltd.
[3] "Pulsar" Mode-Locked Ti:Sapphire Laser, User's Manual, Amplitude Systems.
[4] D. Strickland, G. Mourou, "Compression of amplified chirped optical pulses", Opt. Commun. 56, 219 (1985)
[5] Moulton P.F., Spectroscopic and laser characteristics of Ti:Al_2O_3, J. Opt. Soc. Am. B 3, 125 (1986).
[6] "Single-Shot Autocorrelator (SSA)", User's Manual, Coherent Inc.
[7] " istar " ICCD camera, User's Guide, Andor Technology Ltd.
[8] " PI-MAX" ICCD camera, User's Guide, Princeton Instruments.
[9] X. Wang, S. Amoruso, J. Xia, Appl. Surf. Sci. 255, 5211 (2009).
[10] S. Noel, J. Hermann, T. Itina, Appl. Surf. Sci. 253, 6310 (2007).

[11] A. Kramida, Yu. Ralchenko, J. Reader, and NIST ASD Team (2014), NIST Atomic Spectra Database (ver. 5.2), [Online]. Available at: http://physics.nist.gov/asd.
[12] N. Konjević and W.L. Wiese, J. Phys. Chem. Ref. Data 19, 1307 (1990).
[13] Reader, J. and C.H. Corliss, "Line spectra of the elements," in CRC Handbook of Chemistry and Physics, edited by D. R. Lide (CRC Press, Boca Raton, FL, 2005).
[14] D.W. Koopman, Physics of Fluids, 14, 1707 (1971).
[15] B. Doggett and J. G. Lunney, J. Appl. Phys. 105, 033306 (2009).
[16] " FC-71A" Faraday cup, User's Manual, Kimball Physics Inc.
[17] Amoruso, G. Ausanio, R. Bruzzese, M. Vitiello, and X. Wang, Phys. Rev. B 71, 033406 (2005).
[18] Eliezer, N. Eliaz, E. Grossman, D. Fisher, I. Gouzman, Z. Henis, S. Pecker, Y. Horovitz, M. Fraenkel, S. Maman, and Y. Lereah, Phys. Rev. B 69, 144119 (2004).
[19] D. Perez and L. J. Lewis, Phys. Rev. B 67, 184102 (2003).
[20] T. E. Glover, G. D. Ackerman, R. W. Lee, H. A. Padmore, and D. A. Young, Chem. Phys. 299, 171 (2004).
[21] S. Amoruso, R. Bruzzese, X. Wang, and J. Xia, Appl. Phys. Lett. 92, 041503 (2008).
[22] " Nanoscope IIIa " User's Manual, Digital Instruments Inc.
[23] L. Marrucci, C. Manzo, and D. Paparo, Phys. Rev. Lett. 96, 163905 (2006).
[24] "ΣIGMA" Field Emission Scanning Electron Microscope (FE-SEM), Carl Zeiss, Inc.
[25] Photonics products from Thorlabs Inc. (http://www.thorlabs.com/)
[26] Precision Piezo Stage (PPS-20), MICRONIX USA, LLC.
[27] J. P. Torres and L. Torner (Eds.), *Twisted Photons, Applications of Light with Orbital Angular Momentum* (Wiley, 2011).
[28] L. Marrucci, Journal of Nanophotonics 7, 078598 (2013).

Chapter 4

Characterization of Ultrashort Laser Ablation Plasmas

This chapter summarizes the different aspects of ultrashort laser ablation (ULA) of solid targets with special emphasis on copper. The spatial and temporal evolution of ultrafast laser produced plasma (LPP) plume components, in high vacuum conditions, is studied through a spectrally resolved imaging technique. The ionic (Cu^{+}) and neutrals (Cu^{*}) components are separately imaged by introducing corresponding bandpass interference filters in front of a fast gated intensified charge coupled device (ICCD). Since each image is representative of particular plume component, this analysis gives more insights to the fundamentals of ULA and its possible applications. The ionic components in the LPP plume are simultaneously studied using negatively biased Langmuir probe and Faraday cup. These allow studying the angular distribution and average kinetic energy of ions produced during ULA, and the obtained results are consistent with the spectrally resolved imaging technique. An interesting feature of our results is the generation of a fast ion population separated from the neutral component of the atomic plasma plume and characterized by sub-keV kinetic energies, which is interpreted in the frame of a simple model of ambipolar diffusion.

This chapter is divided mainly into two sections. First section (4.1) comprises the experimental results obtained from spectrally resolved ICCD imaging of ultrashort LPP, and ion dynamics in ULA using Langmuir probe in a moderate intensity regime (1×10^{13} to 2×10^{14} W/cm^2). The second section (4.2) illustrates the extension of the experimental characterization to a higher intensity regime (1.6×10^{13} to 2.2×10^{15} W/cm^2). An additional diagnostic technique, namely Faraday cup detector, has been introduced for ion dynamics in this last experiment. All the experiments in section 4.2 were performed at Center for Materials Under Extreme Environment (CMUXE), School of Nuclear Engineering, Purdue University, during my summer internship. The higher energy laser available at CMUXE allowed to extend our research on ULA to a higher intensity regime not achievable in our laboratory at the Physics Department, University of Naples Federico II. Since these two investigations were performed with two different laser systems and at different laboratories, the experimental parameters are slightly different. Therefore, some further details with respect to the general description of the experimental methods given in chapter 3 are reported separately in the two sections.

4.1 Ultrafast Laser Ablation at moderate intensity regime

A Ti:Sapphire laser system delivering fs pulses at 800 nm central wavelength was used for the ablation process at moderate intensity. An 8 mm pinhole selected the central part of the laser beam, and a half-wave plate and a polarizer system was used to vary the laser pulse energy delivered to the target. The duration of the laser pulse at the target was ≈50 fs, as measured by a single-shot, background-free autocorrelation technique. The laser beam was focused onto a pure copper (99.99+ %, GoodFellows) target at an angle of incidence of 45º with respect to the target normal. The target was positioned in the center of a vacuum chamber ($\leq 10^{-6}$ mbar), and was rotated to avoid local drilling. The laser spot area was $S = 1.4\times10^{-4}$ cm^2, as estimated by measuring the laser impact region as a function of the pulse energy, E, [1]. From the same set of measurements, the threshold fluence for copper ablation was obtained, resulting $F_{th} = (0.43 \pm 0.08)$ J/cm^2 in our experimental conditions. The average fluence F *(F = E/S)* used in the experiment was varied from the ablation threshold value F_{th} ($F_{th} \approx 0.4$ J/cm^2) up to ≈11 J/cm^2. The corresponding intensity range is $\approx 1\times10^{13}$ to $\approx 2\times10^{14}$ W/cm^2.

An ICCD was set near one window of the vacuum chamber, and perpendicular to the plume expansion direction to record the copper plasma plume evolution. The ionic and neutral components of the plume were separately imaged by keeping bandpass interference filters in front of the ICCD camera. In order to get the correct plume evolution, images were recorded with different gate widths and gate delays with respect to zero time, i.e., the time at which the laser pulse hits the target. The concept of spectrally resolved ICCD imaging is described in section 3.2.4. A schematic of the Langmuir probe setup used in the current investigation is shown in Fig. 3.1(b). Following Doggett et al. [2], a planar ion probe facing the plasma flow was used for this investigation. The ion probe is moved along a semicircular path in the zx plane. Angular measurements are made by varying the probe angle with respect to the target normal in the range of –90º – +90º to determine whether or not the laser beam incidence at 45º influences the hemispherical characteristics of the ion plume. The distance between the probe and the target surface was 32 mm. Additional details as circuit bias, operating voltage etc. of LP used in our experimental condition are given in section 3.2.4.

4.1.1 Spectrally resolved ICCD imaging of ultrashort laser produced plasma

Experiments were carried out by varying the fluence F from threshold to ≈11 J/cm^2. The results are summarized in Fig. 4.1, where examples of 2D images of the ULA plume are shown as a function of delay (Fig. 4.1(a)), and laser fluence (Fig. 4.1(c)).

We consider first the temporal behavior of the ULA plume. Figure 4.1(a) shows the copper plume evolution at F = 10.7 J/cm^2. In Fig. 4.1(a) the left column show images of the overall plume emission, while the central and right columns report images of the neutral and ion populations, respectively, at three different delays. In each image, the position (x = 0, z = 0) marks the laser spot on the target. The early stage of plume evolution mostly contains atomic components. Figure 4.1(b) shows the spatial profile of the emission intensity along the normal to the target surface at 150 ns after laser pulse, obtained from the images of Fig. 4.1(a). Dividing the distance z by the image capturing time (delay time 150 ns) provides information on the velocity of the various plume components. The obtained peak velocity of ionic and neutral components are ≈33 km/s and ≈9 km/s, respectively.

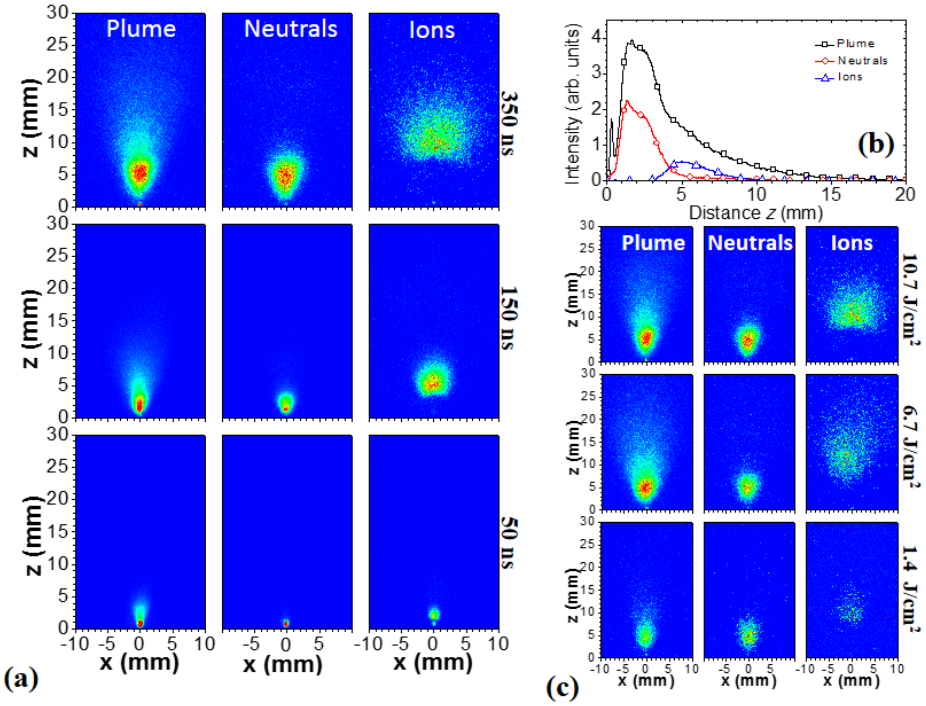

Figure 4.1: The 2D images of copper plasma plume evolution at different conditions. (a) Each column of images shows the different atomic plume populations at F=10.7 J/cm^2. The component names and the delays are marked on the top and right sides of the images. (b) Spatial profile of the emission intensity along the normal to target surface, z, for the three components of the copper plasma plume, at a delay of 150 ns. (c) 2D plume images of the atomic populations at different fluence F registered at a delay of 350 ns. Here the intensity of each image is normalized to its own maximum value.

The spectrally-resolved 2D images of Fig. 4.1(a) (second and third columns) provide further, interesting insights on the features of ULA atomic plumes. Interestingly, we observe that the atomic plume splits into two different populations of faster ions and slower neutrals, well separated in space already in the images registered at very early delay. Moreover, the ion population is spatially broader than the neutral one, while its emission intensity is much lower (see Fig. 4.1(b)). Analysis of these 2D spectrally-resolved images shows the dominance of the neutral component in the ULA plume emission, which can lead to some overlooking of the ionic population when imaging is done without spectral filtering. In the images, a clear edge between the two populations is also observed, which indicates a significant difference in the expansion behavior of neutrals and ions. The mechanism leading to the spatial separation of the two populations is already active in the very early stage of the ULA process, as testified by the distinct separation of the two components already at the very short delay investigated by the ICCD imaging. The early stage dynamics of ULA of an Al target induced by 100 fs Ti:Sapphire laser pulses was studied by Oguri et al. for laser intensities comparable to those of the present investigation [3]. These authors exploited time-resolved x-ray absorption fine structure imaging, showing the formation of a structured plume with ions slightly ahead of the neutrals already at a delay of 0.5 ns [3]. This suggests that an acceleration process leading to the faster ion velocity takes place at earlier time and distance. An ambipolar diffusion mechanism occurring in the very early stage of the plume expansion, which was considered earlier [4, 5], can explain the observed difference between ions and neutrals. This will be discussed in section 4.1.4.

Fig. 4.1(c) reports 2D images of the different plume populations, registered at a delay of 350 ns, for three values of the fluence. For easiness of comparison, in Fig. 4.1(c) the intensity of each image is normalized to its own maximum value. As the fluence raises, the plume shape becomes more defined as a consequence of the increase of the emission intensity. The clear spatial separation between the ionic and neutral components observed in Fig. 4.1(a) is present for each value of the laser pulse fluence, in the investigated range. This, in turn, suggests that this feature is characteristics of the ULA plume in this regime of interaction.

Fig. 4.2(a) reports the variation of the intensity of the atomic plume components as a function of fluence. The intensity was obtained by spatially integrating the 2D images at 350 ns for ions and neutrals (gate width = 50 ns). It was shown earlier that the fluence variation of the emission intensity is consistent with the fluence dependence of the overall ablation rate [6-8], therefore it can

give interesting insights on the ablation efficiency for the different plume components. Two different regimes are observed in the low and high fluence regions, with a crossover at about 3 J/cm^2 (≈6×F_{th}). This is in agreement with the theoretical predictions of both the two-temperature model, and molecular dynamics simulations [7, 9]. The existence of these two regimes is typical of ULA, and can be interpreted as a transition from a condition of energy absorption occurring in a region of the order of the material optical skin depth, to a situation of energy distribution regulated by the electron thermal diffusion length [9]. It is interesting to note that an increase in the laser fluence leads to a larger emission, as a consequence of the increase of the amount of ablated material for all three components, as already stated above [6-8]. The fluence increase also rises the plume temperature that further promotes the enhancement of emission intensity with the fluence. In particular, the ion emission shows a weaker dependence in the low-fluence regime, then followed by a steeper enhancement when the fluence approaches the transition stage, similarly to what observed earlier [10]. This, in turn, suggests that the plume ionization is less in the low-fluence regime and then increases in the high-fluence regime.

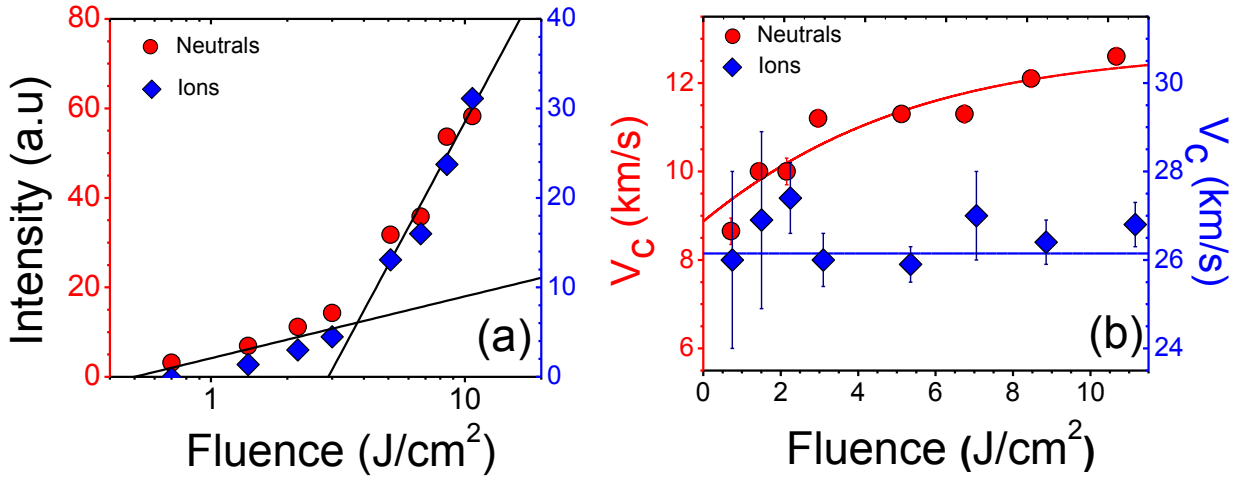

Figure 4.2: (a) Variation in emission intensity of copper plasma plume with fluence at a delay of 350 ns (ICCD gate width: 50ns) for atomic components (b) Average expansion velocity V_c of the various plume components as a function of the laser pulse fluence for atomic components. The lines are guide to the eye.

From the 2D images, one can analyze the variation of the plume center position as a function of delay, which shows a linear dependence. This analysis was carried out for delays in the range 200-800 ns for atomic components. Then, the slope of this position-time plot provides an estimate of the average velocity of the various ULA plume components along the normal to the target surface. The average velocity as a function of the laser pulse fluence is reported in Fig. 4.2(b), which shows a

rather weak dependence. In particular, the average velocity of the ion population is almost constant with the fluence, whereas for neutrals a slight increase is observed (see fig. 4.2(b)). The maximum average velocity of ions is ≈27 km/s, while for neutrals it is ≈13 km/s. The observed velocities are rather consistent with the results obtained by S. Noel et al [6] and Wang et al [10]. The higher velocity of ions can be explained as the result of interactions between charged particles and the built-in bipolar electrostatic field, which exists near the target surface in the very early stage of plasma formation and expansion [4, 5]. The slight rise of the average velocity of neutrals can be ascribed to the possible contribution of ionized species that recombine during the early phases of plume expansion, thus increasing the average velocity of this population. This interpretation is consistent with the partial overlap between the front of the neutral plume and the rear part of the ion plume observed in Figures 4.1(a) and 4.1(c). Moreover, the weak influence of the laser fluence on the average velocity of the various ULA plume populations, and the simultaneous increase of their emission suggest that the increase of energy released to the target mainly results in a raise of the amount of ablated material, which eventually gains a similar average expansion velocity.

4.1.2 Ion dynamics in ultrafast laser ablation

The Langmuir probe current signal provides an ion time-of-flight (TOF) signal that is proportional to both ion density, n_i, and ion flow velocity, u_i, through the following relationship:

$$I(t) = eAn_i(t)u_i(t) \tag{4.1}$$

where e is the electron charge, A is the probe collecting area, and t is the TOF measured relative to the arrival of the laser pulse. The zero time for the TOF measurement was provided by a fast photodiode that collects the laser light reflected off the target surface. Ion TOF profiles were recorded as a function of the probe angle θ for different values of the laser pulse fluence F. Each profile was acquired from an average of over 16 laser shots.

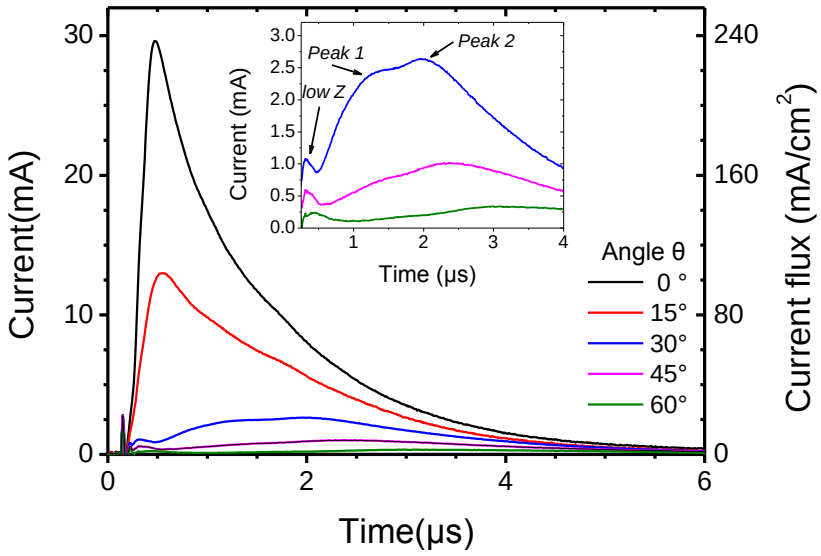

Figure 4.3: TOF ion signals for various angles θ relative to the target normal. Inset: Magnified image of the TOF ion profiles at selected angles showing the presence of various components.

Figure 4.3 shows typical ion TOF profiles recorded at various angles θ and a laser fluence F = 10.7 J/cm^2. We observe the following: a) the signal intensity is largest along the normal (θ = 0º) and progressively decreases with increasing angle, and b) the TOF profile leading edge moves toward longer TOF values as θ increases. These features suggest the presence of faster ions along the target normal. Similar behaviors are observed at lower fluence values. The inset in Fig. 4.3 shows an increase in ion TOF profiles recorded at larger angles, which indicates the presence of various components. Weaker features at TOF values below ~0.3 μs are due to residual low-Z contaminants [11, 12], as confirmed by firing a number of single laser shots at the same position on a stationary target. After the first shot, an intense peak with the same TOF value is observed, but the amplitude decreases when the next shots are fired, eventually reaching values comparable with those of Fig. 4.3. Given a rotating target with a repetition rate of several tens of Hz, appropriate conditioning of the target surface with a series of laser shots results in a negligible contribution of contaminants to the ablated plume species, which is in agreement with results of previous studies using plume spectroscopy techniques [10]. Signals obtained at very early TOFs decrease to values comparable with those observed for a stationary target after a number of laser shots has been fired. All measurements were obtained after appropriate target conditioning/cleaning procedures. The contribution of low-Z contaminants to the overall ion TOF signal is 0.1%, which is inconsistent with the contribution of low-Z species present in the target considering its high purity. The presence

of the low-Z peak can be explained by considering the diffusion of surface contaminants from the surrounding area into the cleaned laser spot, as reported by Williams et al. [12] under typical LA conditions. Note that the high quality of vacuum chamber used in our study reduces this contribution to nearly negligible levels [10].

With increasing duration of delays, two other features are observed in the ion TOF signals (indicated as peaks 1 and 2 in the inset in Fig. 4.3), further suggesting the presence of different components aside from the contaminant peak. For angles close to the target normal, two components are present in the form of a peak at a TOF of ∼0.5 μs and a shoulder of the signal at a TOF of ∼1.5–2.0 μs. The presence of more than one component in the ion plume produced in the ULA experiments of metallic targets has been previously reported by other authors [4, 13-15]. Zhang et al. observed two distinct ion populations in the energy spectrum of plasma plumes produced during ULA of Al and Ni targets with ∼80–100-fs Ti:Sapphire laser pulses, as measured by an ion energy analyzer ∼1m from the target surface [4]. The presence of differently charged ionization states of up to +3 has been reported for Al. Comparison with the ion probe signal recorded ∼10 cm from the target surface for Ni indicates overall agreement among ion kinetic energies. However, a significant overlap of the two components is recorded by the ion energy analyzer. The same authors attribute the more-energetic ion population to a combination of ambipolar field effects, Coulomb explosions, and nonlinear ponderomotive forces and the less-energetic ion population to a hydrodynamic component with ns pulses under similar conditions [4]. Double peak ion TOF profiles were also reported by Ye et al. [13], and Amoruso et al. [14] during ULA of metals (Ti, Cu, Au) with ≈80-100 fs Ti:Sa laser pulses. Double peak ion structures have been reported by Verhoff et al. using a Faraday cup detector positioned ∼14 cm from the target surface during ULA of Al with ∼40 fs Ti:Sapphire laser pulses [15]. Simultaneous measurements with a 6-ns pulse from a Nd:YAG laser do not reveal energetic components. Also other experiments with visible (∼250 fs, 527 nm), and ultraviolet (∼500 fs, 248 nm) fs laser pulses did not reveal the presence of a significant energetic component [16, 17]. The same experimental setup used here was exploited for previous experiments with laser pulses of ∼250 fs at 527 nm. Thus, any influence exerted by the experimental apparatus can be excluded. The pulse durations and fluences used in the two previous studies are very different, resulting in diverse levels of interaction. The average pulse intensity, I_L, is investigated in the interval $\sim(0.3–2)\times10^{12}$ W/cm^2 at 527 nm in a previous study, whereas I_L varies in the range $\sim(0.3–2)\times10^{14}$ W/cm^2 in the present study. This result suggests

that the generation of fast ions depends on mechanisms related to laser pulse intensity, as explained later.

The ion TOF profiles were also integrated to investigate the angular dependence of the ion charge flux collected by the probe. As the two ion peaks cannot be easily separated, the overall signal was evaluated except for the very minor contribution at early TOF due to low-Z contaminants. The angular variation of the charge flux is shown in Fig. 4.4(a). The curves are rather symmetric with respect to the target normal, although the maximum flux does not always occur at θ =0°, as a consequence of the limited mechanical precision of the probe holder. The charge flux was fitted with the angular distribution $F(\theta)$ predicted by the expansion model of Anisimov et al. [11, 18, 19] for the collection on a hemispherical surface:

$$F(\theta) = F_0\left(1+\tan^2(\theta)\right)^{3/2}\left(1+k_{zx}^2\tan^2(\theta)\right)^{-3/2} \tag{4.2}$$

where F_0 is the maximum flux value and k_{zx} is the asymptotic value of the longitudinal-to-transverse axes ratio of the semi-ellipsoidal shaped plume in the zx plane (see Fig. 4.1(b)). The parameter k_{zx} is related to the plume aspect ratio, and a larger value corresponds to a more forward-peaked expansion, with the angular full-width half maximum $\Delta\theta$ depending on k according to the following relation:

$$\Delta\theta = 2\arctan\sqrt{\frac{2^{2/3}-1}{k^2-2^{2/3}}} \tag{4.3}$$

In the fitting procedure the angle corresponding to the maximum intensity was left as a parameter, which always coincided with the nominal θ = 0° position, within a few degrees.

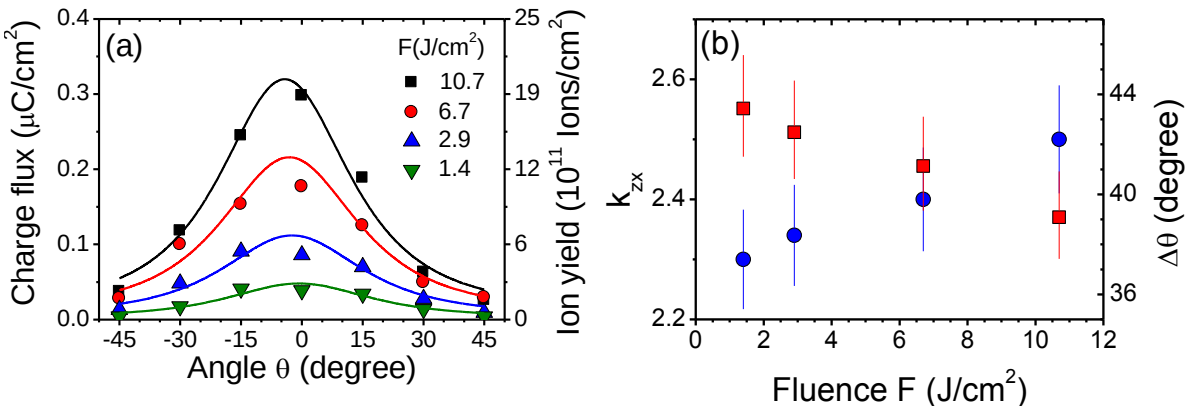

Figure 4.4: (a) Angular variation of the collected charge flux for different values of the laser pulse fluence F. (b) Aspect ratio, k_{zx} (blue dots), and corresponding angular widths (FWHM) $\Delta\theta$ as a function of laser pulse fluence F.

Fig. 4.4(b) reports the dependence of k_{zx} on the laser pulse fluence F. The rise of its value with F indicates a more forward-peaked ion plume at larger fluence, in agreement with previous reports [14]. The values of the corresponding angular width $\Delta\theta$ (FWHM) are also reported in Fig. 4.4(b). An angular width in the order of 20º is consistent with that reported for an Al LPP produced by ~40-fs Ti:Sapphire laser pulses [15]. In other reports [16, 20], however, somewhat narrower ion plumes were observed. This difference is ascribed to the smaller values of the laser beam spot size on the target used in our experiment, which lead to larger angular widths of the produced LPP, in agreement with model predictions [11, 18, 19]. In all cases, the angular distribution of the LPP ions is well described by the Anisimov model, with realistic parameters related to the specific experimental conditions.

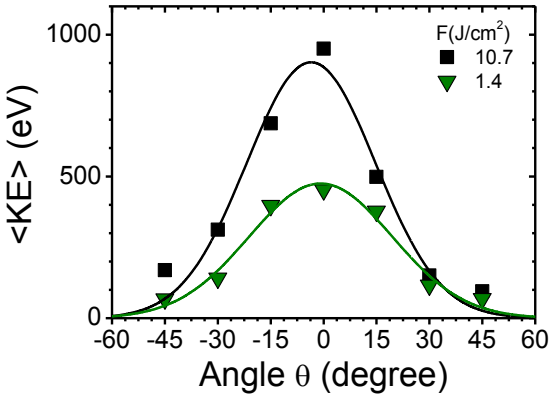

Figure 4.5: Angular variation of the ion average kinetic energy <KE> for two different values of the laser pulse fluence *F*. The curves are Gaussian fits to the experimental data.

From the ion TOF signals the ion average kinetic energy <*KE*> was calculated, and hence its angular variation was derived. <*KE*> was obtained as:

$$\langle KE \rangle = \frac{1}{2} m_{Cu^+} < u^2 > , \text{ with } \langle u^2 \rangle = \frac{\int \left(\frac{L_p}{t} \right)^2 I(t) dt}{\int I(t) dt} \qquad (4.4)$$

where <u^2> is the ions mean square velocity and L_p is the target-to-probe distance [21].

The angular variation of <*KE*> is reported in Fig. 4.5 for two values of the laser pulse fluence F. In both cases, the average ion energy in the direction normal to the target is greatest, indicating a forward-peaked distribution of average ion <*KE*>, that reaches values of several hundred eV. Moreover, going from 0° to ≈30° the value of average ion <*KE*> reduces by a factor of 6 at 10.7 J/cm^2, and 3 at 1.4 J/cm^2, respectively. This indicates that the majority of the ions are concentrated

in a rather narrow cone angle with respect to the target normal. In particular, the LPP ion plume has an angular width (FWHM) of ~36° at 10.7 J/cm^2, and ~41° at 1.4 J/cm^2, in agreement with the broadening of the distribution as the fluence decreases. These values are consistent with those observed for a LPP produced by ~40 fs Ti:Sa laser pulses irradiating an Al target [15]. The larger effect of the laser pulse fluence on the forward-focusing of the ions average kinetic energy with respect to the ion flux is consistent with more electrons forming the space-charge layer at higher laser intensity, resulting into stronger acceleration effects of the ions during the early stage of the ULA process in the forward direction.

We also analyzed the dependence of the ion plume features on the laser pulse duration, τ_L. Ion probe measurements were carried out at three laser-pulse durations (i.e. $\tau_L \approx 50$ fs, $\tau_L \approx 200$ fs and $\tau_L \approx 600$ fs), for a fixed-laser fluence of 8.5 J/cm^2. The angular distributions were all well described by the Anisimov model with $k_{zx} = (1.8 \pm 0.1)$ and the value of F_0 varied only within ±10%, which is comparable with the accuracy of the measurement. Therefore, our results indicated that ions plume characteristics, e.g., average velocity, collected charge, and angular width, are almost independent of the laser pulse duration for subpicosecond laser pulses.

We also carried out a similar analysis, i.e., both spectrally resolved ICCD imaging and ion dynamics using Langmuir probe on a semiconducting material to investigate general behaviors of ultrashort LA of solid targets. Preliminary results on a silicon target show the presence of a sizeable population of fast ions flying ahead of the main LPP neutral component. It is also noticed that the silicon ion angular distribution is well described by the model of Anisimov et al. [18, 22], which allows quantifying the aspect ratio of the LPP ions plume. The angular distribution of the ion flux shows a progressive narrowing at increasing fluencies. At fixed fluence, the angular profile of the ion flux is rather confined around the target normal, while the ions average velocity is broader. Nevertheless, the total energy of the ion flux is very focused in the forward direction, with a typical angular width of ≈20º for both copper and silicon.

4.1.3 Ambipolar Diffusion Model

A mechanism accounting for the generation of energetic ions in laser ablation is the rapid formation and expansion of a space-charge layer of electrons that creates a time-dependent ambipolar field, as discussed earlier by Zhang et al. [23] and Amoruso et al. [5] during laser ablation with fs Ti:Sa laser pulses at intensities comparable with those used in the present study. This layer forms as a consequence of the escape of energetic electrons at the plasma edge on

distances comparable to the Debye plasma length. These electrons set up a space charge-layer, which consequently accelerates a fraction of the plasma ions. On the contrary, the core of the plume, which is essentially neutral, undergoes a hydrodynamic expansion away from the target. Such a mechanism results in the double-component distribution observed in the ion TOF profiles: the high-energy component contains hot electrons and accelerated ions, while the second peak consists of thermalized ions and electrons expanding in vacuum. Such mechanism is more effective in accelerating the energetic ions in a narrow angle along the normal to the target surface, as suggested by the fact that their signal predominates for $\theta = 0°$, and 15° in Fig. 4.3, while progressively becoming lower than the second, slower component at larger angles.

An interesting point concerns the stage of the plume expansion at which the faster ions acquire their extra energy and momentum. Oguri et al investigated the early-stage dynamics of an Al ablation plume produced by 100 fs Ti:Sa laser pulses at intensities of 10^{14} W/cm^2 [3]. This study evidenced that a structured plume is already formed within the early stages of the LA process, and that the ions are slightly ahead of the neutrals already at 0.5 ns. By this time, these ions have achieved a final average expansion velocity of the order of 10^4 m/s, suggesting that the ion acceleration process takes place at very short times and distances. The authors suggest that the production of the ions can be related to optical field ionization followed by Coulomb explosion (CE) [24-26]. Nevertheless, in all cases where CE was clearly addressed, the laser fluence was below the macroscopic threshold for ablation, a condition sometimes indicated as 'gentle ablation', and the observed ion energy was of only few to tens of eV [24-26]. As this is not the case in our experimental conditions, CE cannot solely explain our findings.

We turn now to the mechanism of built-in bipolar electrostatic field formation and ambipolar diffusion in the early stage of the LPP formation [4, 13-15]. Such a mechanism involves the formation of a thin layer where the plasma neutrality is lost because of the escape of a discrete population of energetic electrons at the plasma edge over distances comparable to the Debye plasma length, λ_D. Such a mechanism can be very complicated to model for a transient plasma such as that produced during the LA process. Therefore, we consider a simplified model. The nascent plasma is described as a disk of area S (equal to the laser spot size on the target) and thickness z, with the charge homogeneously distributed. The plasma sheath from which electrons and ions diffuse ambipolarly is located at the plasma boundary along the target normal, and has thickness l_s. The rest of the plasma, from the target surface to $(z–l_s)$, is electrically neutral. We can approximate the front

sheath as an effective capacitor with a net charge $Q_n = e \times N_i \times (l_s/z)$ on each armature of area S, where N_i is the number of produced ions. The electric field in the sheath is $E = Q_n/(\varepsilon_0 \times S)$, where ε_0 is free-space permittivity. The average potential energy associated with this charge distribution is $U = 1/2(\varepsilon_0 \times E^2 \times S \times l_s)$. Hence, the net energy available per each ion can be evaluated as $\Delta E_{\text{ion}} \approx U/N_n$, where $N_n = Q_n/e$ is the net number of ions in the sheath. In our experimental conditions, the Anisimov model predicts that the 3D expansion starts when the plume has reached a thickness Z_0 of the order of ≈3 μm. For a typical expansion velocity in the one-dimensional (1D) stage of $\approx 10^3$ m/s [11, 27], this implies a duration of the 1D expansion of the order of ≈100 ps. Moreover, the number of ions varies from $N_i \approx 0.5 \times 10^{13}$ at $F \approx 2$ J/cm^2 to $N_i \approx 2 \times 10^{13}$ at $F \approx 10$ J/cm^2.

We consider that $l_s \approx \lambda_D \approx$ 1–10 nm in our experimental conditions. On the other hand, we can assume $z \leq Z_0$. An estimate for z ≈ (1–3) μm and $l_s \approx 5$ nm leads to an ion kinetic energy increase $\Delta E_{\text{ion}} \approx$ 1–300 eV, in agreement with the order of magnitude of the extra energy experimentally observed. Moreover, considering the observed extra momentum $\Delta p \approx 10^{-21}$ kg m/s, one can calculate a characteristic acceleration time $\Delta t_{\text{acc}} = \Delta p/(e \times E) \approx$ (50–160) fs, thus suggesting that ions in the sheath promptly accelerate to their final kinetic energy and a new front layer can form. This, in turn, points to a dynamic process by which small fractions of an increasing number of ions at the front edge of the nascent plasma plume get further energy. As the plasma expands in the 1D stage, z increases with time, and the gained energy decreases. This indicates that the amount of extra energy gained by this dynamic process should progressively reduce with time, and only a fraction of the produced ions are eventually accelerated. A further intriguing aspect evidenced by our simple approach is that ΔE_{ion} is directly proportional to N_i and inversely proportional to the laser spot size S, which can limit the effectiveness of the dynamic ambipolar process for larger spot sizes. This is in agreement with recent reports on fs LA of metals, where, for a number of ions comparable to that observed here, the energetic ion component is present for spot sizes $S \approx 10^{-5}$–10^{-4} cm^2 [5, 14, 15], while becoming negligible for $S \approx 10^{-3}$ cm^2 [11, 17]. In fact, the number of ions N_i depends on the laser-pulse fluence F [14, 17], which, in turn, depends on the maximum available energy, E_L, delivered by the laser source, and on the spot size S. At fixed energy, a smaller spot size can result in higher fluence, but with a reduced amount of total ablated material, and hence a smaller number of ions, N_i. As a consequence, the effectiveness of the dynamic ambipolar diffusion process in fs LA and the consequent generation of energetic ions in fs LPP results from the complex interplay of these experimental parameters.

4.2 The High Laser Intensity Regime

Here we discuss the extension of the previous study to the high fluence regime. The experiments were carried out at Purdue University, therefore the experimental parameters are slightly different from those used in the set of experiments presented in the previous section. In particular, the laser beam hits the target surface at normal incidence, and the charge collectors are located at larger distances from the target. Schematic of the experimental setup used is shown in Fig. 3.1 (a) & (b) and allows simultaneous measurements of plume features and expansion dynamics by means of a Langmuir probe (LP), a Faraday cup (FC) and spectrally resolved ICCD imaging. The details of experimental conditions are summarized in table 4.1.

Parameters	Specifications	Details
Laser System	Ti:Sapphire II 800 nm, ≈50 fs	[Details are given in table 3.1]
Investigated Fluence Regime	0.5 J/cm^2 – 75 J/cm^2 (Spot Size ≈100 μm)	Corresponding Intensity 1.6×10^{13} – 2.2×10^{15} W/cm^2
Pulse contrast	10^{-5}	No pre-pulse damage occurs on the target
ICCD (for direct and spectrally resolved imaging)	Princeton Instruments, Model PI-MAX	Details of spectrally resolved ICCD Imaging are given in sections 3.2.4 & 4.1.1
Langmuir Probe (LP)	Probe area: 12 mm^2 Bias voltage: -20 V	Positioned at 20º with respect to target normal Target to LP distance (L) = 6.5 cm For angular measurements L = 14 cm
Faraday Cup (FC)	Aperture area: 5 mm^2 Bias voltage: -32 V	Positioned 20º with respect to target normal Target to FC distance (L) = 6.5 cm
Targets	99.99+% pure	Mg, Al, Cr, Fe, Cu, and W

Table 4.1: Experimental details of the multidiagnostic analysis of ion dynamics in ULA of metals over a large fluence range, carried out at Purdue University.

In section 4.2.1 we discuss the variation of copper ion dynamics over a fluence range going from the ablation threshold F_{th} (≈0.5 J/cm^2) up to $F \approx 150 \times F_{th}$. The corresponding intensity varies in the range (≈1×10^{13} - 2×10^{15} W/cm^2). Then, in Sec. 4.2.2 we discuss the fluence dependence of the Cu ions angular distribution. Finally, in Sec. 4.2.3 we illustrate the results of an experimental

characterization of the ionic angular distribution for emission from several metallic targets carried out at a relatively high fluence of ≈66 J/cm^2.

4.2.1 Laser fluence dependence of the Cu ions plume

Figures 4.6(a) and 4.6(b) show the ion signals obtained from the LP and FC at several values of the laser pulse fluence, *F*. The TOF profiles registered by LP and FC show a similar variation as a function of the fluence, and the slight differences can be likely due to the different positions of the diagnostics, the dissimilar collecting area of their charge collectors, as well as minor spatial asymmetries in the plasma around the target normal.

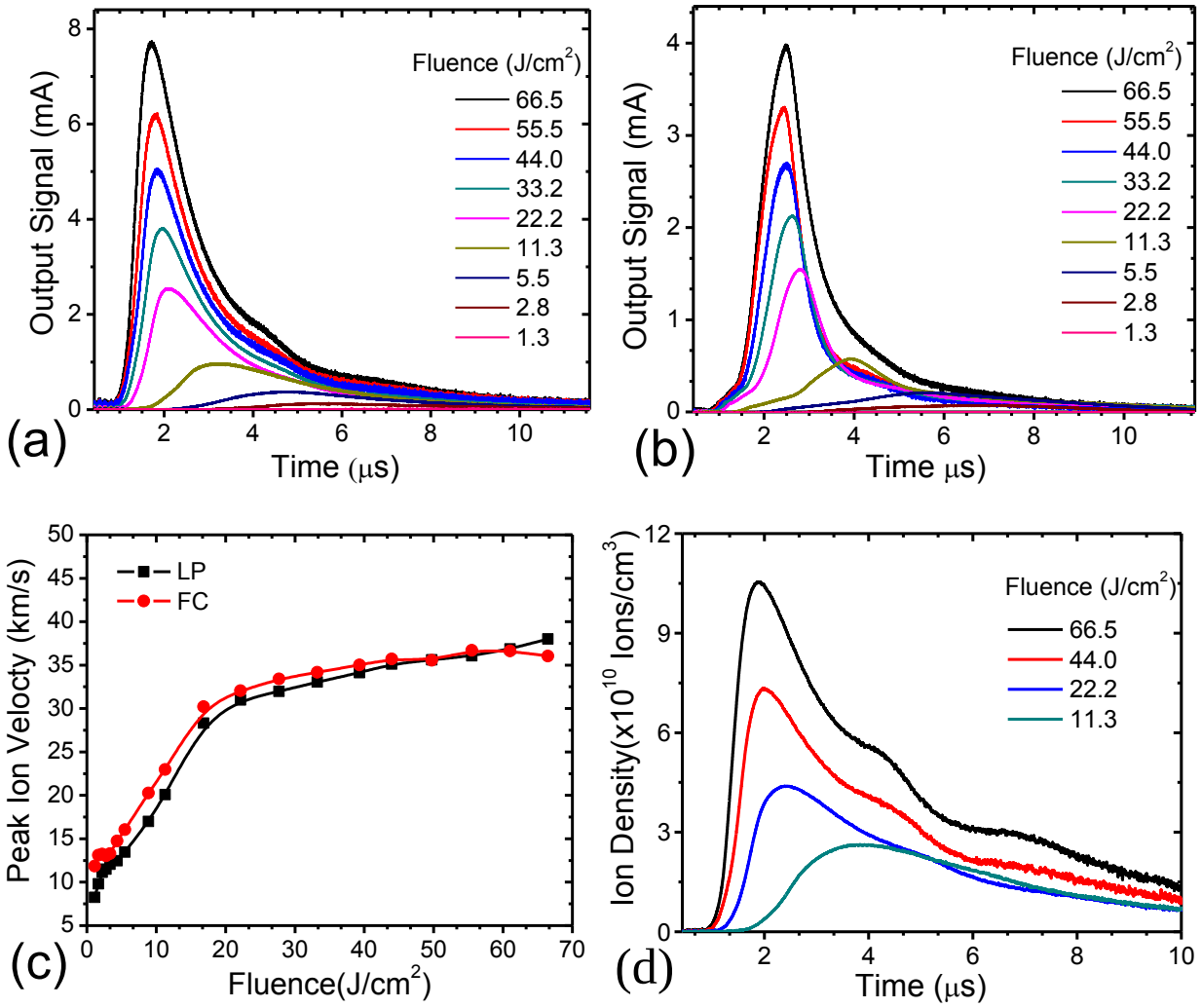

Figure 4.6: Copper ion TOF signals at different laser fluences registered by using (a) Langmuir probe and (b) Faraday cup. Panel (c) reports the copper ion peak velocity u_p as a function of fluence. Panel (d) shows the ion density temporal profile of the copper LPP ions obtained from LP measurements at various values of the fluence.

From Figs. 4.6(a) and 4.6(b) one can observe that both LP and FC signals show a peak that progressively shifts to a shorter time as the fluence F increases. This indicates a progressive rise of the ion peak velocity with F. Moreover, the variation of the ion peak velocity becomes gradually smaller at higher fluences, as suggested by the reduced rate of change at larger F. From the TOF profiles of Fig. 4.6(a) and 4.6(b), the variation of the ion peak velocity, $u_p = L/t_p$ (where t_p is the peak TOF), with fluence is derived, and reported in Fig. 4.2(c). One can observe that the two diagnostic techniques give similar results, and the u_p dependence on F shows two different regimes. At low fluences (F<17 J/cm^2), the peak velocity progressively increases with F, passing from ≈10 km/s at $F \approx 2$ J/cm^2, to ≈30 km/s at $F \approx 17$ J/cm^2. Then, it levels off at larger F suggesting the transition to another regime of ionic expansion.

Since charge-collection diagnostics as LP and FC lack species sensitivity, we also measured the plasma plume self-emission by ICCD-based fast imaging. Figure 4.7 shows the emission characteristics of direct and spectrally resolved ICCD images of the copper LPP. Figure 4.7(a) reports time resolved two-dimensional images of the LPP emission acquired at a delay of 200 ns, with a gate width of 20 ns, at $F = 77$ J/cm^2. The left image in Fig. 4.7(a) refers to the overall plume emission - namely, without any spectral filtering - while the central and right images of Fig. 4.7(a) report a spectrally filtered 2D image of the copper neutrals and ions, respectively. The intensity is plotted in linear scale and is normalized to the maximum value of the image. We observe a clear spatial splitting of neutrals and ions, with the charged plume component flying ahead of the neutral population. This is in good agreement with results obtained in the previous section (sec. 4.1.2), where we had investigated copper LPP only at moderate laser intensity. This, in turn, indicates that this characteristic behavior represents a general feature of fs ablation plasmas, which is present even at much larger fluences, up to about 150 times the fluence threshold. Moreover, it is worth observing that at the lower fluences investigated earlier [28], the ionic contribution to the overall emission was easily overlooked in the direct 2D images due to lower intensity of the ionic emission with respect to neutrals. Instead, in the left image of Fig. 4.7(a), we can easily recognize the important contribution of the front ionic component, which suggests an increased proportion of the ion population at a higher fluence of several tens of J/cm^2. Figure 4.7(b) shows the spatial profile of the emission intensity along the normal to the target surface as obtained from the images of Fig. 4.7(a) for overall plume, neutrals, and ions emission. The values of velocity corresponding to the

peak emission intensity are ≈26 km/s for ions and ≈8 km/s for neutrals, while the front velocity of ions is of the order of ≈50 km/s.

Since the image intensity is related to the density of the emitting particles, for the sake of comparison Fig. 4.6(d) reports some temporal profiles of the ion population measured with the LP in terms of the ion density $n_i(t) = I(t)/(eAu_i(t))$. One can observe that the ion front and peak velocity obtained from the image analysis is consistent with that indicated by the ion density profiles. For instance, in Fig. 4.6(d) the LP profile at $F \approx 67$ J/cm^2 reaches ≈10% of the peak value at ≈1.2 μs corresponding to an ion velocity of the faster ions registered by the LP of ≈55 km/s, while the peak velocity is ≈33 km/s. The good consistency indicates that LP and FC signals can be reliably associated to the copper ions plume registered by fast imaging.

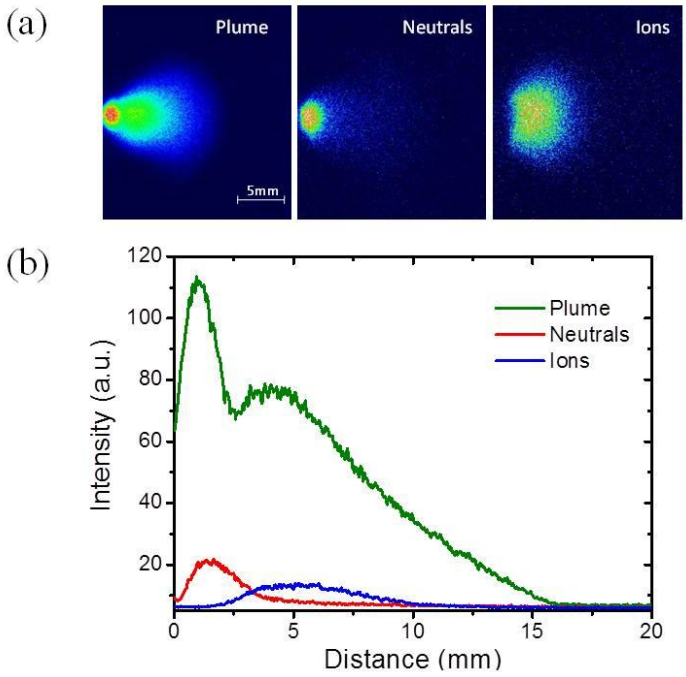

Figure 4.7: (a) Direct and spectrally resolved images of the copper LPP plume (left), neutrals (center) and ions (right); (b) spatial profile of the emission intensity along the normal to target surface, z. The images are acquired at a delay of 200 ns, with a gate width of 20 ns, at a laser fluence of 77.5 J/cm^2. The intensity of each image in panel (a) is normalized to its own maximum value.

We can also notice that the ion density profiles of Fig. 4.6(d) show the presence of more than one component at high fluence, while the spatial profile of the ion emission intensity in Fig. 4.7(b) is characterized by a relatively smooth variation. This can be rationalized by considering that the spectrally filtered image of the ion emission specifically refers to a population of singly charged

excited ions, which likely constitute the more abundant population of the positively charged LPP species. Nevertheless, at high fluence levels other ionic components with higher charge could contribute to the signal registered by the LP. The presence of more than one ionic component in ULA of metallic targets has been reported earlier [4, 13-15]. The more structured ion density profile at higher fluences can likely be due to the presence of these further contributions to the ion current registered by LP.

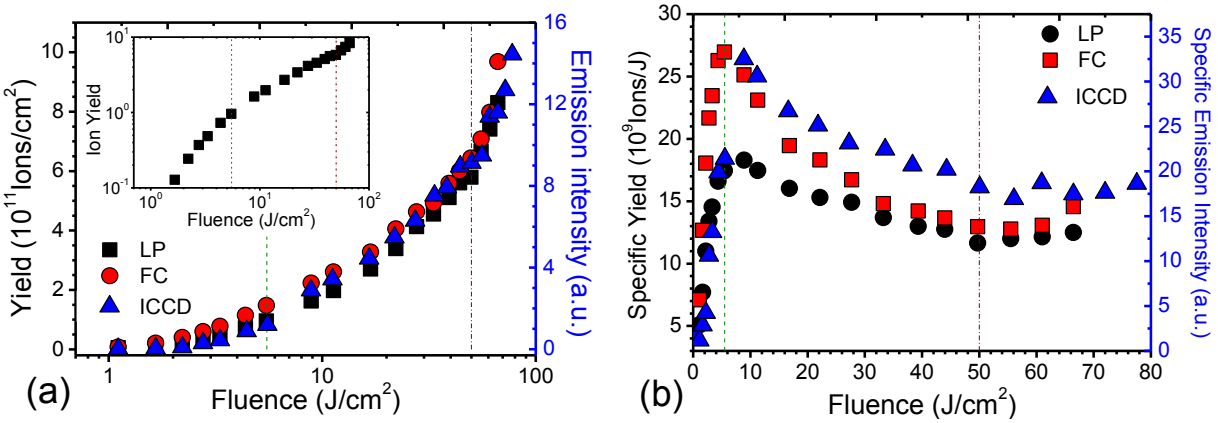

Figure 4.8: Copper ion emission yield (a) and specific ion yield (b) as a function of the laser fluence. In both cases the left axis represents the LP and FC measurements and the right axis represents the spectrally resolved ICCD imaging. The two vertical lines mark the transition between different regimes. The inset in panel (a) shows the LP data on a log-log plot.

By integrating the time of flight (TOF) signals, the total flux of positive ions collected on LP and FC can be obtained. Figure 4.8(a) reports the copper ion yield (ions/cm^2) as a function of the laser pulse fluence *F*. In Fig. 4.8(a), we also report the variation of the ion emission intensity with fluence as registered by fast imaging. In this case, the emission yield has been estimated by registering the ion emission over an interval of 1 μs and spatially integrating the image signal. The data are plotted on different vertical axes to facilitate the comparison. We observe that the three diagnostics provide a similar trend of the ion yield as a function of the fluence, corroborating the idea that singly charged ions constitute the main part of the positively charged plasma plume. The data of Fig. 4.8(a) shows an increasing behavior of the ion yield as a function of the fluence. The inset of Fig. 4.8(a) reports the LP data on a log-log plot and suggests that different dependences occur over the large fluence range investigated here. In particular, a first transition seems to take place at ≈4-6 J/cm^2 as evidenced by the presence of a knee and a reduction of the slope at larger fluences. Then, another change of slope can be discerned at ≈50 J/cm^2 indicating the transition to a

high-fluence regime. This effect is clearly visible in Fig. 4.8(b) which reports the variation of the specific ion yield, i.e. the yield per unit fluence, as a function of F. We observe a clear maximum in the specific ion yield at $F \approx$ 4-6 J/cm^2 followed by a rapid decrease at larger fluences. Then, a shallow minimum is discernible at $F \approx 50$ J/cm^2 with a reversal of the trend, which starts slightly rising again and marks the transition to the high-fluence regime. Hydrodynamic simulation of ULA of copper with 170 fs pulses at 800 nm were carried out by Colombier *et al*. to describe the experimental behavior of the ablation rate vs fluence, in the fluence range 1-35 J/cm^2 [29], obtaining a fairly good agreement with experimental data. Their simulations predict the presence of a maximum in the specific removal rate at about 5 J/cm^2 evidencing the occurrence of a critical behavior which was related to the complex relaxation dynamics of the irradiated target. This effect can be correlated to the observation of a maximum in the specific ion yield in Fig. 4.8(b), addressing its origin in the optimal conditions for ablation efficiency that also leads to an effective production of copper ions in the plume. In this respect it is worth noticing that previous studies have demonstrated a very good consistency between ion yield, optical emission intensity and overall ablation rate dependence on laser fluence in ULA of metallic targets [6-8].

The existence of optimal conditions of ablation efficiency have been observed in various experiments [29-33]. In particular, the fairly good agreement with the prediction of Colombier *et al*. [29] suggests that the fluence variation of the ion yield observed for low and moderate fluences (F<50 J/cm^2) is directly related to the two different regimes of target decomposition predicted by the two-temperature model description of target heating and the consequent electron-lattice energy transfer dynamics and material decomposition. Instead, the third regime observed at fluences larger than ≈50 J/cm^2 could be associated to the processes involved in ion emission by ULA at very high intensity. In this respect, it is worth noticing that Bacghi *et al*. [34] studied ion and x-ray emission from Cu targets induced by 50 fs Ti:Sa pulses at intensity going from $\approx 5\times10^{15}$ to 6×10^{16} W/cm^2, observing an ever-increasing trend of the ion yield with fluence. The corresponding fluence ranges from 250-3000 J/cm^2. It is likely that the transition observed at ≈50 J/cm^2 may represent the progressive passage towards the low fluence side of this high-intensity regime of ULA, where ion dynamics is related to the generation of hot electrons and sheat formation in the early stage of LPP production [34]. The diverse regimes of ion emission observed in Fig. 4.8 can be useful to select the best experimental conditions for any specific application, as for example material processing, film deposition or ion beam generation by ULA.

4.2.2 Laser fluence dependence of the Cu ions angular distribution

The angular distributions of copper ion yield at different fluences are shown in Fig. 4.9(a) It seems clear that the ionic angular distribution is well described by the Anisimov model for laser fluences up to a moderate value of ≈11 J/cm^2, and that its angular width progressively decreases with fluence (see Fig. 4.9(b)). This is in agreement with previous reports for laser ablation at low and moderate fluences [11, 22, 28], and with the experimental findings discussed in section 4.1. Instead, at larger fluence the ions plume follows the Anisimov curve only in a relatively narrow region of about 40° (from −20° to + 20°) around the normal to target surface, but a secondary ionic contribution seems to form a broader shoulder at larger angles. This result indicates that the transition to a regime of higher fluences already observed in Fig. 4.8 also affects the angular distribution of the produced ions. While the angular width of the central part at low angles derived from the Anisimov formula tends to level off at larger fluence, the angular distribution at larger angles slightly broadens suggesting an opposite trend with respect to the forward peaking with fluence observed for low and moderate laser fluences (F≤10 J/cm^2). Additional investigations are needed to further clarify this aspect of the ion plume behavior at relatively large fluence of several tens of J/cm^2.

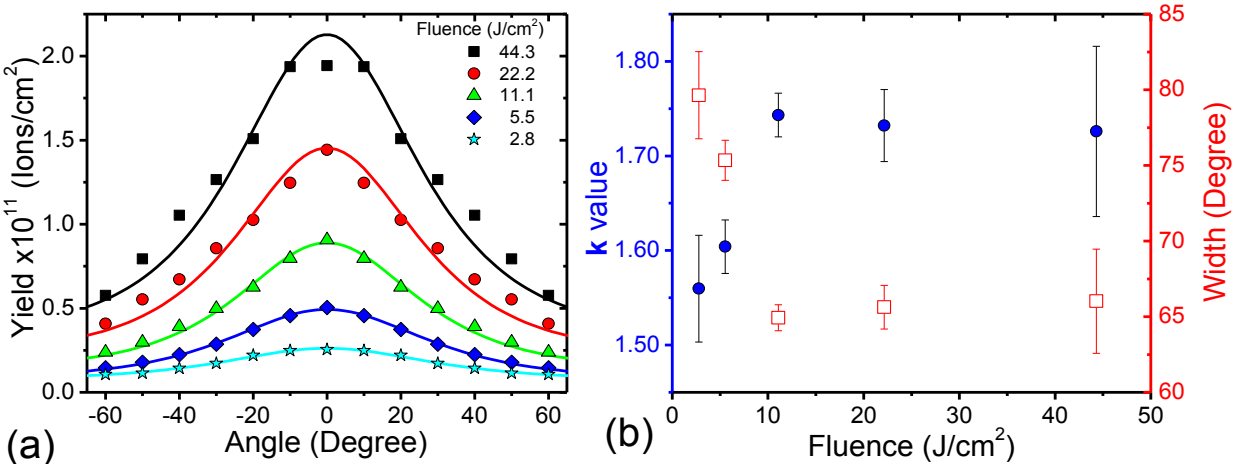

Figure 4.9: (a) Angular distribution of copper ion yield at different laser fluences. The solid curves are fits to Anisimov model angular distribution (Eq. (4.2)); (b) k value and corresponding angular width Δθ as obtained from Eq. (4.3), vs. laser fluence.

4.2.3 Ion angular distribution for different metallic targets

To further explore the properties of ion plumes produced in the high fluence regime, we also carried out an experimental characterization of the angular distribution of ion flux for six different

metals (Mg, Al, Cu, Fe, Cr, W), at a fixed fluence of 66 J/cm^2. Fig. 4.10(a) reports the angular distribution of the ion yield registered for the different solid targets. We notice that elements with low Z (i.e., Mg and Al) exhibit a larger ion flux along the normal to the target surface. Moreover, their angular distribution shows a very narrow component in the range (−30° – +30°), accompanied by a much broader contribution at larger angles. The forward component seems to reduce progressively by passing from the volatile elements Mg and Al, to the refractory metals Cr and W, while the broader fraction is present in all cases. In this trend, Cu seems to behave differently, with the lower amount of ions produced.

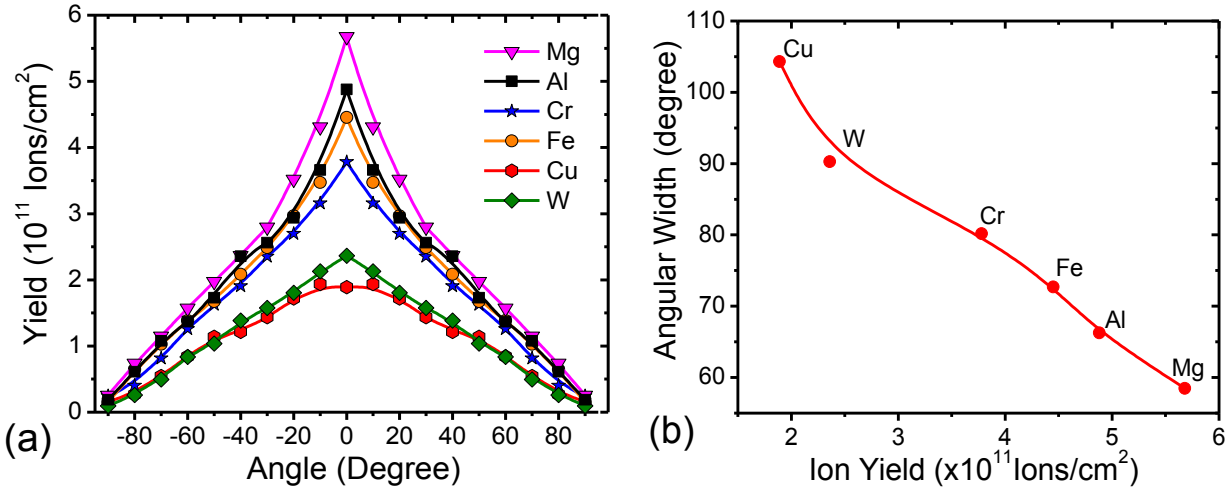

Figure 4.10: (a) Angular distribution of the ion yield for a selected number of elemental metallic targets, at fixed laser fluence of 66 J/cm^2. (b) Ion angular width at FWHM as a function of ion emission yield registered for the different metals. The lines are guides to the eye.

Farid *et al*. noticed that the ion yield from laser-produced plasmas strongly depends on the sublimation energy during ns laser ablation of metal targets [35]. Thestrup *et al*. studied the variation of the number of ablated atoms per pulse from many elemental metals during UV nanosecond laser ablation at 355 nm [36]. They evidenced an interesting correlation with the melting point of the element, considered as a measure of their volatility [36]. In particular, a general decreasing trend of the number of ablated atoms as a function of the element volatility was observed. Nevertheless, the same authors also pointed out that the number of ablated atoms varied strongly from one element to another, which indicates that one single physical parameter cannot rationalize the complex dependence of the ablation rate. Therefore, the indication of such kind of reliance are often qualitative, but can provide interesting general hints on the underlying mechanisms of laser ablation. A similar general trend was also observed for the total ion yield of a

selected number of metals, which can be justified by considering the rather low variability of the ionization potential. Table 4.2 reports some physical properties of the metals investigated in the present study, and a decreasing trend of the collected ion yield with melting point is generally observed also in our case (see Table 4.2 and Fig. 4.10(a)), with the exception of copper. We ascribe this inconsistency to the much higher reflectivity of copper at 800 nm [37]. The high value of the reflectivity likely reduces the laser energy coupling to the target and the corresponding ablation rate, thus producing a corresponding lower amount of ions with respect to the other metals. Then, the higher ion yield we observe for volatile metals is ascribed to the corresponding larger amount of ablated material.

Fig. 4.10(b) reports the ion angular width as a function of the peak ion emission yield registered for the different metals, evidencing another intriguing aspect of the ionic expansion dynamics. We observe an interesting reduction of the angular width as a function of the peak ion yield, Y_0. This, in turn, suggests a direct connection between the ion plume angular shape at large distance from the target surface, and the total amount of charged species in the plasma. The enhancement of the forward-directed character of an ion plume with increasing ion yield in Fig. 4.10 likely points to space-charge effects and other complex mechanisms occurring during fs laser ablation plasma formation and expansion in the high fluence regime. This, in turn, leads to a regime of ion plume expansion dynamics that cannot be described by a gas-dynamics approach as that of the Anisimov model, as already suggested in sect. 4.2.3, and a more complex modeling should be developed to portray the ion angular distribution in the high fluence regime.

Table 4.2: Some physical properties of the selected metals: A, atomic weight; T_m, melting point; R, reflectivity at ≈800 nm, normal incidence; IP, ionization potential [37]. Y_0 is the peak value of the ion yield registered along the direction normal to the target surface.

Element	**A (u)**	**T_m (K)**	**R (%)**	**IP (eV)**	**Y_0 (10^{11} ions/cm^2)**
Mg	24.30	923	-	7.65	5.7
Al	26.98	933	86.8	5.99	4.9
Cr	51.99	2180	56.8	6.77	3.8
Fe	55.84	1811	56.12	7.90	4.5
Cu	63.54	1357	96.3	7.73	1.9
W	183.84	3695	49.6	7.86	2.4

4.3 Conclusive remarks

We have carried out a comprehensive study on femtosecond laser ablation of a pure copper target in both a moderate (0.5 J/cm^2–10 J/cm^2) and a high fluence (0.5–75 J/cm^2) regime. Our analysis clearly shows the presence of a sizeable population of fast ions flying ahead of the main LPP neutral component, which becomes still more marked for the high fluence case. A simple model indicates that the formation of the fast ion component can be explained in terms of a dynamic ambipolar diffusion process occurring in the early stage of the LPP formation.

The fluence dependence of ion yield shows the presence of three different regimes. The first transition occurs at about 5-6 J/cm^2 and a maximum in the specific ion yield is observed at such fluence. Thus, our experimental findings in the first two regimes (i.e. from ablation threshold up to a fluence $F \approx 50$ J/cm^2) can be rationalized in the frame of the two-temperature model description of the fs laser-target interaction and subsequent material decomposition mechanisms. The transition occurring at $F \approx 50$ J/cm^2 is ascribed to the progressive passage towards a high-intensity LPP generation, where other complex mechanisms start playing a role.

We have also observed that the ion angular distribution is well described by the Anisimov expansion model [18] up to a laser fluence of ≈10 J/cm^2, in good agreement with previous reports. At larger fluences a progressive broadening of the ionic angular distribution occurs at larger angles.

Finally, we have studied the angular distribution of the ion flux for six different metals (Mg, Al, Cr, Fe, Cu, and W), in the high-fluence regime at $F = 66$ J/cm^2. Interestingly, the ion emission from the light metals generally shows a narrow, forward peaked distribution and high peak ion yield compared to the heavier ones.

The results of this extensive investigation on the ions generated in ULA of metallic targets can help in selecting appropriate experimental conditions for applications of ULA plumes in different fields, like e.g. ion physics and materials science.

References

[1] J.M. Liu, Opt. Lett. 7, 196 (1982).
[2] B. Doggett and J. G. Lunney, J. Appl. Phys. 105, 033306 (2009).
[3] K. Oguri, Y. Okano, T. Nishikawa, H. Nakano, Phys. Rev. B 79, 144106 (2009).
[4] Z. Zhang, P.A. VanRompay, J.A. Nees, P.P. Pronko, J. Appl. Phys. 92, 2867 (2002).
[5] S. Amoruso, X. Wang, C. Altucci, C. de Lisio, M. Armenante, R. Bruzzese, N. Spinelli, R. Velotta, Appl. Surf. Sci. 186, 358 (2002).
[6] S. Noel, J. Hermann, T. Itina, Appl. Surf. Sci. 253, 6310 (2007).

[7] N.N. Nedialkov, P.A. Atanasov, S. Amoruso, R. Bruzzese, X. Wang, Appl. Surf. Sci. 253, 7761 (2007).
[8] S. Amoruso, R. Bruzzese, X. Wang, N.N. Nedialkov, P.A. Atanasov, J. Phys. D. Appl. Phys. 40, 331 (2007).
[9] K. Furusawa, K. Takahashi, H. Kumagai, K. Midorikawa, M. Obara, Appl. Phys. A 69, S359 (1999).
[10] X. Wang, S. Amoruso, J. Xia, Appl. Surf. Sci. 255, 5211 (2009).
[11] T. Donnelly, J. G. Lunney, S. Amoruso, R. Bruzzese, X.Wang, and X. Ni, J. Appl. Phys. 108, 043309 (2010).
[12] G. O. Williams, G. M. O'Connor, P. T. Mannion, and T. J. Glynn, Appl. Surf. Sci. 254, 5921 (2008).
[13] M. Q. Ye and C. P. Grigoropoulos, J. Appl. Phys. 89, 5183 (2001).
[14] S. Amoruso, X. Wang, C. Altucci, C. de Lisio, M. Armenante, R. Bruzzese, and R. Velotta, Appl. Phys. Lett. 77, 3728 (2000).
[15] B. Verhoff, S. S. Harilal, and A. Hassanein, J. Appl. Phys. 111, 123304 (2012).
[16] T. Donnelly, J. G. Lunney, S. Amoruso, R. Bruzzese, X. Wang, and X. Ni, Appl. Phys. A 100, 569 (2010).
[17] B. Toftmann, B. Doggett, C. Budtz-Jørgensen, J. Schou, and J. G. Lunney, J. Appl. Phys. 113, 083304 (2013).
[18] S. I. Anisimov, D. B¨auerle, and B. S. Luk'yanchuk, Phys. Rev. B 48, 12076 (1993).
[19] S. I. Anisimov, B. S. Luk'yanchuk, and A. Luches, Appl. Surf. Sci. 96–98, 24 (1996).
[20] P. T. Mannion, S. Favre, C. Mullan, D. S. Ivanov, G. M. O'Connor, T. J. Glynn, B. Doggett, and J. G. Lunney, J. Phys. Conf. Ser. 59, 753 (2007).
[21] T. Donnelly, B. Doggett, and J. G. Lunney, Appl. Surf. Sci. 252, 4445 (2006).
[22] Xiaochang Ni, K.K. Anoop, X. Wang, D. Paparo, S. Amoruso, R. Bruzzese, Appl. Phys. A, Volume 117, Issue 1, pp 111-115 (2014).
[23] Z. Zhang, P. A. Van Rompay, J. A. Nees, C. A. Stewart, X. P. Pan, L. Fu, and P. P. Pronko, Proc. SPIE 3935, 86 (2000).
[24] Hashida M, Namba S, Okamuro K, Tokita S and Sakabe S, Phys. Rev. B 81, 115442 (2010).
[25] Dachraoui H and Husinsky W, Phys. Rev. Lett. 97, 107601 (2006).
[26] Vella A, Deconihout B, Marrucci L and Santamato E, Phys. Rev. Lett. 99, 046103 (2007).
[27] Povarnitsyn M E, Itina T E, Kishchenko K V and Levashov P R, Phys. Rev. Lett. 103, 195002 (2009).
[28] K K Anoop, X. Ni, X. Wang, S. Amoruso and R. Bruzzese, Laser Phys. 24, 105902 (2014).
[29] J. P. Colombier, P. Combis, F. Bonneau, R. Le Harzic, and E. Audouard, Phys. Rev. B 71, 165406 (2005).
[30] S. Amoruso, R. Bruzzese, C. Pagano, X. Wang, Appl. Phys. A 89, 1017 (2007).
[31] X. Zhao and Y. C. Shin, J. Phys. D: Appl. Phys. 46 335501 (2013).
[32] A. M. Komashko, M. D. Feit, A. M. Rubenchik, M. D. Perry, P. S. Banks, Appl. Phys. A 69, S95 (1999).

[33] J. Hermann, S. Noël, T. E. Itina, E. Axente, M. E. Povarnitsyn, Laser Phys. 4, 374 (2008)
[34] S. Bagchi, P. Prem Kiran, M.K. Bhuyan, S. Bose, P. Ayyub, M. Krishnamurthy and G. Ravindra Kumar, Appl. Phys. Lett. 90, 141502 (2007).
[35] N. Farid, S. S. Harilal, H. Ding, and A. Hassanein, Physics of Plasmas 20, 073114 (2013).
[36] B. Thestrup, B. Toftmann, J. Schou, B. Doggett, J. G. Lunney, Appl. Surf. Sci. 197–198, 175 (2002).
[37] W. M. Haynes and D. R. Lide (Eds.), CRC Handbook of Chemistry and Physics: A Ready-Reference Book of Chemical and Physical Data (Boca Raton, CRC, 2010).

Chapter 5

Nanoparticles Generation in Ultrashort Laser Ablation

5.1 Introduction

The interaction of ultrashort laser pulses with solid target has generated a lot of interest in both basic research and technological applications. The direct ejection of nanoparticles (NPs) is one of the prominent features of ultrashort laser ablation (ULA) and has proved its potential applications in optical, magnetic, and electronic materials [1-4]. This phenomenon is related to the capability of inducing non-equilibrium, extreme states in the irradiated material whose relaxation dynamics allows the generation of specific thermodynamic conditions during the decomposition stage, which eventually result in NP formation [5-8]. It has been observed that during ULA the laser produced plume (LPP) splits into two components, a faster-moving atomic component and a slower one, constituted of nanoparticles of the target material. Typically, NPs constitute the major part of the material blowoff produced in ULA of a metallic target, the atomic plume accounting for only 10%–20% of the total ablated mass [3, 9, 10]. Therefore, ULA of metals in vacuum is among the most promising prospective techniques for the preparation of NPs and NPs-assembled media.

In this chapter the process of nanoparticles formation is briefly presented from the point of view of both the main experimental features and the theoretical models describing it. The main emphasis is given to the investigations carried out to analyze the role of laser pulse fluence on expansion dynamics and size distribution of the NPs produced by irradiating a pure copper target with ultrafast laser pulses in high vacuum. The experiment and theoretical investigations are performed in the moderate fluence regime (1-10 J/cm^2), which is widely used both in basic research and a number of applications [11, 12]. The better control of NPs shape, size distribution and its reproducibility is a challenging task via laser ablation method. There are contradictory experimental results, and theoretical predictions exist on the role of laser pulse fluence on the process of NPs generation and their final properties [4, 8, 13-15]. For example, Eliezer et al. studied the generation of Al NPs by irradiating a 100 nm thick Al foil on a transparent heat-insulating CaF_2 glass with 50 fs Ti:Sa laser pulses, analyzing the NPs deposited on a silicon substrate held at 28mm from the target surface [4]. They reported that both the total number of the Al NPs per unit area, and the NPs average dimension reduce as the laser pulse fluence increases. Moreover, hydrodynamic modeling of silicon fs laser ablation coupled to fragmentation theory also suggests a possible reduction of the

NPs size with fluence [13]. These results seem to establish that it should be possible to exercise some control over the size of NPs by varying the laser fluence. In contrast, a very weak or negligible dependence of the NPs size and size distribution was observed for different metallic bulk targets (Au, Cu, Ni, etc) [8, 14]. In the course of this thesis, we took a step forward to clarify this scenario by considering both experimental and theoretical investigation of ULA of bulk copper with special emphasis on the NP generation process and their size characterization.

This chapter includes different features of NPs generation in ULA and its possible applications. Section 5.2 details the expansion dynamics of produced copper NPs plumes, which is analyzed by time-resolved imaging of its broadband optical emission with fast-gated ICCD. Section 5.3 details the experimental investigation of copper NPs deposition in high vacuum conditions. An atomic force microscope (AFM) in tapping mode was used for size and shape characterization of deposited NPs. In section 5.4, a theoretical investigation of ULA of a bulk copper target with particular emphasis on the NPs generation process and to their size characteristics is presented. In the theoretical investigation, the ablation process of copper is studied by exploiting a hybrid atomistic-continuum model that combines molecular dynamics (MD) simulations with the two-temperature model (TTM) for the description of the laser excitation and the subsequent transfer of the electrons energy to the lattice [16]. This computationally expensive and time consuming MD-TTM simulation was carried out at Regroupement Québécois sur les Matériaux de Pointe (RQMP), Département de Physique, Université de Montréal. The theoretical outcomes obtained from MD-TTM simulations are compared with the experimental results presented in sections 5.2 and 5.3. Finally, Section 5.5 comprises two examples of the characteristics of NPs-assembled films for applications in the field of bio-sensing, via deposition of gold NPs on a quartz crystal microbalance electrode, and in photoelectrochemical cells (PEC), via deposition of TiO_2 NPs on a photoanode.

5.2 Imaging of Copper Nanoparticles Emission

A schematic of the ultrashort laser ablation setup used for NPs imaging and deposition in high vacuum condition is shown in figure 3.5. Here the experimental parameters are the same of section 4.1.1. Since the NPs plume evolution spans microseconds after laser irradiation, we have imaged its characteristic broadband emission at longer delays of 1-100 μs. Fig. 5.1 shows 2D images of the copper NP plume self-emission registered at different delays after the laser pulse, and for two values of the laser pulse fluence: F = 2.2 J/cm^2 and F = 9.9 J/cm^2. In each image, the emission intensity is normalized to its own maximum value and plotted in linear scale. z = 0 marks the

position of the target surface. From Fig. 5.1, it is clear that the NP plume evolution is entirely different from that of the atomic part. It is also observed that NPs are very slowly moving particles, and even at a very long delay of 50–100 μs, the NP plume is still attached to the target surface while progressively decreasing in intensity.

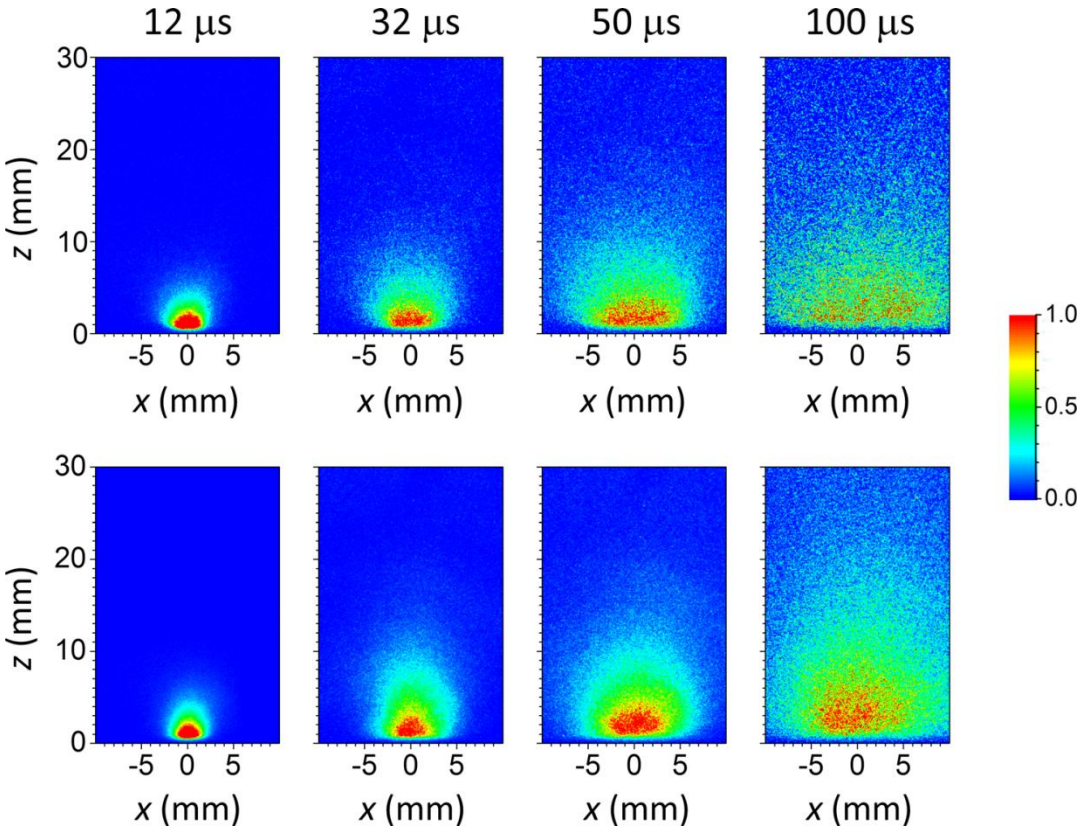

Figure 5.1: Snapshots of the copper NPs plume evolution with delay τ after the laser pulse, for two values of the laser pulse fluence: F = 2.2 J/cm^2 (upper panel) and F = 9.9 J/cm^2 (lower panel). The value of the delay τ is reported on the top of the images. In each image, the position (x = 0, z = 0) marks the laser spot on the target. For each image, the intensity is normalized to its own maximum value and is plotted in linear scale. A gate width of 10, 10, 25, and 25 μs was used going from left to right.

Analysis of 2D images in Fig. 5.1 gives further information on spatio-temporal evolution of the NPs emission. Fig. 5.2(a) shows the spatial profile of the emission intensity from an early stage of laser produced copper plasma performed at ≈10 J/cm^2. The inset graph shows the status of the same plume at 12 μs. That is, front atomic components are almost completely decayed or have moved away from the ICCD capturing window by this time. In order to concentrate our study on NPs plume emission, we have registered images only at longer delays. From the 2D images, one can analyze the variation of plume center position as a function of delay, which shows a linear dependence. This analysis was carried out in the interval 8-28 μs, and the slope of this position-time

plot provides an estimate of centre-of-mass velocity, v_{cm}, of the NPs component. Fig. 5.2(b) shows the v_{cm} of the NPs plume as a function of laser fluence (solid red circles). The NPs velocity is approximately 65 m/s and is almost independent of fluence in the investigated range (≈1-10 J/cm^2). The obtained value is rather consistent with the results obtained by Noel et al [8]. Fig. 5.2(b) also represents the NP plume emission intensity as a function of fluence (solid blue squares). The intensity was obtained by spatially integrating 2D images, registered at 12 μs (gate width 10 μs) after laser irradiation. Two different regimes are observed in the low- and high-fluence regions, with a crossover at about 3 J/cm^2 (≈6 × F_{th}). This is in agreement with the theoretical predictions of both TTM, and MD simulations [17, 18].

The existence of these two regimes is typical of ULA, and can be interpreted as a transition from a condition of energy absorption occurring in a region of the order of the material optical skin depth, to a situation of energy distribution regulated by the electron thermal diffusion length [18], as already discussed in section 4.1.1 It is interesting to note that an increase in the laser fluence leads to a larger emission, as a consequence of the increase of the amount of ablated material [8, 10, 17, 19, 20]. The fluence increase also rises the plume temperature that further promotes the enhancement of emission intensity with the fluence.

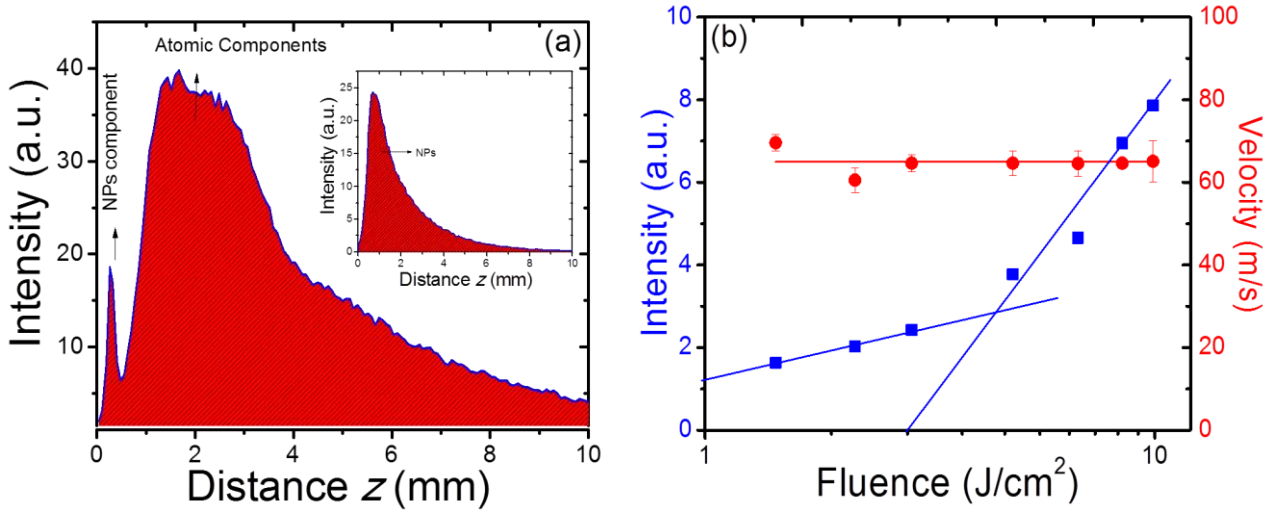

Figure 5.2: (a) Spatial profile of the copper ULA plume emission intensity along the normal to target surface, z, at a delay of 150 ns with laser fluence $F \approx 10$ J/cm^2. The peak at low distance in the spatial profile of the overall plume is due to the NPs emission. The inset graph shows the plume emission at 12 μs that is entirely due to NPs. (b) Variation in emission intensity of copper NPs plume with fluence (solid blue squares) and center-of-mass velocity (solid red circles), v_{cm}, of the NPs plume as a function of the laser fluence, F.

5.3 Deposition of Copper Nanoparticles

The experimental configuration used for deposition of copper NPs is shown in figure 3.6. The produced NPs were collected on a freshly cleaved mica substrate located at a distance of 45 mm in front of the pure copper target. Low-density deposits were obtained by appropriately tuning the number of laser pulses for each laser fluence, in order to avoid NPs coalescence and overlap, which eventually prevents a reliable determination of the NPs size characteristics. Different AFM images were taken from multiple positions of the deposited area for size characterization of many NPs, typically several hundreds. The NPs generated by ULA usually present an oblate shape with the major cross section parallel to the substrate surface [3, 4, 21, 22]. Hence, we measured the equivalent spherical diameter (*ESD*) of NPs for size characterization.

We have performed deposition and size characterization of copper NPs for different values of laser fluences in the interval ≈1-10 J/cm^2. The AFM images and the corresponding cumulative distributions of depositions obtained at four different laser fluences are shown in figure 5.3. As an example, consider the size histogram of *ESD* and its cumulative distribution, at F = 2.9 J/cm^2. One can observe that the *ESD* histogram is asymmetric, presenting a majority (≈70%) of small NPs with sizes lower than ≈10 nm, and a minority of large NPs in a long tail of larger sizes. In fact, from the cumulative distribution one can estimate a median (i.e., the *ESD* value below which 50% of the NPs *ESD* are counted) $ESD_m \approx 5$ nm. Moreover, 90% of the NPs show an *ESD* lower than $ESD_{90\%} \approx 21$ nm, while the other 10% is mostly characterized by NPs with an *ESD* of several tens of nm, and only a very limited fraction (≤ 1%) reaches an *ESD* of the order of ≈100 nm.

Fig. 5.4 reports the variation of $\langle ESD \rangle$, ESD_m, and $ESD_{90\%}$ with laser fluence. One can observe that the values of these parameters are slightly scattered around average values, indicated by a dash-dot line in Fig. 5.4, without evidencing any specific trend. In Fig. 5.4, for each parameter, a gray stripe has been drawn illustrating the range of values going from $-\sigma$ to $+\sigma$ around the mean value of the parameter, σ being the standard deviation of the observed values.

The stripes fairly well represent both $\langle ESD \rangle$, ESD_m, while $ESD_{90\%}$ values are a bit more scattered. This is likely due to the low number of counts in the *ESD* histogram at large size values. Therefore, within the limits of the experimental errors and using limited statistics, the results of this NPs size characterization indicate that the laser fluence does not significantly affect the size distribution of the NPs produced by ultrashort laser ablation of a bulk copper target, in an investigated fluence range going from $\approx 2 \times F_{th}$ to $\approx 20 \times F_{th}$.

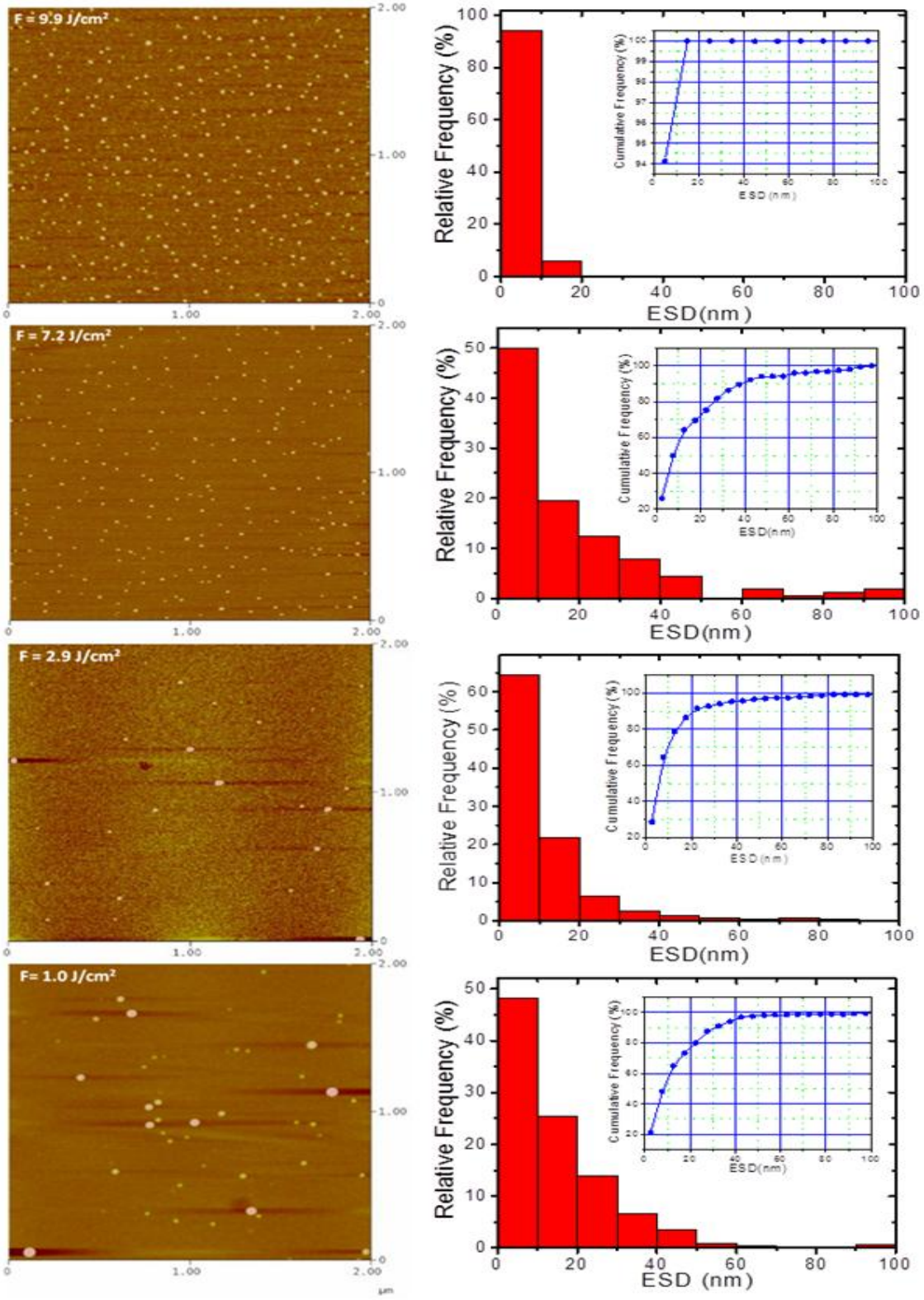

Figure 5.3: Typical AFM images (2 μm × 2 μm) of copper NPs deposited on freshly cleaved mica substrate for laser pulse fluences F = 9.9 J/cm^2, F = 7.2 J/cm^2, F = 2.9 J/cm^2, and F = 1.0 J/cm^2. The size histogram and cumulative distribution of NPs *ESD* is shown on the right side of each image.

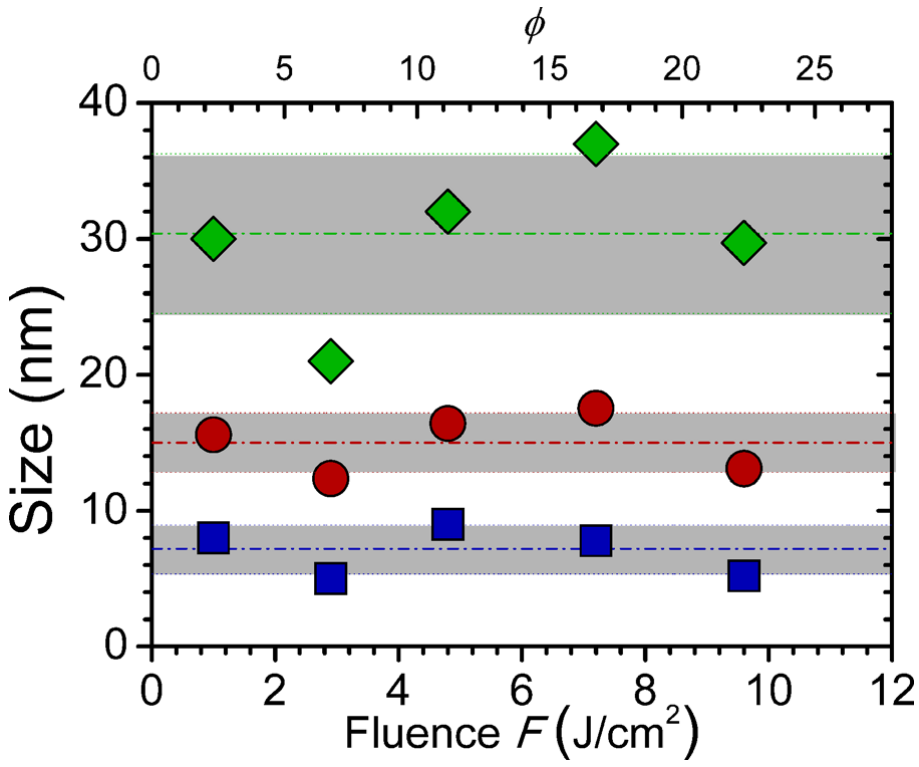

Figure 5.4: Variation of the NPs ESD size distribution parameters <*ESD*> (circle), ESD_m (squares), and $ESD_{90\%}$ (diamond) as a function of the laser pulse fluence, *F*. The dash-dot lines indicate the average value of the parameter, while the gray stripes show regions with a thickness equal to 2× the standard deviation of the parameter centered at its average value. Within the limits of the available statistics, the data suggest a negligible effect of the laser fluence on the NPs size characteristics, in the investigated fluence range. The upper axis reports the F/F_{th} (ϕ) scale that helps comparing the experimental results with theoretical outcomes obtained in section 5.4.

Finally, we also analyzed the variation of the NPs size with the temporal duration of the ultrashort ablation pulse. To this end, depositions were carried out for three different values of the pulse length τ_p (<1 ps), at a fixed laser fluence of 9.6 J/cm^2. The results are summarized in Table 5.1, and indicate a negligible effect on the NPs size properties by a change of the ultrashort laser pulse duration τ_p by a factor ≈10.

τ_p (fs)	<*ESD*> (nm)	<ESD_m> (nm)	<$ESD_{90\%}$> (nm)
50	13.1	5.2	30.0
280	13.7	4.2	37.6
580	13.9	6.6	35.0

Table 5.1: NPs size characteristics <*ESD*>, <ESD_m> and <$ESD_{90\%}$> for three different pulse duration τ_p at a fluence *F* = 9.6 J/cm^2.

5.4 MD-TTM Theoretical Model

MD-TTM is a computational scheme suitable for describing the evolution of a metallic target, such as copper, following irradiation by an intense, ultrashort laser pulse [23, 24]. In this approach, the MD part is responsible for handling the forces among the atoms at all times during the simulations. The TTM part, on the other hand, uses the coupling of electrons and phonons in order to calculate the transfer and diffusion of the energy to the lattice, during and after irradiation. These two methods, combined, allow for a strict and well-defined description of the laser ablation problem. In particular, MD simulations coupled to thermodynamic trajectory analysis allow one to follow the target decomposition history through both visual inspection of the simulated cell and material state evolution in the phase diagram.

The interactions between the atoms are described in terms of EAM potentials by Mishin *et al.* [25], as it accurately represents non-equilibrium configurations that are expected to develop in the ultrafast laser ablation of copper. The simulated copper target has dimensions $9 \times 9 \times 400$ nm^3 along the x, y, and z directions, respectively, where z is the direction of incidence of the laser pulse. The initial configuration is a fcc lattice with lattice constant 3.6316 Å, and a consequent total number of atoms of $\approx 2.5 \times 10^6$. This particular sample is thick enough along the z-direction to allow a proper description of the physics of the system while, at the same time, being computationally cost-effective. Both the top and bottom surfaces of the target are treated as open, i.e., are unconstrained, while periodic boundary conditions are imposed along the x and y directions. The initial configuration was relaxed for 50 ps at 300 K. The time step for the classical Verlet algorithm employed in the MD simulations was 2.5 fs, which we find ensures proper conservation of energy. During every MD time step, there were 150 iterations of the TTM scheme. The copper parameters used in the TTM part of the simulation code are summarized in Table 5.2.

Fermi energy	7.00 eV
Penetration depth[a]	13.00nm
Equilibrium density	8.49 atoms m^{-3}
Volumetric heat capacity	3.45 J m^{-3} K^{-1}
Electron heat capacity[b]	71.0 J m^{-3} K^{-2}

[a]Ref. 26; [b]Ref. 27

Table 5.2: Parameters for copper used in the TTM.

As will be seen below, we determine the various mechanisms occurring during the relaxation of the irradiated material in terms of the thermodynamic trajectories in the phase diagram. Therefore,

we first computed the phase diagram and the critical point of copper. For this purpose, we used the Gibbs ensemble method in order to calculate the binodal line and the isobaric isothermal ensemble for the spinodal line [28, 29]. The binodal line represents the line of separation between stable and metastable phase states e.g liquid and superheated liquid. The spinodal line represents the unstable region where two phases can co-exist. These are reported in Fig. 5.5 in temperature-density space. The data points both in the binodal and the spinodal curves are connected through splines.

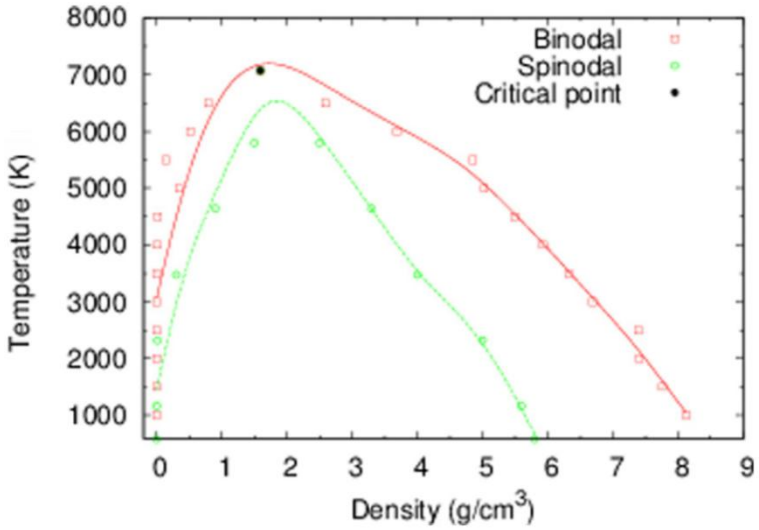

Figure 5.5: Calculated phase diagram of copper as described by the Mishin et al potential [25]. The red squares are the binodal points, and the green circles are the spinodal ones. The black square is the critical point, which is reported in Table 5.3. The lines connecting the data-points were extracted using the spline method.

Parameters	This work	Experimental values
T_c (K)	7070 ± 180	7696[a]
		5140 ≤ T_c ≤ 5580[b]
		8900[c]
ρ_c (g/cm^3)	1.59 ± 0.19	1.93[a]
		1.04[c]
P_c (bar)	12733 ± 130	5829[a]
		4200 ≤ Pc ≤ 6000[b]
ΔH_{vap} (kJ/mol)	313 ± 44	300.4[d]
T_b (K)	2545 ± 380	2835[d]

[a]Ref. 30; [b]Ref. 31
[c]Ref. 32; [d]Ref. 33

Table 5.3: Critical and thermodynamic properties of copper from the Mishin *et al.* potential compared with experimental values reported in the literature.

Our estimates for the critical properties of copper are reported in Table 5.3, along with experimental values. We also calculated two other physical properties of copper, namely the heat of vaporization, ΔH_{vap}, and the boiling temperature, T_b, also reported in Table 5.3. It is evident that the

estimated values of ΔH_{vap} and T_b are consistent with the ones found in the literature. In the following, the phase diagram will be used to illustrate the thermodynamic paths of the phase change processes following laser irradiation.

5.4.1 Simulation Results

The MD-TTM simulations use a laser pulse duration of 50 fs at a wavelength of 800 nm, as in the experiments described in sections 5.2 and 5.3. Simulations use the absorbed fluence, F_{abs}, rather than the total incident laser fluence, F. The MD-TTM simulations were carried out at low values of F_{abs} ranging from 0.05 J/cm^2 to 0.6 J/cm^2, and an absorbed fluence threshold $F_{abs,th}$ = 0.044 J/cm^2 was estimated. For the sake of comparison of experimental results and model predictions, in the following we will rationalize our findings in terms of a dimensionless parameter ϕ, obtained by normalizing the fluence to its threshold value, i.e., $\phi = F/F_{th}$ for the experimental results and $\phi = F_{abs}/F_{abs,th}$ for the theoretical predictions. The experimental analysis was carried out for $1 < F < 10$ J/cm^2 and, therefore, ϕ ranges from ≈3 to ≈23. On the other hand, in the MD-TTM simulations 0.05 J/cm^2 < F_{abs} < 0.6 J/cm^2, so that $1.13 < \phi < 13.63$. By considering the experimental absorption A ≈ 0.05 measured after irradiation of a copper foil with ≈130 fs, 800 nm Ti:Sa pulses [34], we can approximately estimate that the incident laser fluence used in the simulations varies from ≈1 to ≈14 J/cm^2. These values are consistent with the experimentally investigated fluence range, so the following analysis gives the theoretical investigations of the experiments performed in section 5.2 and 5.3.

Fig. 5.6(a) illustrates the reaction of the metal target to the sudden deposition of laser energy for F_{abs} = 0.2 J/cm^2; this fluence corresponds to experimental value of ϕ = 5.1, i.e., the same as that reported in the upper panel of Fig. 5.1. The three-dimensional (3D) snapshots represent what happens in the region close to the initial surface of the Cu target. The size of the target in the z direction is 400 nm, and only the top ~65 nm are depicted in figure 5.6(a). The particles are colored according to their potential energy U (in eV). After approximately 240 ps, almost 14% of the initial target has ablated, and the new surface of the target is found ~55 nm below its initial point. The plume evolution in both space and time can be tracked by means of a density map, as displayed in Fig. 5.6(b), in which the matter is colored according to its relative density (i.e., the density is normalized to the copper solid density value of 8.92 g/cm^3). The plume breaks up in clusters of various sizes, which move through regions of very low density, mainly vaporized material. Fig. 5.6(a) provides a macroscopic overview of the effects of ablation, but does not directly account for

the underlying physical mechanisms leading to ablation. These can be determined and interpreted by means of thermodynamic trajectories [5, 35-37], which allow the phase transformations that matter undergoes during each step of the ablation process to be followed. To this effect, the target is cut in "slices" of thickness 0.5 nm, inside which the average density and temperature is estimated. For F_{abs} = 0.2 J/cm^2 (ϕ = 5.1), the ablation depth after 240 ps is approximately 55 nm, as noted above. This portion of the target where ablation occurs is the region where the synthesis of NPs is initiated. By investigating the behavior of matter within this region, therefore, it is possible to monitor the NPs creation mechanisms and predict their evolution.

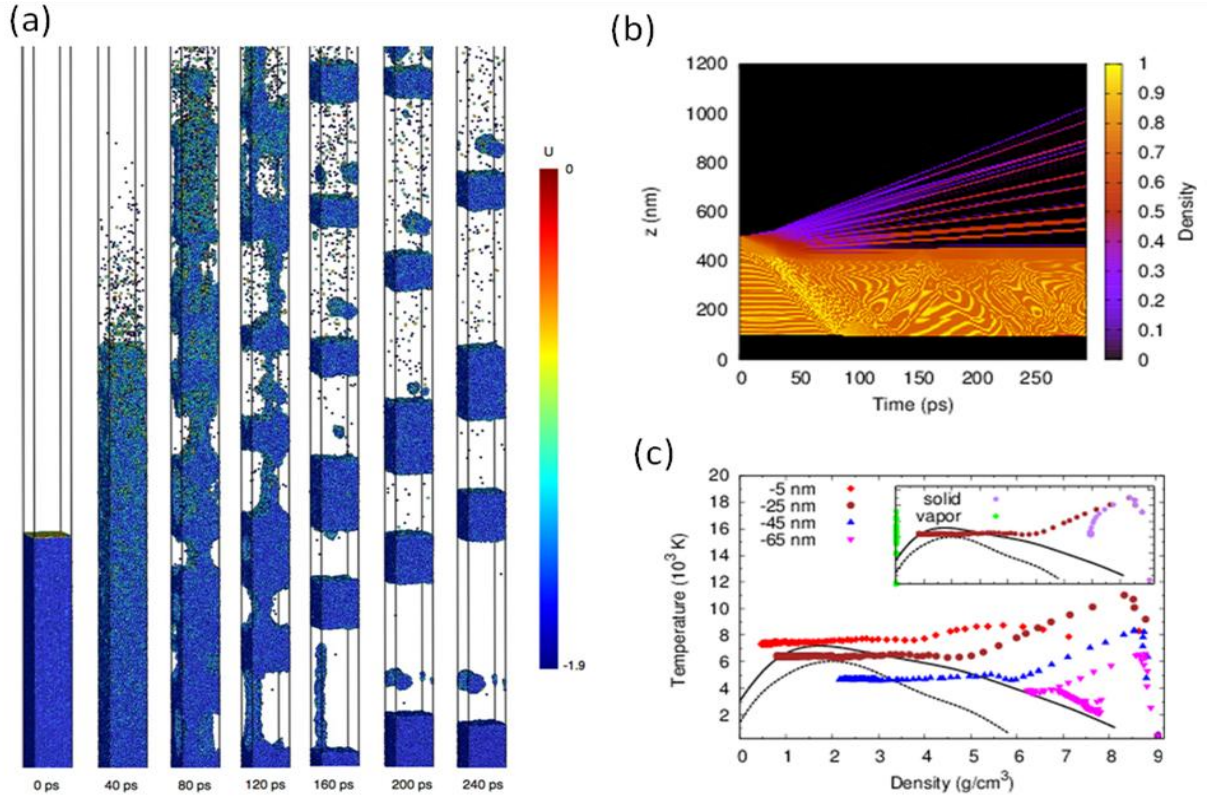

Figure 5.6: (a) 3D snapshots of the Cu target close to its original surface (the top 65 nm only are shown) at F_{abs} = 0.2 J/cm^2 (ϕ = 5.1), at different time delays after the laser pulse. The particles are colored according to their potential energy U (eV). (b) Evolution of the density of the target for F_{abs} = 0.2 J/cm^2 (ϕ = 5.1). Matter is colored according to relative density, i.e., the density normalized to copper solid density of 8.92 g/cm^3. (c) Thermodynamic trajectories of "slices" of the target for selected depths below the initial surface: –5 nm (red), –25 nm (brown), –45 nm (blue), and –65 nm (magenta). The fluence is F_{abs} = 0.2 J/cm^2 (ϕ = 5.1). The trajectories are projected on top of the phase diagram (binodal: continuous line, spinodal: dashed line). The inset illustrates the vapor and solid branches of the thermodynamic trajectory for depth equal to –25 nm.

The thermodynamic trajectories for slices typical of various zones of the ablated region are depicted in Fig. 5.6(c), at (i) –5 nm, (ii) –25 nm, and (iii) –45 nm, respectively; we also show one slice near, but below, the ablated zone, at (iv) –65 nm. The thermodynamic trajectories are projected

on top of the Cu phase diagram of Fig. 5.5. Immediately after the irradiation, each slice is heated to a very high temperature, at constant density (isochoric). The trajectory for –5 nm evolves towards very low densities, without crossing the binodal line, a behavior which is characteristic of vaporization. For –25 nm, the trajectory approaches the binodal from the supercritical region, breaking into two distinct branches (vapor and solid), typical of fragmentation [5, 35]. This behavior is explicitly presented in the inset of Fig. 5.6(c). The main characteristic of this mechanism is the disintegration into clusters, which are the building elements of the solid branch and which are embedded in vapor regions. As it is obvious in the inset of Fig. 5.6(c), for a depth of –25 nm, the disintegration takes place during the expansion phase before reaching the liquid-vapor coexistence region of the phase diagram. At –45 nm, the material enters the metastable region of the phase diagram, where the breakup of the vapor and solid branches takes place. Thus, phase separation occurs and homogeneous regions are formed. Finally, for –65 nm, i.e., below the ablation depth, matter is not ablated and quickly relaxes back to its initial state.

Depending on the fluence, some of these mechanisms may be suppressed, and others may develop (e.g., spallation). But, apart from the mechanisms, it is interesting to investigate the effect of the fluence on the characteristics of the plume, such as the average velocity, V_{av}, of the ejected particles. In Fig. 5.7(a), V_{av} is shown as a function of F_{abs}. The average velocity increases rapidly with fluence, then reaches a plateau for $F_{abs} > 0.25$ J/cm^2 ($\phi > 5$). This indicates that F_{abs} in this range has only a minor influence on V_{av}, and this is qualitatively similar to the experimental observation (see Fig. 5.2(b)). As a side note, not taking into account the velocities of the monomers does not significantly alter the results; rather, it simply reduces the numerical values of V_{av}, but the general trend remains the same as Fig. 5.7(a) shows.

In order to compare accurately the theoretical results with the experimental measurements, it is essential to extract the relative and cumulative distributions of the NPs *ESDs*. The results are shown in Fig. 5.7(b) for $F_{abs} = 0.3$ J/cm^2 ($\phi = 6.7$). This is the final distribution of the particles *ESDs* after approximately 300 ps, without taking into account the monomers. It is clear from the cumulative distribution that most NPs in the plume are small ($ESD < 1$ nm). In fact, 90% of the clusters have a size smaller than $ESD_{90\%} \approx 0.57$ nm. The average size value is $\langle ESD \rangle \approx 0.98$ nm, and the median is $ESD_m = 0.41$ nm. Both the $ESD_{90\%}$ and ESD_m have been calculated using the same methodology as in experiment. As anticipated, for the sake of comparison, we consider the normalized size parameter d_n. From Fig. 5.7(b), one finds that the ESD histogram predicted by MD-TTM is

asymmetric, consistent with the experimental observations (see Fig. 5.3). Almost 90% of the NPs *ESDs* are counted for the normalized parameter $d_n \leq 1.5$, as can be seen from the cumulative function in Fig. 5.7(b). In the inset of Fig. 5.7(b), the whole range of the cumulative function is displayed. Since 90% of the *ESDs* have values smaller than $ESD_{90\%} \approx 0.57$ nm, the remaining 10% is spread over a wide interval with very few large clusters reaching values as high as 12 nm ($d_n \approx 30$).

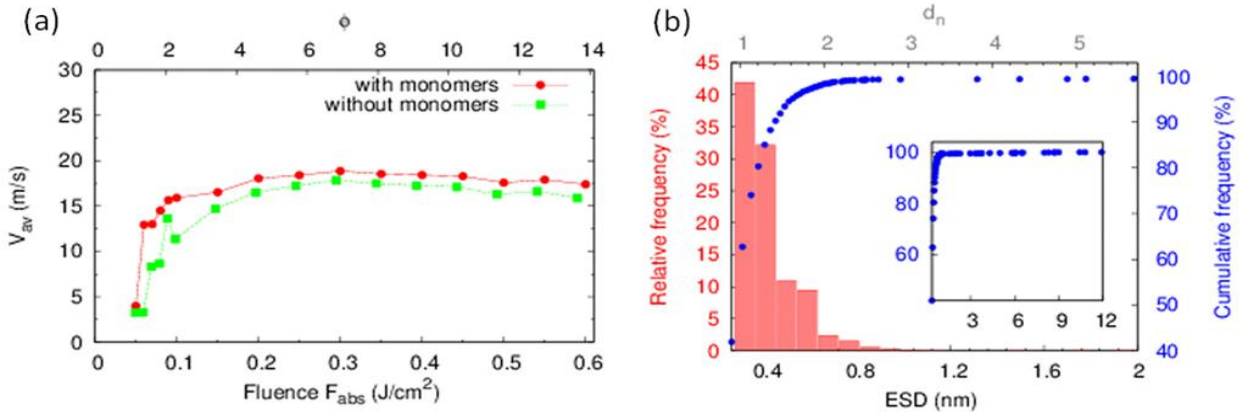

Figure 5.7: (a) Average velocity, V_{av}, of the NPs as a function of the absorbed fluence, F_{abs}. Results are presented including (red circles) and excluding (green squares) monomers. The upper axis reports corresponding values of ϕ, for comparison purposes with the experimental results. (b) Size histogram (left axis) and cumulative distribution (right axis) of the NPs *ESD* at $F_{abs} = 0.3$ J/cm^2 ($\phi_{theo} = 6.72$). The top axis reports d_n, the NPs *ESD* normalized to its median size ESD_m. The inset presents the cumulative distribution for the whole range of *ESDs*.

It is interesting to further investigate the nature and composition of the ablated material in the case of $F_{abs} = 0.3$ J/cm^2 ($\phi \approx 6.7$) after 300 ps. In Fig. 5.8(a), two stacked bars are presented. The left bar illustrates the fraction of the ablated material that belongs to clusters of various sizes. It is evident that the target decomposes overwhelmingly (≈80%—yellow color) into large clusters. On the other hand, monomers account for just a tiny fraction (≈1.5%—red color) of the total ablated material. This is consistent with previous reports that the NP component is prominent in the material blow-off resulting from ultrashort laser ablation of a metallic target [9, 10, 38-40]. Apparently, mechanisms such as fragmentation and spallation drive the ablation process for $F_{abs} = 0.3$ J/cm^2 ($\phi = 6.7$). The right bar of Fig. 5.8 (a) reports the number of elements counted in each class of clusters. Of course, monomers are the dominant fraction of the structures observed after the ablation threshold (≈55%—red color in right bar of Fig. 5.8(a)), due to their very small size and mass. The largest clusters, with more than 10001 particles are less than 1% of the total number of ablated particles. The large proportion of monomers in the cluster distribution and their insignificant contribution to the ablated material (left bar) are the reasons we did not take them into account in

the calculation of the histogram of Fig. 5.7(b). By excluding the monomers, clusters with 2 to 10 particles are the most numerous in the ablated material, while very large clusters are minor. These model predictions are consistent with the characteristic properties of the NPs size distribution observed experimentally.

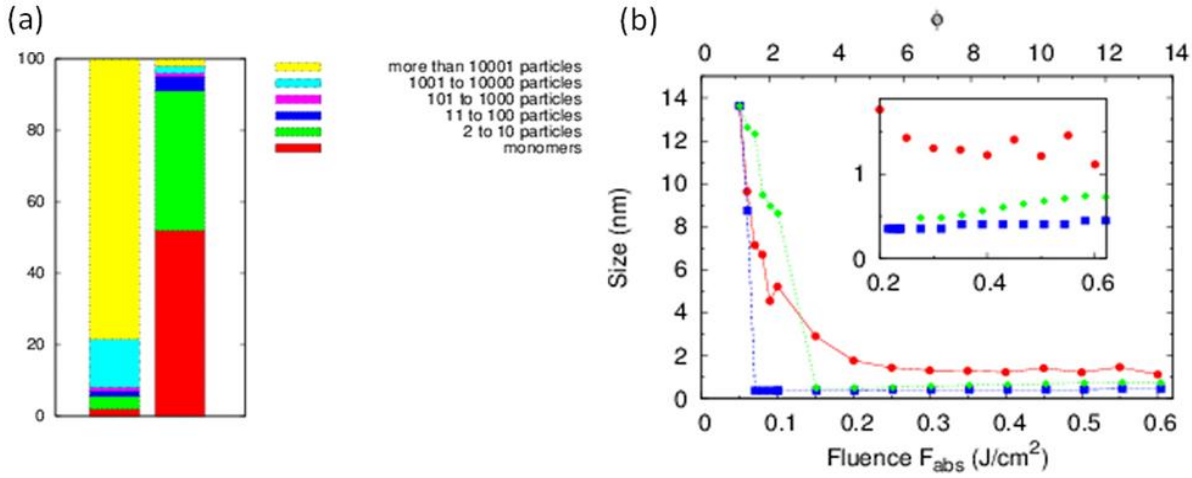

Figure 5.8: (a) Distribution of the ablated material among clusters for F_{abs} = 0.3 J/cm^2 (ϕ = 6.7). Several cases of cluster sizes are examined. It reveals that clusters with more than 10001 particles (yellow color) possess the largest fraction of the ablated material. Distribution of clusters for F_{abs} = 0.3 J/cm^2 ϕ = 6.7). By excluding the monomers, clusters with 2 to 10 particles are the most numerous in the ablated material. (b) <*ESD*> (circle), ESD_m (squares), and $ESD_{90\%}$ (diamond) as a function of the absorbed fluence, F_{abs}. The upper axis reports corresponding values of ϕ, for comparison purposes with the experimental results.

Finally, in Fig. 5.8(b), the sizes <*ESD*>, ESD_m, and $ESD_{90\%}$ are presented as a function of F_{abs}. For high fluences (F_{abs} > 0.25 J/cm^2 or ϕ > 5), the sizes $ESD_{90\%}$ and ESD_m converge and reach a plateau. The <*ESD*> values are higher because of the effect of the very large clusters. It is clear that high fluences have a negligible effect on the sizes of the NPs, a prediction verified by the experimental results. Finally, these findings rationalize the role of such an important experimental parameter as laser fluence on the final properties of the produced NPs, which can eventually help the search for possible strategies aiming to control/tailor size distributions of NPs produced by ultrashort laser ablation [15, 41-46]. Indeed, the general agreement between MD-TTM predictions and experimental findings addressed here suggests that modeling can effectively support outlining the more appropriate experimental approaches.

5.5 Applications of Deposited Nanoparticle Films

Nanoparticle research is currently an area of intense scientific interest due to a wide variety of potential applications in physics, chemistry, biology, material science, and it impacts other disciplines as well [1, 2]. From our previous set of experiments on NPs imaging, deposition, and characterization, it is clear that ULA is a powerful technique to produce NPs embedded films. We discuss here two applications of NPs generation and deposition, carried out with a femtosecond laser system (527 nm, 300 fs, Nd:Glass): (i) gold nanoparticles on a quartz-crystal microbalance (QCM) electrode for biosensor applications; (ii) titanium dioxide (TiO_2) nanoparticles on a photoanode for hydrogen evolving photoelectrochemical cell (PEC) applications. The experimental setup used for NPs deposition is similar to the one mentioned in section 3.3. A brief explanation of these two applications is given in the following sections.

5.5.1 QCM based biosensors

We used gold NPs to improve the sensitivity of biosensors based on a quartz-crystal microbalance (QCM) device [47]. The NPs produced by irradiating a gold target with 527-nm, 300-fs laser pulses, in high vacuum, are directly deposited on the QCM electrode. It has been recently reported that sensor sensitivity can increase by enhancing the effective surface of the QCM electrode where the bio-receptor is anchored and the analyte is caught by using NPs. This was achieved by means of a chemical approach based on precipitation of 50-nm gold nanoparticles onto the QCM gold lamina [48]. Here we take the physical alternative offered by ULA to improve the sensitivity of a QCM biosensor.

The electrode surface is nanostructured through deposition of gold NPs, and different samples are fabricated by varying the deposition time, t_{dep}, in the 10-40 minutes range. The different deposition times modify the QCMs surface, thus yielding sensors whose surface changes from a quasi-dispersed coverage of NPs to a NPs-assembled film deposited on the standard QCM gold lamina [49]. This, in turn, permits a direct testing of how the physical modification induced on the QCM lamina influences the effectiveness of antibody attachment. The experimental procedure consists of a flow of standard concentration of antibodies Anti-IgG from goat (50 μg/mL) onto NP-modified QCM electrodes to check the potential increase of the frequency shift when the antibodies interact with the nanostructured electrode surface. Then the flow of the solution containing the analyte (IgG from mouse), recognized by anti-IgG linked onto NP-modified QCM, determines the

improvement in sensitivity of the device, due to larger number of antibodies deposited onto the gold lamina, as compared to the standard case.

Figure 5.9 shows how increasing t_{dep} changes the basal frequency of the electrodes; a linear decrease of the frequency indicates a linear increase of NPs mass, Δm, deposited onto the lamina by fs-LA [50]. From Δm, we have estimated the equivalent thickness, h_{eq}, of the NPs gold layer deposited on the QCM lamina, as reported in Fig. 5.9. We observe that the values of t_{dep} exploited correspond to an equivalent thickness h_{eq} varying from few nm, at low deposition time, up to ≈25 nm, for the longer deposition time. Since the average height of the gold NPs is of the order of ≈5 nm, the morphology of the QCM surface consequently changes from a quasi-dispersed coverage of NPs to a NPs-assembled complete film for the range of deposition times exploited here.

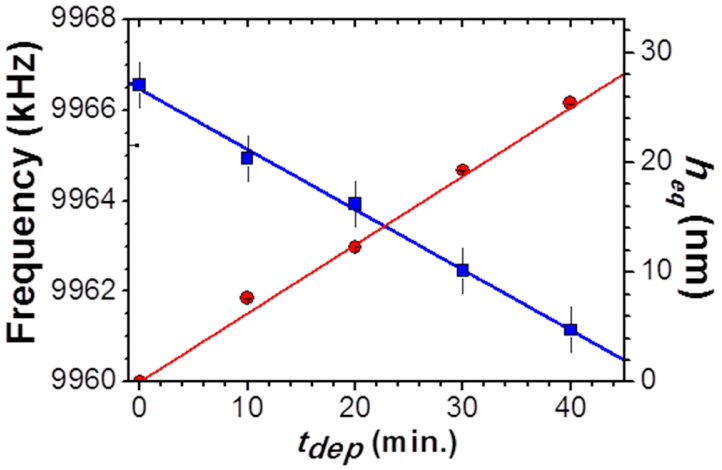

Figure 5.9: Frequency of the NP-modified QCMs (squares, left vertical axis) decorated with different amount of NPs produced by fs-LA. The horizontal axis reports the deposition time t_{dep}. The circles show the corresponding equivalent thickness, h_{eq}, of the deposited gold NPs (right vertical axis).

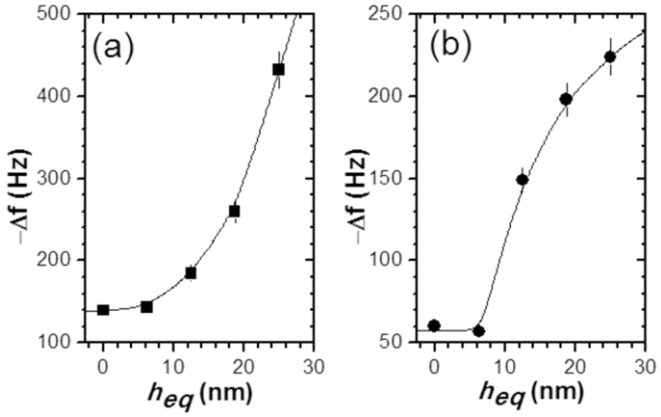

Figure 5.10: Frequency shift Δf measured for the different nanoparticle modified QCM electrodes obtained by deposition of NPs layers with different equivalent thickness h_{eq}. Panel (a) refers to the electrode functionalization with Anti-IgG from goat, while panel (b) corresponds to the recognition antigen IgG from mouse. The solid lines are guides to the eye.

Fig. 5.10(a) reports the frequency variation occurring when the Anti IgG from goat flows in the QCM device. We clearly observe that the modification induced to the QCM lamina effectively influences the amount of Anti IgG tethered to the electrode surface. In particular, for h_{eq}<7 nm the frequency shift is negligible, in agreement with the fact that the NPs are dispersed on the lamina surface. As h_{eq} increases above ≈7 nm, the NPs coverage progressively improves the available gold surface for IgG attachment, and a three-fold increase of the frequency shift, Δf, is achieved at h_{eq} ≈ 25 nm, with respect to the value obtained by a standard QCM electrode. Subsequently, the IgG antigen recognition is analyzed, and the resulting frequency shift is shown in Fig. 5.10(b). As expected, the improved amount of AntiIgG results into a corresponding enhancement of the Δf values registered by Nm-QCM for h_{eq}>7 nm. Interestingly, the frequency shift at h_{eq} ≈ 25 nm is increased by about 4 times, compared to the standard QCM electrode. This, in turn, demonstrated that the nanoparticle modified QCM can be a suitable route to improve the sensitivity of QCM-based biosensors.

5.5.2 PEC Performance of TiO_2 Nanoparticles

We investigated the effects of deposition conditions on crystalline phase, morphology and photoelectrochemical properties of a TiO_2 NPs-assembled films electrode [51]. For this, we deposited TiO_2 nanoparticles on Ti foil via ULA (527 nm, 300 fs, Nd:Glass), at room temperature. We produced five set of TiO_2 NPs assembled films by varying deposition time and chamber pressure from high vacuum (≈10^{-6} mbar) to various oxygen pressures (namely, 0.1 mbar and 1 mbar). The deposition setup is same as in section 3.6 and the details of deposited films are given in table 5.4. All of the deposited TiO_2 NPs films were annealed in air at 500º C for 30 min. Then, the annealed TiO_2 NPs films were encapsulated as photoelectrode by using conductive silver adhesives and epoxy resin. The effective exposed area of the photoelectrode are listed in Table 5.4.

Samples	Chamber pressure (mbar)	Deposition time (h)	Area (cm^2)
TiO_2-Low-3	0.1	3	0.08
TiO_2-High-3	1	3	0.18
TiO_2-Vac-3	10^{-6}	3	0.12
TiO_2-Vac-1.5	10^{-6}	1.5	0.23
TiO_2-Low-1.5	0.1	1.5	0.23

Table 5.4: The deposition condition of TiO_2 NPs films produced by ULA

Since the crystalline phase and morphology of TiO_2 films photoelectrodes are crucial to their photoelectrochemical properties, we determined the crystal structures of TiO_2 NPs film electrodes by using an X-ray diffractometer, and the surface composition of TiO_2 NPs film electrodes were investigated by X-ray photoelectron spectroscopy. The morphology of the TiO_2 NPs-assembled films was analyzed by a field emission scanning electron microscope and an atomic force microscopy. Table 5.5 summarizes crystalline phase and photoelectrochemical properties of TiO_2 NPs films deposited by ULA.

Samples Properties	TiO_2 Low-3	TiO_2 High-3	TiO_2 Vac-3	TiO_2 Vac-1.5	TiO_2 Low-1.5
Crystallite size (nm)	15.9	14.7	12.0	8.7	9.2
Crystalline phase[a]	R	R	R and A	R and A	R
Photocurrent (mA/cm^2)	0.11	0.19	0.13	0.08	0.21
Photovoltage (V)	0.48	0.72	0.78	0.71	0.45
Electron lifetime (s)	-	14.4	14.8	-	8.4
Carrier density (cm^{-3})	9.8×10^{23}	2.7×10^{22}	7.3×10^{22}	2.7×10^{21}	5.6×10^{23}

[a] R: rutile; A: anatase.

Table 5.5: Crystalline phase and photoelectrochemical properties of TiO_2 NPs films deposited by ULA.

When the energy of photons is equal or larger than the semiconductor band gap, photoelectron-hole pairs can be generated in the electrode surface. The separated photoelectron hole pairs can spread to the solution/electrode interface and form an electric double layer, which results in an open circuit voltage. Simultaneously, a photocurrent can be produced when photogenerated electrons are transferred over the external circuit. The photo-induced current signal reflects the conductance of the semiconductor thin film, indicating the amount of charge carrier of the semiconductor. For overall photoelectrochemical water splitting similar to electrolysis, water molecules are reduced by electrons to form H_2 and are oxidized by holes to form O_2. Thus, the photocurrent determines the photoelectric converting efficiency and the hydrogen evolving property of PEC.

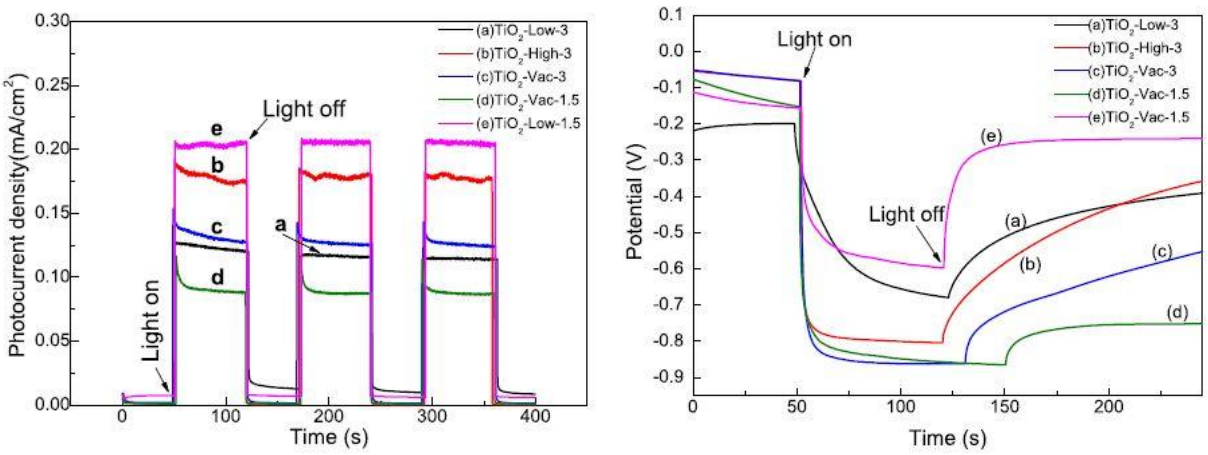

Figure 5.11: (Left) Photocurrent density-time curves (I-t) obtained from fs-PLD deposited TiO_2 NPs films in 1 M KOH at 0 V Ag/AgCl under interrupted illumination with a solar simulator (with AM 1.5 filter, 100 mW/cm^2). (Right) Open potential transient curves in the same condition.

Fig. 5.11 shows the photocurrent density-time curves of TiO_2 NPs film electrodes produced by fs-PLD. For TiO_2-Vac-3 and TiO_2-Vac-1.5, deposited under vacuum, the photocurrent density of TiO_2-Vac-3 was 0.05 mA/cm^2 higher than that of TiO_2-Vac-1.5, which can be ascribed to the longer deposition time of 3 h. With increase of deposition time, more TiO_2 NPs can be collected on the substrate, and more photoactive sites can be created. For TiO_2-Low-3 and TiO_2-High-3 with the same deposition time of 3 h, it can be observed that the photocurrent density of TiO_2-High-3 deposited in the chamber pressure of 1 mbar was higher than that of TiO_2-Low-3 which was deposited in the pressure of 0.1 mbar. In higher oxygen pressure, the proper defect structures can be obtained, resulting in better charges separation and higher photoelectrochemical properties. In our work, it is demonstrated that TiO_2 NPs film with pure rutile phase can exhibit better photoelectrochemical activities than that with mixed phase. Among all samples, TiO_2-Low-1.5 and TiO_2- High-3 exhibited the comparatively higher photo-induced current density. They have the same rutile phase, so the difference of their photocurrent may be related to their morphology. Compared to that of TiO_2 NPs deposited under vacuum or in 0.1 mbar, the morphology of the sample (TiO_2-High-3) obtained in 1 mbar shows the sparser nanoagglomerates. Fig. 5.11, shows the longer time required for the photovoltage value of TiO_2-High-3 and TiO_2-Vac-3 to get back to the original value because the lifetime of the photogenerated holes and electrons on the surface of the electrodes lived much longer. Moreover, the higher photovoltage gives rise to the larger charge separation rate. Therefore, combined with photovoltage, it can be concluded that the deposition condition of TiO_2-High-3 with higher chamber pressure and longer deposition time represents the

optimal condition for better PEC performance of TiO_2 NPs films produced by fs-PLD. Thus, the efficient TiO_2 NPs film for hydrogen production from water splitting can be assembled by adjusting the deposition conditions when using fs-PLD method.

References

[1] *Laser Ablation and Its Applications*, edited by C. Phipps (Springer, Berlin, 2007).

[2] *Pulsed Laser Deposition of Thin Films*, Edited by Robert Eason (Wiley, New Jersey, 2007).

[3] S. Amoruso, G. Ausanio, R. Bruzzese, M. Vitiello, and X. Wang, Phys. Rev. B 71, 033406 (2005).

[4] S. Eliezer, N. Eliaz, E. Grossman, D. Fisher, I. Gouzman, Z. Henis, S. Pecker, Y. Horovitz, M. Fraenkel, S. Maman, and Y. Lereah, Phys. Rev. B 69, 144119 (2004).

[5] D. Perez and L. J. Lewis, Phys. Rev. B 67, 184102 (2003).

[6] T. E. Glover, G. D. Ackerman, R. W. Lee, H. A. Padmore, and D. A. Young, Chem. Phys. 299, 171 (2004).

[7] S. Amoruso, R. Bruzzese, X. Wang, N. N. Nedialkov, and P. A. Atanasov, Nanotechnology 18, 145612 (2007).

[8] S. Noel, J. Hermann, and T. Itina, Appl. Surf. Sci. 253, 6310 (2007).

[9] M. E. Povarnitsyn, T. E. Itina, M. Sentis, K. V. Khishchenko, and P. R. Levashov, Phys. Rev. B 75, 235414 (2007).

[10] S Amoruso, R Bruzzese, X Wang, N N Nedialkov and P A Atanasov, J. Phys. D: Appl. Phys. 40, 331 (2007).

[11] D. Bauerle, *Laser Processing and Chemistry*, 4th ed. (Springer, Berlin, 2011).

[12] *Laser Precision Microfabrication*, edited by K. Sugioka, M. Meunier, and A. Pique (Springer, Berlin, 2010).

[13] T. E. Glover, J. Opt. Soc. Am. B 20, 125 (2003).

[14] S. Amoruso, R. Bruzzese, C. Pagano, and X. Wang, Appl. Phys. A 89,1017 (2007).

[15] S. Amoruso, N. N. Nedyalkov, X. Wang, G. Ausanio, R. Bruzzese, and P. A. Atanasov, J. Appl. Phys. 110, 124303 (2011).

[16] L. V. Zhigilei, Z. Lin, and D. S. Ivanov, J. Phys. Chem. C 113, 11892 (2009).

[17] N.N. Nedialkov, P.A. Atanasov, S. Amoruso, R. Bruzzese, X. Wang, Appl. Surf. Sci. 253, 7761 (2007).

[18] K. Furusawa, K. Takahashi, H. Kumagai, K. Midorikawa, M. Obara, Appl. Phys. A 69, S359 (1999).

[19] B. Verhoff, S.S. Harilal, J.R. Freeman, P.K. Diwakar, A. Hassanein, J. Appl. Phys. 112, 093303 (2012).

[20] S. Amoruso, R. Bruzzese, N. Spinelli, R. Velotta, M. Vitiello, X. Wang, Europhys. Lett. 67, 404 (2004).

[21] V. Iannotti, S.Amoruso, G. Ausanio, X. Wang, L. Lanotte, A. C. Barone, G. Margaris, K. N. Trohidou, and D. Fiorani, Phys. Rev. B 83, 214422 (2011).

[22] M. Sanz, M. Lopez-Arias, J. F. Marco, R. de Nalda, S. Amoruso, G. Ausanio, S. Lettieri, R. Bruzzese, X. Wang, and M. Castillejo, J. Phys. Chem. C 115, 3203 (2011).
[23] M. Gill-Comeau and L. J. Lewis, Phys. Rev. B 84, 224110 (2011).
[24] D. S. Ivanov and L. V. Zhigilei, Phys. Rev. B 68, 064114 (2003).
[25] Y. Mishin, M. J. Mehl, D. A. Papaconstantopoulos, A. F. Voter, and J. D. Kress, Phys. Rev. B 63, 224106 (2001).
[26] J. Byskov-Nielsen, "Short-pulse laser ablation of metals," Ph.D. thesis (Aarhus University, 2010).
[27] Z. Lin, L. V. Zhigilei, and V. Celli, Phys. Rev. B 77, 075133 (2008).
[28] D. V. Makhov and L. J. Lewis, Phys. Rev. B 67, 153202 (2003).
[29] N. Tsakiris and L. J. Lewis, Eur. Phys. J. B 86, 313 (2013).
[30] H. Hess, Z. Metallkd. 89, 388 (1998).
[31] ASM Specialty Handbook: Copper and Copper Alloys, edited by J. R. Davis (ASM International, 2001).
[32] J. A. Cahill and A. D. Krishenbaum, J. Phys. Chem. 66, 1080 (1962).
[33] M. M. Martynyuk and O. G. Panteleichuk, High Temp. 14, 1201 (1976).
[34] S. E. Kirkwood, A. C. Van Porta, Y. Y. Tsui, and R. Fedosejevs, Appl. Phys. A 81, 729 (2005).
[35] D. Perez and L. J. Lewis, Phys. Rev. Lett. 89, 255504 (2002).
[36] P. Lorazo, L. J. Lewis, and M. Meunier, Phy. Rev. Lett. 91, 225502 (2003).
[37] P. Lorazo, L. J. Lewis, and M. Meunier, Phys. Rev. B 73, 134108 (2006).
[38] G. O'Connell, T. Donnelly, and J. G. Lunney, "Nanoparticle plume dynamics in femtosecond laser ablation of gold," Appl. Phys. A (published online).
[39] S. Amoruso, R. Bruzzese, X. Wang, and J. Xia, Appl. Phys. Lett. 92, 041503 (2008).
[40] C. Wu and L. V. Zhigilei, Appl. Phys. A 114, 11 (2014).
[41] M. Guillermin, J. P. Colombier, S. Valette, E. Audouard, F. Garrelie, and R. Stoian, Phys. Rev. B 82, 035430 (2010).
[42] S. Amoruso, R. Bruzzese, X. Wang, G. Ausanio, and L. Lanotte, J. Phys. B 40, 1253 (2007).
[43] S. Amoruso, N. N. Nedyalkov, X. Wang, G. Ausanioa, R. Bruzzese, and P. A. Atanasov, Thin Solid Films 550, 190 (2014).
[44] R. Hergenroeder, M. Miclea, and V. Hommes, Nanotechnology 17, 4065 (2006).
[45] S. Amoruso, R. Bruzzese, and X. Wang, Appl. Phys. Lett. 95, 251501 (2009).
[46] E. G. Gamaly, A. V. Rode, O. Uteza, V. Kolev, B. Luther-Davies, T. Bauer, J. Koch, F. Korte, and B. N. Chichkov, J. Appl. Phys. 95, 2250 (2004).
[47] B. Della Ventura, L. Schiavo, C. Altucci, R. Esposito, R. Velotta, Biomedical optics express 2, 3223 (2009).
[48] A. Makaraviciute, T. Ruzgas, A. Ramanaviciuscd, A. Ramanaviciene, Anal. Methods 6, 2134 (2014).
[49] S. Amoruso, G. Ausanio, R. Bruzzese, L. Lanotte, P. Scardi, M. Vitiello, J. Phys.: Condens. Matter 18, L49 (2006).
[50] G. Z. Sauerbrey, Z. Phys. 155, 206 (1959).

[51] Lixia Sang, Hongjie Zhang, Xiaochang Ni, K.K. Anoop, Rosalba Fittipaldi, Xuan Wang, Salvatore Amoruso, International Journal of Hydrogen Energy 40, 785 (2015).

Chapter 6

Optical-Vortex Laser Ablation and Surface Micro-nanostructuring

6.1 Introduction

The orbital angular momentum (OAM) of light and generation of optical vortices (OVs) have been subject of intensive research since 1990's [1-3]. In general, angular momentum of light having circular polarization is named as spin angular momentum (SAM), while that associated with a spiral wavefront is called orbital angular momentum (OAM). That is, spin is associated with the rotation of electric or magnetic fields oscillating within the optical wave, meanwhile twist of the optical wavefront results in an OV, i.e. a beam with a point of zero intensity located at its center [1-3]. When a free material particle absorbs light having spin or twist, the particle itself undergoes a spin orientation, i.e. light exerts a rotational form of radiation pressure, showing that this kind of light carries angular momentum. Laser beams carrying OAM have been recently applied in various experiments, especially trapping for Bose-Einstein condensates, microstructure rotation in laser tweezers and spanners [4-7]. In particular, in optical tweezing OVs can trap and manipulate particles with less intensity than standard Gaussian beams, which results in less absorption or photodamage due to multiphoton process. In addition to possible technological applications in particle manipulation, optical sensing, and classical and quantum communication, OAM beams recently showed potential applications in laser ablation (i.e. optical-vortex laser ablation) and material processing [8-14].

This chapter reports on laser ablation of a solid target using fs optical vortex pulses. The experimental details of optical vortex laser ablation is illustrated in section 6.2. Section 6.3 demonstrates the femtosecond (fs) laser surface structuring of silicon (Si) using optical vortex beams generated by a *q*-plate (see section 3.4). Here, the variation of the produced surface structures is investigated as a function of the number of incident laser pulses, *N*, and laser polarization, ***P***, at laser fluence above the ablation threshold value. Direct fs laser ablation of copper (Cu) with an optical vortex beam is also presented in this section. Here, the variation of the produced surface structures is studied as a function of the number of pulses, *N*, with a fixed beam polarization ***P***. The concluding remarks of my experimental investigations are given in section 6.4.

6.2 Experimental Details

A schematic of the experimental setup is shown in figure 3.5. A regeneratively amplified Ti:Sa laser system (Coherent Legend), delivering linearly polarized ≈35 fs pulses at 800 nm central wavelength was used for irradiation of a single-crystalline (100) silicon target, in air. The beam spatial shaping is provided by a *q*-plate with a topological charge $q = +1/2$, producing an optical vortex beam carrying an orbital angular momentum (OAM) $l = \pm 1$, whose spatial intensity distribution, as acquired by a beam profiler, is shown in Fig. 3.5 [15]. The central part of this beam was selected by spatial filtering with an iris, resulting in the annular beam shape shown in Fig. 3.5. The *q*-plate axis was aligned perpendicular to the input beam polarization, thus producing an azimuthal distribution of the optical vortex beam polarization [16]. Other beam polarizations (like e.g. radial or spiral) can be obtained by using a *q*-plate axis with $q = 1/2$. The target, mounted on a translation stage, was located perpendicular to the laser beam direction and close to the focal plane of a lens (75 mm focal length). An electromechanical shutter provided the selection of the desired number of pulses, *N*, applied to the same spot on the target. The irradiated surface regions were inspected using an optical microscope and a Zeiss ΣIGMA field emission scanning electron microscope (FESEM) with a nominal resolution of 1.3 nm at 20 kV, as mentioned in section 3.4.

In the case of copper, the ablation process was carried out at laser energy $E_L \approx 90\ \mu$J, and the corresponding average fluence of the optical vortex beam was $F = 1.4$ J/cm^2. This value of *F* is three times the threshold fluence required for copper ablation with a Gaussian beam [17, 18]. We studied the role of number of laser pulses (*N)* in the surface structure formation, going from single to thousands of shots. All the experiments were performed with a fixed azimuthal laser polarization ***P***.

6.3 Laser Surface Structuring of Si and Cu targets using an Optical Vortex Beams

Fig. 6.1 shows SEM micrographs of the processed Si surface after irradiation with different values of *N*, at a laser energy $E_L \approx 85\ \mu$J. The SEM micrographs follow the laser beam properties with a non-ablated region at the centre of the processed surface. The inner part is almost unaffected by the ablation process, due to the central singular region of the beam with zero intensity, and has a radius $R_{in} \approx 7\ \mu$m. The external radius of the ablated area is $R_{ex} \approx 57\ \mu$m. A circularly shaped region of debris extending to $\approx 2 \times R_{ex}$ can be also observed in Fig. 6.1. This is due to the nanoparticles (NPs) produced during the ablation process that are backward deposited on the target [19, 20]. From

the measured radii, a spot area $S = \pi(R_{ex}^2 - R_{in}^2) \approx 1 \times 10^{-4}$ cm^2 can be estimated, indicating an average laser fluence $F = E_L/S \approx 0.8$ J/cm^2, intermediate between the single- (≈1 J/cm^2) and multi-pulse (≈0.4 J/cm^2) peak fluence thresholds for ablation typically observed for Gaussian-like beams [17, 21-23].

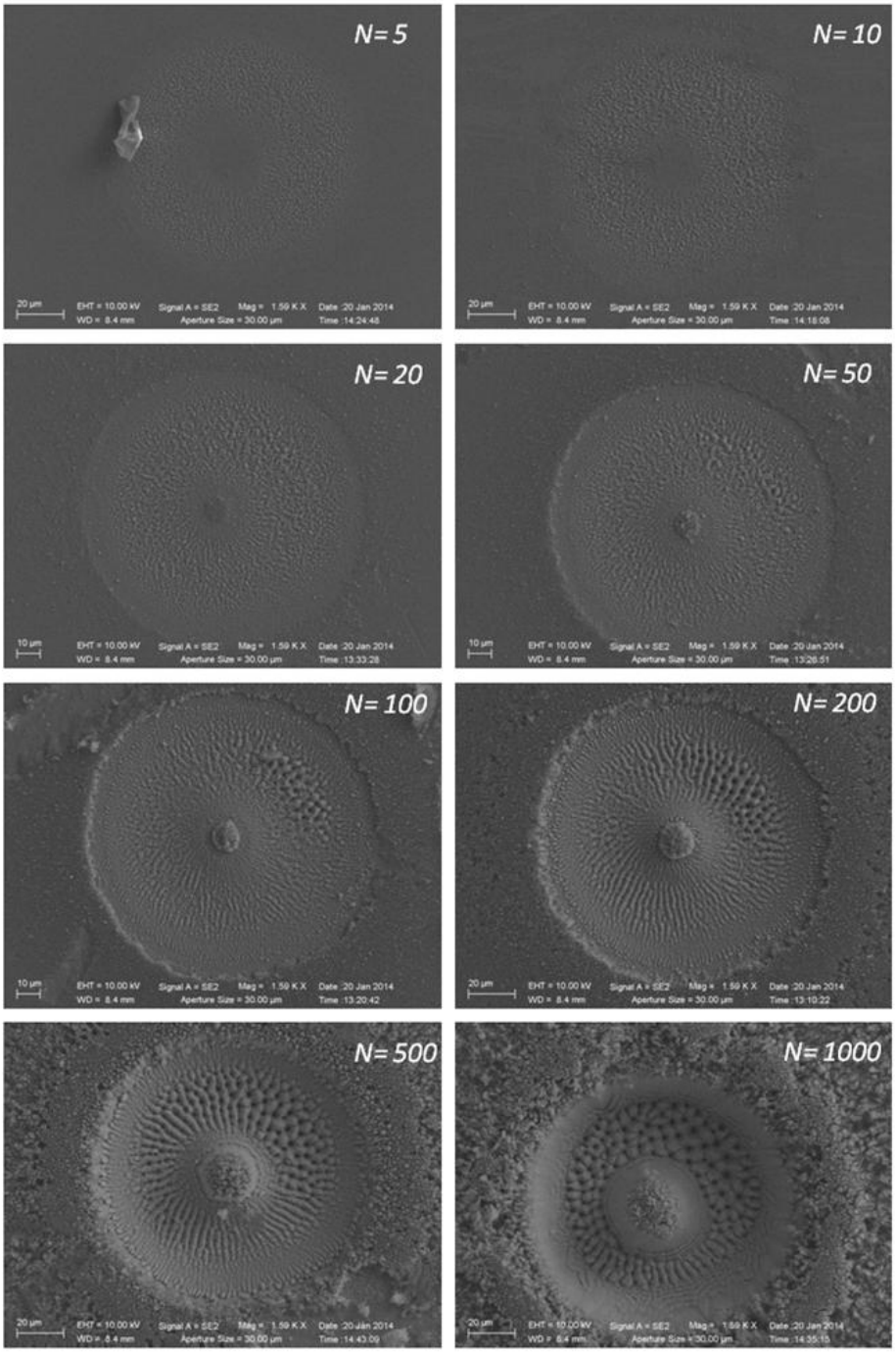

Figure 6.1: SEM micrographs of the processed Si surface after irradiation with N pulses, at a laser energy $E_L \approx 85\ \mu$J. The value of N and scale bar are marked on top-right and bottom left corners of each Image, respectively.

We carried out a detailed analysis of surface morphology dependence on pulse number, with $5 \leq N \leq 1000$. This allows evidencing the crucial role of the parameter N on the evolution of the surface structures. For the sake of discussion, we divide the investigated range of N in three different regimes: low ($5 \leq N \leq 50$), intermediate ($50 < N < 500$), and high ($500 \leq N \leq 1000$) number of pulses. Characteristic SEM images in these three regimes are reported in Fig. 6.1. At $N = 5$, we can identify three regions. The central, almost unaffected area with a radius $r \approx R_{in}$, decorated with NPs. An external area, for $r > 20$ μm, presenting a number of random structures, at the micro- and nano-scale, composed by pores, cavities, rims, and protrusions, and decorated with NPs whose characteristic size is similar to that observed in the central region. An intermediate, annular area, with a thickness of ≈ 10 μm, showing circular ripples with a period close to the laser wavelength, resembling low spatial frequency laser-induced periodic surface structures (LIPSSs) typically observed with Gaussian beams at low number of pulses [24, 25]. Increasing N ($N = 10$), these ring-like ripples disappear, similarly to what was recently reported by Jia *et al.*, who studied LIPSS dynamics in silicon and ascribed the ring-like structure to possible diffraction effects induced by optical elements [24]. At $N = 20$, a turret with a diameter of ≈ 10 μm starts forming in the center of the spot as a consequence the progressive ablation of the irradiated area. Moreover, the formation of rudiments of radial ripple structures can be recognized in some regions, meanwhile the outer area still presents randomly distributed structures.

As N increases, the generation of warm-like ripples with a radial spatial distribution is enhanced, as demonstrated in Fig. 6.1. In particular, the characteristic length of the ripples increases with N, passing from few μm at $N = 50$ to several tens of μm at $N = 200$. This suggests that as N increases, the short warm-like ripples progressively connect together and eventually form the longer ones. The typical spacing between neighbor ripples is within a range of (0.8 ± 0.1) μm and their spatial distribution is orthogonal to the local laser polarization, as typically observed for low spatial frequency LIPSS. In order to confirm the polarization dependence of surface structuring, we processed silicon surface with three types of polarization, i.e. azimuthal, radial and spiral. In all cases, we observed that the produced low spatial frequency LIPSSs are orthogonal to the incident laser polarization as shown in Fig. 6.2. Moreover, the ripples are decorated by nanostructures and NPs, forming a complex hierarchical arrangement. Interestingly, the central turret becomes densely covered with an assembly of NPs, as shown in Fig. 6.1 with $N \geq 50$. This observation agrees with recent reports [26, 27], in which a more complex 4-f system arrangement and spatial light

modulators were exploited to generate the vortex beam and induce 2-dimensional ripples microstructures on Si and steel at a fixed number of pulses (N = 100), then proposing it as a direct verification of the beam polarization distribution.

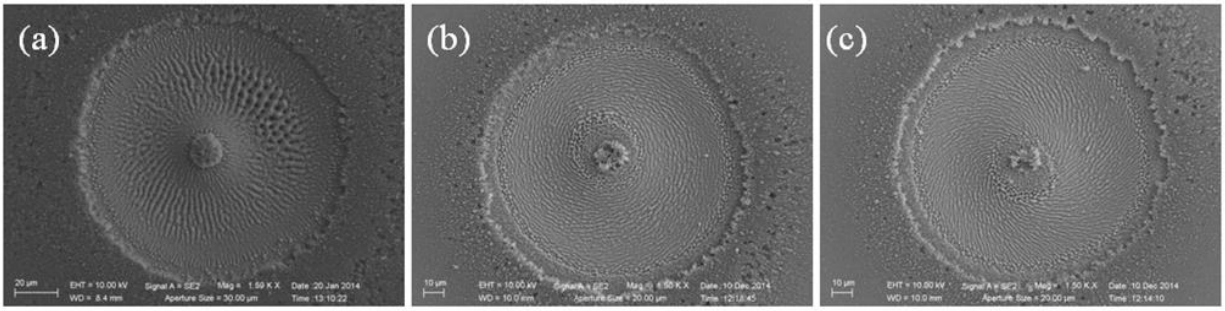

Figure 6.2: SEM micrographs of the processed silicon surface with N = 200, and for different laser polarization. (a) Azimuthal Polarization (b) Radial Polarization (c) Spiral Polarization.

The lower panel in Fig. 6.1 shows the further evolution of the surface morphology at larger values of N, namely, N = 500 and N = 1000. These SEM monographs show the complex structure of the irradiated area. A deep crater is formed at such a high values of N presenting different nanostructured regions. Going from the crater periphery towards the center, one can observe a shallow rim at the crater edge mainly formed by a dense carpet of NPs. This is followed by sharp wall and, then, by an annular region at the bottom of the crater that has developed into a more complex morphology. In particular, the long ripples start decomposing into smaller microstructures, as clearly visible in the top-right corner of the crater at N = 500. These microstructures cover the whole crater base for N = 1000. Finally, an upward directed micro-needle is present at the very center of the crater, whose top is fully decorated by a cauliflower-like structure of assembled NPs.

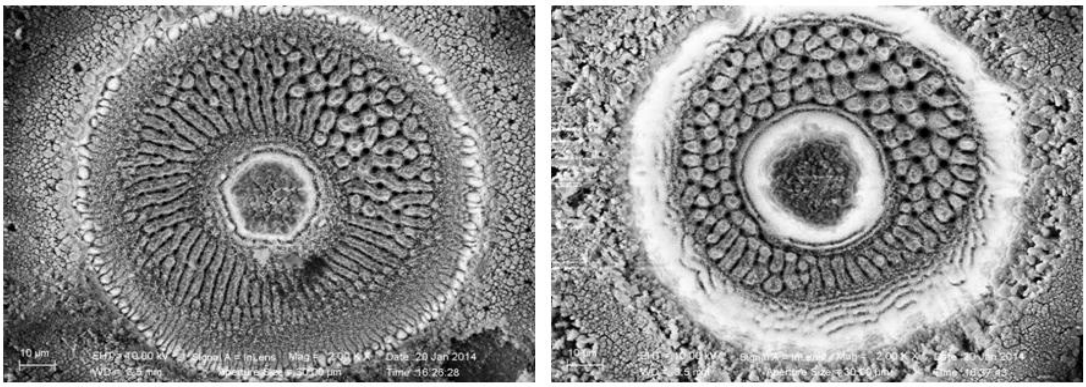

Figure 6.3: The IL mode SEM micrograph of the processed silicon surface with N = 500 (left) and N = 1000 (right). ***P*** = Azimuthal, in both cases.

Fig. 6.3 reports a SEM micrograph registered by using an In-Lens (IL) detector. It is located inside the electron column of the microscope and arranged rotationally symmetric around the optical axis. Due to a magnetic field at the pole piece, the secondary electrons are collected with high efficiency. In particular, at low voltages and small working distances, images with high contrast can be obtained. The image of the IL detector contains more surface information than would be possible to get with the standard Everhardt-Thornley detector. The left IL micrograph well illustrates the ripples structure at high number of pulses (N = 500). One can observe that: (i) neighbor ripples are separate by deep voids, with sub-micron bridges connection; (ii) the lateral outlines of the ripples are rather jagged; (iii) several NPs are distributed on the ripples surface; and (iv) some bifurcations in the ripple structures are present. The right IL micrograph (N = 1000) shows columnar microstructures with typical sizes of 2–3 μm, characterized by a finer nano-structural texture. These columnar structures also present connections. Moreover, in both cases, the microstructures seem composed by different layers at diverse depths, suggesting that the observed morphology is the result of a progressive, cumulative effect related to the interaction of the incoming laser radiation with the structure formed by the previous *(N-1)* pulses.

Various mechanisms have been considered to explain the formation of the low frequency ripples on silicon irradiated with Gaussian beams of fs duration [28-31], but no general consensus has been reached [29, 30]. In many cases, Surface Plasmon Polariton (SPP) formation is considered to explain ripple formation in silicon, as its metallic behavior at high-temperature allows excitation of plasmon waves [22-25, 32]. Localized surface plasmon waves can also be excited by defects (e.g., NPs), surface roughness, and near-wavelength structures already present on the target. Moreover, the possible influence of self-organization from instabilities induced by the ablation process, hydrodynamic effects, and surface roughness interpulse feedback phenomena have been also pointed out recently [33-35]. The most part of these studies regard the ripples formed with a low number of pulses ($N \leq 10$), and a Gaussian spatial intensity profile. However, the Gaussian profile gives rise to ripples in different regions of the spot at different pulse numbers, which makes more difficult a clear identification of their evolution with N.

Figure 6.4 reports a typical SEM micrograph of the Cu sample surface after irradiation with N = 1, at F = 1.4 J/cm^2. Figure 6.4(a) shows that the laser irradiation modifies the target surface in a ring-shaped region, with an almost unaffected central area within a radius $r \leq 6$ μm and an external radius of $\approx$45 μm, thus reflecting the vortex beam spatial intensity profile. Some residue of the

mechanical polishing can also be observed as long sub-micrometer tracks in Figure 6.4(a). The irradiated region presents a corrugated surface characterized by a rather complex network of nanometer scale ridges, wrinkles, pores, and cavities, as illustrated by the SEM micrographs of selected zones acquired at increasing magnification and shown in the panels (b), (c), and (d) of Figure 6.4. In Figure 6.4(d), the inset (e) reports a typical SEM image of a 2×2 μm^2 region of the pristine target surface (same magnification as for panel (d)). Different types of nascent nanostructures can be identified in the complex, cellular network generated on the target surface, some of which are indicated in Figure 2(d). The network connections have a typical thickness of 50–100 nm, and their length between two extreme junction points (bridge) spans from ≈200 nm to ≈700 nm. The network connections form a number of different random structures that include small pores, with diameters in the range 50–150 nm, and large cavities (delimited by rims) of various shape, whose typical sizes range from 300 to 700 nm. Few nanometric protrusions are also observed, which extend for ≈100 nm towards the inside of a nearby cavity. The formation of rather similar structures has been observed earlier in single-shot fs laser nanostructuring of various metals (e.g., copper, gold, platinum, titanium) in the center of irradiated Gaussian beam spot [30, 36]. In the present case, this nanostructure is present over the complete annular beam spot, probably due to a more homogeneous distribution of the energy of the optical vortex beam. Besides, several dispersed NPs can be seen out of the irradiated area. These are NPs produced during the laser ablation process [37, 38], and re-deposited back on the target surface, around the irradiated area, by a backward flux [20, 30, 39].

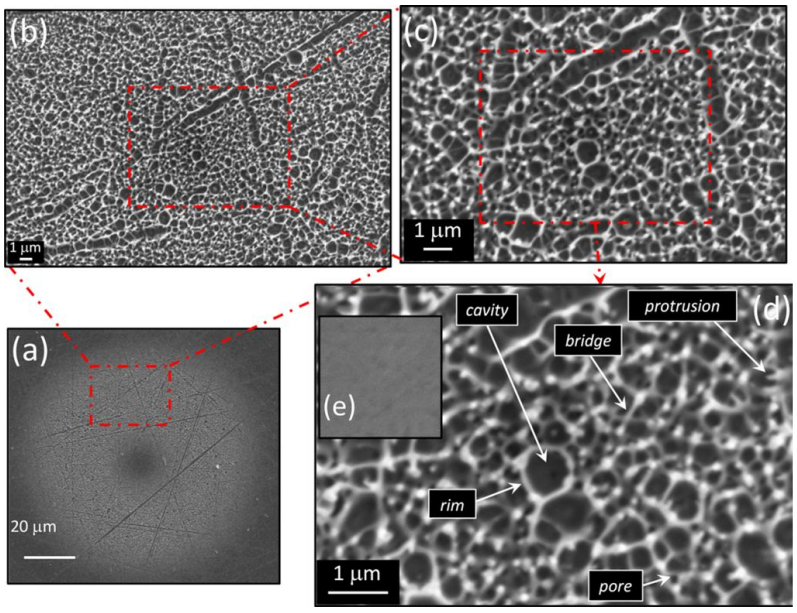

Figure 6.4: Typical SEM micrographs of the copper sample surface after irradiation with N = 1 laser pulse, at F = 1.4 J/cm^2. In clockwise order, the images show: (a) the characteristic laser-modified annular region reflecting the beam shape; (b)–(d) SEM micrographs of the areas indicated by the dashed-dotted boxes at increasing magnification. Inset (e) reports a typical SEM image of a 2 × 2 μm^2 region of the unprocessed target surface with same magnification of panel (d). In panel (d), labels indicate the different types of nascent nanostructures identifiable in the complex, cellular network generated on the target surface.

Various mechanisms have been suggested to rationalize the formation of nanostructures on metallic targets, but no clear understanding has been reached yet [29, 30]. Some of these mechanisms are related to the complex dynamics followed by the melted layer produced by the laser irradiation, which can eventually lead to the formation of nanometer-sized cavities, rims and protrusions on the target surface [30, 40-43]. Approaches based on Molecular Dynamics (MD) simulations have been proved capable of delivering a rather detailed description of the relaxation dynamics of a target irradiated by an ultrashort laser pulse [43-49]. MD results for different metallic targets showed striking similarities suggesting rather general characteristics of the underlying processes. For fs laser pulses, relaxation of laser heated metallic targets occurs in a regime of inertial stress confinement, because both the laser excitation and the energy transfer from electrons to lattice take place before any significant expansion of the irradiated material. In such a regime, the development of tensile stresses induced by the fast expansion of the excited material can trigger cavitation processes and voids formation in the metastable liquid layer produced during the ablation process [42, 43]. Recently, Wu and Zhigilei carried out large-scale MD simulations accounting for the various effects of laser-induced stresses on material relaxation and ejection mechanisms in the condition of stress confinement [43]. Their findings clearly evidence the formation and growth of many voids in the deeper subsurface layers of the target. This leads to the generation of a cellular, foamy, and porous structure in the metastable liquid, with many interconnected regions resembling a "Swiss-cheese-like" configuration. The subsequent cooling of the non-ablated region of the liquid layer can freeze these structures, thus leading to a complex, nanostructured surface morphology as that exemplified in Figure 6.4.

Figure 6.5 reports typical SEM micrographs for low pulse numbers, i.e., N = 2, 5, and 10. In Figure 6.5, panel (a) shows the annular spot on the target for N = 2, while panel (b) illustrates the details of the generated nanostructure morphology. For comparison, in Figures 6.5(a) and (b), the insets display a portion of the surface structure for N = 1, registered at the same magnification. The SEM micrographs for N = 2 clearly indicate that one additional pulse is already able to significantly change the surface structure morphology. In particular, the surface density of inter-connecting bridges reduces, meanwhile the typical dimension of ridges and cavities increases; ridge thickness is in the range ≈200–400 nm and typical sizes of the cavities varies in the interval ≈200–1000 nm. In addition, several spherical dips with typical dimensions in the range ≈200–400 are present in the nanostructure. Moreover, numerous NPs with diameter of ≈50–100 nm are present both in the nano-

cavities and on the nano-ridges, as indicated in Figure 6.5(b) by the yellow and blue arrows, respectively. Figures 6.5(c)–(e) report SEM images of the surface morphology for N = 2, 5, and 10, respectively, illustrating the progressive evolution of the surface nanostructures with N, in the low pulse number regime. One can see that randomly branched nanostructures characterize the surface, and their surface density gradually decreases with the number of pulses.

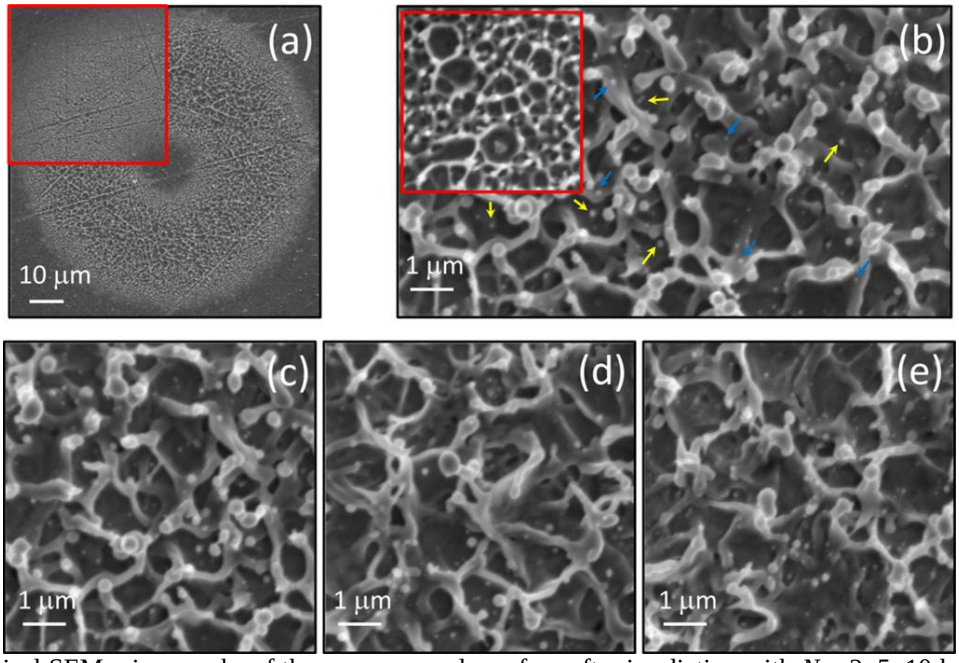

Figure 6.5: Typical SEM micrographs of the copper sample surface after irradiation with N = 2, 5, 10 laser pulses, at F = 1.4 J/cm^2. Panels (a) and (b) reports SEM micrographs for N = 2, registered at two different magnifications, showing: (a) the characteristic laser-modified annular region for N = 2 and (b) its nanostructured morphology. The insets in (a) and (b) report a portion of the target for N = 1, at the same magnification, for comparison. Panels (c), (d) and (e) show the surface morphology for N = 2, N = 5 and N = 10, respectively. In panel (b), yellow and blue arrows indicate some nanoparticles located in the nanocavities and on the nano-ridges, respectively.

It is worth observing that for $N > 1$, the n-th laser pulse of the ablation sequence interacts with the nanostructured surface developed by the previous (n - 1) pulses, which can influence the actual target surface absorption. Vorobyev and Guo showed that the target surface modification induced by multipulse, fs laser ablation with a Gaussian beam enhances its absorptance [50]. In particular, a steep increase by a factor ≈2-3 with respect to the clean metallic target surface occurs after the first pulse, then remaining almost constant for N up to ≈10. This behavior was ascribed to surface nanoscale roughness induced by laser ablation at low number of pulses. A similar effect is also likely in the case of fs laser ablation with optical vortex beams: after the first laser pulse, the ablation process is more effective because of the increased amount of energy coupled to the nanostructured target. The associated increase of the plasma plume pressure [51] can explain the

increased number of NPs re-deposited within the laser beam spot and decorating the surface nanostructures. Moreover, a reduction of the nanostructure surface density with the number of pulses was also reported earlier for Gaussian beams and can be ascribed to inhomogeneous energy absorption driven by the surface roughness [30, 36].

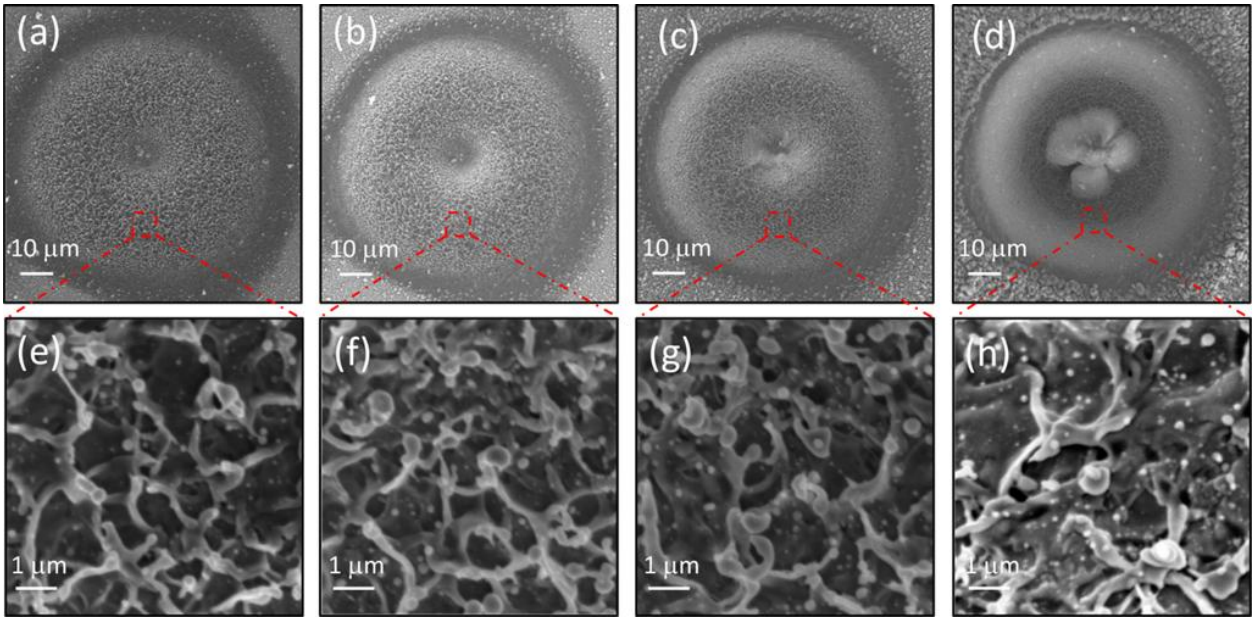

Figure 6.6: Typical SEM micrograph of the copper sample surface after irradiation with (a)–(e) N = 40, (b)–(f) N = 100, (c)–(g) N = 200, and (d)–(h) N = 500, at F = 1.4 J/cm^2. The upper panels show SEM micrograph of the laser-modified annular region; the lower panels report SEM micrographs of the area indicated by the dashed-dotted box, registered at larger magnification, illustrating the typical surface morphology.

Figure 6.6 reports typical SEM micrograph of the Cu sample surface after irradiation with medium number of pulses, i.e. (a)–(e) N = 40, (b)–(f) N = 100, (c)–(g) N = 200, and (d)–(h) N = 500, at F = 1.4 J/cm^2. In particular, Figures 6.6(a)–(d) illustrate the typical surface morphology of the laser modified annular region and its close periphery, while the lower panels report SEM images of the area indicated by the dashed-dotted box, registered at larger magnification, demonstrating the nanostructured morphology of the annular irradiated area. For N = 40, and N = 100 (see Figure 6.6, panels (a) and (b)), the shallow ablated crater shows a morphological structure similar to that observed for lower number of pulses, thus resembling the optical vortex beam intensity profile. The nanostructure morphology of the crater bottom reported in Figures 6.6(e) and 6.6(f) mainly consists of several random micro-branches, with nanometer-size thickness, and odd shaped cavities decorated with nanoparticles. By increasing the number of pulses to N = 200 and, then, to N = 500, a deeper crater is progressively drilled. Crater drilling is typically accompanied by the formation of side walls and by the progressive reduction of the dimension of the bottom region with respect to

the crater entrance area, as evidenced in Figures 6.6(c) and 6.6(d). As illustrated in Figures 6.6(g) and 6.6(h), the crater bottom shows a morphology similar to that observed for lower number of pulses. Interestingly, also the central turret left in the singular region of the optical vortex beam for a low number of pulses starts structuring as N increases.

Figures 6.7 (a)–(c) report the evolution of the crater morphology as N further increases, showing that the central structure is progressively wrecked (panel (b), N = 1000), and eventually a hole without any residual central part is drilled for N = 2000 (panel (c)). This can be ascribed to multiple reflections on the crater external wall that guiding laser light towards the center of the ring-shaped beam area promote laser energy absorption and ablation in the central region [52], which eventually results in the gradual structuring even in the singular part of the vortex beam.

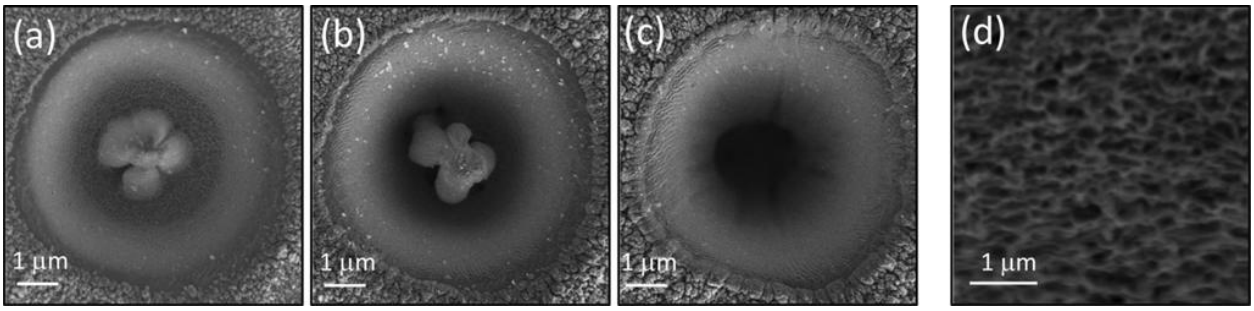

Figure 6.7: SEM micrographs of the ablation crater after irradiation with (a) N = 500, (b) N = 1000, and (c) N = 2000, at F = 1.4 J/cm^2. Panel (d) reports a SEM image of a portion of the crater external wall, showing its characteristic nanometer-scale, filamentary corrugation.

It is worth noticing that the central structure of Fig. 6.7(a) can be delimited by a circle with a radius of ≈16 μm, which is about 3 times larger than R_{in} (≈6 μm), the typical radius of both the central turret observed at lower number of pulses, and the singular beam area with zero intensity. This suggests a progressive accumulation of ablated material around the turret during crater drilling, for 100 < N < 1000. This observation can be contrasted with micro-needle fabrication on a Ta metal surface based on laser ablation with a nanosecond (ns) optical vortex beam [9]. For ns pulses, a central needlelike structure forms in the center of the vortex beam and extends for several microns out of the pristine target surface, after only four pulses. This is ascribed to accumulation of laser ablation plasma material at the center of the processed surface [9]. Instead, for optical vortex, fs pulses used in the present study, many laser pulses (N ≈ 100) are needed to produce a turret in the center of the ablation crater because of the lower ablation rate per pulse of fs ablation. This progressively transforms into a micro-tip with a nanostructured surface for 200 < N < 1000, and eventually disappears at still larger number of pulses.

6.4 Conclusive Remarks

The optical vortex beams generated by a *q*-plate were usefully exploited to fabricate different, surface micro- and nano-structures on Si and Cu targets. In both cases, the morphological characteristics of the surface structures change with the pulse number, *N*, evidencing a clear cumulative effect. Nevertheless, as *N* increases, for Si the structures change from a rough surface to rudiments of ripples and, then, to ordered ripples, prevalently oriented in a direction orthogonal to the laser polarization, eventually transforming into columnar structures for $N \approx 1000$. Instead, for Cu the surface always presents a rather complex texture, without ordered structures, at the laser fluence used. Interestingly, in both cases the center of the laser spot, corresponding to the central singular region of the vortex beam with nearly zero intensity, develops into a micro-tip like form, which presents different characteristics for Si and Cu. While a turret whose top is decorated with a cauliflower-like NPs assembled structure occurs for Si, the central structure formed in Cu resembles a slightly asymmetric mountain peak surrounded by four inclines degrading toward the rough nanostructured crater bottom.

In conclusion, our results on Si and Cu demonstrate that fs vortex beams generated by a *q*-plate can produce very interesting morphologies at the micro- and nano-scale, which are not usually achieved with the more standard Gaussian beams. This aspect deserves further investigations fully exploring the possibilities offered by this novel method in fs direct laser surface structuring.

References

[1] L. Allen, M. W. Beijersbergen, R. J. C. Spreeuw, and J. P. Woerdman, Phys. Rev. A 45(11), 8185–8189 (1992).

[2] J. P. Torres and L. Torner (Eds.), *Twisted Photons, Applications of Light with Orbital Angular Momentum* (Wiley, 2011)

[3] L. Marrucci, C. Manzo, and D. Paparo, Phys. Rev. Lett. 96, 163905 (2006).

[4] T. Kuga, Y. Torii, N. Shiokawa, T. Hirano, Y. Shimizu, and H. Sasada, Phys. Rev. Lett. 78(25), 4713–4716 (1997).

[5] K. T. Gahagan, and G. A. Swartzlander, Jr., "Optical vortex trapping of particles," Opt. Lett. 21(11), 827–829 (1996).

[6] L. Paterson, M. P. MacDonald, J. Arlt, W. Sibbett, P. E. Bryant, and K. Dholakia, Science 292(5518), 912–914 (2001).

[7] A. Mair, A. Vaziri, G. Weihs, and A. Zeilinger, Nature 412(6844), 313–316 (2001).

[8] Junichi Hamazaki, Ryuji Morita, Keisuke Chujo, Yusuke Kobayashi, Satoshi Tanda, and Takashige Omatsu, Opt. Express 18(3), 2144 (2010).

[9] Takashige Omatsu, Keisuke Chujo, Katsuhiko Miyamoto, Masahito Okida, Kazuki Nakamura, Nobuyuki Aoki, and Ryuji Morita, Opt. Express 18(17), 17967 (2010).
[10] Kohei Toyoda, Katsuhiko Miyamoto, Nobuyuki Aoki, Ryuji Morita, and Takashige Omatsu, Nano Lett., 12, 3645 (2012).
[11] Kohei Toyoda, Fuyuto Takahashi, Shun Takizawa, Yu Tokizane, Katsuhiko Miyamoto, Ryuji Morita, and Takashige Omatsu, PRL 110, 143603 (2013).
[12] Cyril Hnatovsky, Vladlen G. Shvedov, Wieslaw Krolikowski, and Andrei V. Rode, Optics Letters 35, 3417(2010).
[13] K. K. Anoop, A. Rubano, R. Fittipaldi, X. Wang, D. Paparo, A. Vecchione, L. Marrucci, R. Bruzzese, and S. Amoruso, Applied Physics Letters 104, 241604 (2014).
[14] K. K. Anoop, R. Fittipaldi, A. Rubano, X. Wang, D. Paparo, A. Vecchione, L. Marrucci, R. Bruzzese, and S. Amoruso, Journal of Applied Physics 116, 113102 (2014).
[15] S. Slussarenko, A. Murauski, T. Du, V. Chigrinov, L. Marrucci, and E. Santamato, Opt. Express 19, 4085 (2011).
[16] F. Cardano, E. Karimi, S. Slussarenko, L. Marrucci, C. de Lisio, and E. Santamato, Appl. Opt. 51, C1 (2012).
[17] X. Ni, K. K. Anoop, X. Wang, D. Paparo, S. Amoruso, and R. Bruzzese, Appl. Phys. A 117 (1), 115 (2014).
[18] K.K. Anoop, Xiaochang Ni, M. Bianco, D. Paparo, X. Wang, R. Bruzzese, S. Amoruso, Appl. Phys. A 117 (1), 313 (2014).
[19] S. Amoruso, R. Bruzzese, N. Spinelli, R. Velotta, M. Vitiello, X. Wang, G. Ausanio, V. Iannotti, and L. Lanotte, Appl. Phys. Lett. 84, 4502 (2004).
[20] A. Pereira, P. Delaporte, M. Sentis, W. Marine, A. L. Thomann, and C. Boulmer-Leborgne, J. Appl. Phys. 98, 064902 (2005).
[21] S. Amoruso, R. Bruzzese, N. Spinelli, R. Velotta, M. Vitiello, and X. Wang, Europhys. Lett. 67, 404 (2004).
[22] J. Bonse, K.-W. Brzezinka, and A. J. Meixner, Appl. Surf. Sci. 221, 215 (2004).
[23] J. Bonse, S. Baudach, J. Kr€uger, W. Kautek, and M. Lenzner, Appl. Phys. A: Mater. Sci. Process. 74, 19 (2002).
[24] X. Jia, T. Q. Jia, N. N. Peng, D. H. Feng, S. A. Zhang, and Z. R. Sun, J. Appl. Phys. 115, 143102 (2014).
[25] J. Bonse, A. Rosenfeld, and J. Kruger, J. Appl. Phys. 106, 104910 (2009).
[26] K. Lou, S.-X. Qian, X.-L. Wang, Y. Li, B. Gu, C. Tu, and H.-T. Wang, Opt. Express 20, 120 (2012).
[27] Y. Jin, O. J. Allegre, W. Perrie, K. Abrams, J. Ouyang, E. Fearon, S. P. Edwardson, and G. Dearden, Opt. Express 21, 25333 (2013).
[28] Laser Precision Microfabrication, edited by K. Sugioka, M. Meunier, and A. Piqué (Springer, Heidelberg, 2010).
[29] K. Sugioka and Y. Cheng, Light: Sci. Appl. 3, e149 (2014).
[30] A. Y. Vorobyev and C. Guo, Laser Photonics Rev. 7, 385 (2013).

[31] E. G. Gamaly and A. V. Rode, Prog. Quantum Electron. 37, 215 (2013).
[32] T. J.-Y. Derrien, T. E. Itina, R. Torres, T. Sarnet, and M. Sentis, J. Appl. Phys. 114, 083104 (2013).
[33] J. Reif, O. Varlamova, S. Varlamov, and M. Bestehorn, AIP Conf. Proc. 1464, 428 (2012).
[34] G. D. Tsibidis, M. Barberoglou, P. A. Loukakos, E. Stratakis, and C. Fotakis, Phys. Rev. B 86, 115316 (2012).
[35] J. Z. P. Skolski, G. R. B. E. Romer, J. Vincenc Obona, and A. J. Huis in 't Veld, J. Appl. Phys. 115, 103102 (2014).
[36] A. Y. Vorobyev and C. Guo, Opt. Express 14, 2164 (2006).
[37] S. Amoruso, G. Ausanio, R. Bruzzese, M. Vitiello, and X. Wang, Phys. Rev. B 71, 33406 (2005).
[38] S. Eliezer, N. Eliaz, E. Grossman, D. Fisher, I. Gouzman, Z. Henis, Y. Horovitz, M. Frankel, S. Maman, and Y. Lereah, Phys. Rev. B 69, 144119 (2004).
[39] A. Pereira, A. Cros, P. Delaporte, S. Georgiou, A. Manousaki, W. Marine, and M. Sentis, Appl. Phys. A 79, 1433 (2004).
[40] E. Stratakis, V. Zorba, M. Barberoglou, C. Fotakis, and G. A. Shafeev, Nanotechnology 20, 105303 (2009).
[41] T. Y. Hwang, A. Y. Vorobyev, and C. Guo, Appl. Phys. Lett. 95, 123111 (2009).
[42] V. V. Zhakhovskii, N. A. Inogamov, and K. Nishihara, JETP Lett. 87, 423 (2008).
[43] C. Wu and L. V. Zhigilei, Appl. Phys. A 114, 11 (2014).
[44] D. Perez and L. J. Lewis, Phys. Rev. Lett. 89, 255504 (2002).
[45] D. S. Ivanov and L. V. Zhigilei, Phys. Rev. Lett. 91, 105701 (2003).
[46] S. Amoruso, R. Bruzzese, X. Wang, N. N. Nedialkov, and P. A. Atanasov, J. Phys. D: Appl. Phys. 40, 331 (2007).
[47] L. V. Zhigilei, Z. Lin, and D. S. Ivanov, J. Phys. Chem. C 113, 11892 (2009).
[48] N. Tsakiris, K. K. Anoop, G. Ausanio, M. Gill-Comeau, R. Bruzzese, S. Amoruso, and L. J. Lewis, J. Appl. Phys. 115, 243301 (2014).
[49] S. Amoruso, N. N. Nedyalkov, X. Wang, G. Ausanio, R. Bruzzese, and P. A. Atanasov, Thin Solid Films 550, 190 (2014).
[50] A. Y. Vorobyev and C. Guo, Phys. Rev. B 72, 195422 (2005).
[51] T. Donnelly, J. G. Lunney, S. Amoruso, R. Bruzzese, X. Wang, and X. Ni, J. Appl. Phys. 108, 043309 (2010).
[52] Q. Zhan, Adv. Opt. Photon. 1, 1 (2009).

Chapter 7

Summary and Future Directions

This thesis reports a detailed investigation of laser ablation of solid targets with femtosecond (fs) pulses, focusing on three prominent aspects: 1) spatial and temporal evolution of the laser produced plume (LPP), in high vacuum condition; 2) nanoparticle (NP) generation in high vacuum and applications of NPs-assembled films in material science; 3) surafce micro/nanostructure formation, in ambient condition. Most of the experiments were carried out exploiting pure copper and silicon targets, and some of the results were compared with other metals as well. The first two investigations were performed with a standard, fs laser beam with Gaussian intensity profile. Instead, material surface structuring was carried out with spatially shaped optical vortex pulses, which is a topic of recent increasing interest in the field of laser ablation. Hereafter, I report an overall summary of the research activity carried out during my PhD and illustrate some possible future directions of fs laser ablation.

7.1 Summary

This thesis reports a comprehensive study on fs laser ablation of a pure copper target with 800 nm, ≈50 fs, Ti:Sapphire laser pulses. The experimental analysis mainly focuses on the spatial and temporal evolution of atomic and NP components in the LPP, by exploiting spectrally resolved time-gated imaging and charge collection techniques, and the features of the NP generation process. The temporal evolution of neutral (Cu*), and ionic (Cu^+) components of the plume were separately imaged by exploiting bandpass interference filters, while the NP component was investigated by collecting their characteristic broadband emission. Meanwhile, charge collection analysis was accomplished by using Langmuir probe and Faraday cup detectors.

The study was carried out at a moderate (0.5−10 J/cm^2) and a high fluence (0.5–75 J/cm^2) regime. Moreover, similar behavior was observed in some experiments carried out on a silicon target, indicating a rather general character of the observed features. The analysis of the LPP clearly showed the presence of a sizeable population of fast ions flying ahead of the main neutral component, which becomes still more marked for the high fluence case. A simple model indicated that the formation of the fast ion component can be explained in terms of a dynamic ambipolar diffusion process occurring in the early stage of the LPP formation. The fluence dependence of ion yield showed the presence of three different regimes. A first transition occurred at about 5-6 J/cm^2

and a maximum in the specific ion yield was observed at such fluence. The first two regimes (i.e. from ablation threshold up to a fluence $F \approx 50$ J/cm^2) were rationalized in the frame of the two-temperature model description of the fs laser-target interaction and subsequent material decomposition mechanisms. The transition occurring at higher fluence ($F \approx 50$ J/cm^2) was ascribed to the progressive passage towards a high-intensity LPP generation, where other complex mechanisms start playing a role.

The angular distribution of the ion flux was investigated, showing that it is well described by an adiabatic and isentropic model of plume expansion and that the ion flux narrows as the laser pulse fluence increases. Moreover, the ion average velocity reaches values of several tens of km/s, evidencing the presence of ions with kinetic energy of several hundred eV. The fluence dependence of the copper ions angular distribution was also analyzed, observing a gradual increase in forward peaked Cu ions for fluences up to ≈10 J/cm^2. The progressive formation of a broader ion component was observed at larger angles for fluences larger than ≈10 J/cm^2.

Finally, an experimental characterization of the ionic angular distribution for several metallic targets (Mg, Al, Cr, Fe, Cu, and W) was carried out at a relatively high fluence of ≈66 J/cm^2. Interestingly, the ion emission from the volatile metals showed a narrow, forward-peaked distribution, and a high peak ion yield compared to the refractory metals, evidencing some interesting effects related to the physical characteristics of the elemental target atoms on the LPP expansion dynamics.

As for the NP component produced during fs laser ablation, a combined theoretical and experimental analysis of the process of NPs generation from a bulk copper target with ≈50 fs, 800 nm pulses, in an interval of laser fluencies going from ≈2×F_{th} to ≈20×F_{th}, was carried out. On one side, molecular dynamics simulations, with two-temperature model, allowed describing the decomposition of the material through the analysis of the evolution of thermodynamic trajectories in the material phase diagram, and estimating the size distribution of the generated nanoaggregates. On the other side, atomic force microscopy of less than one layer NPs deposits on witness plates, and fast imaging of the NP plume broadband optical emission provided the corresponding experimental characterization. Both experimental and numerical findings agreed on a size distribution characterized by a significant fraction (≈90%) of small nanoparticles, and a residual part (≈10%) spanning over a rather large size interval, evidencing a weak dependence of the NPs sizes on the laser pulse fluence. Moreover, NP generation was used to fabricate NPs-assembled

films for applications in the field of bio-sensing via deposition of gold NPs on a quartz crystal microbalance electrode, and in photoelectrochemical cells (PEC) via deposition of TiO_2 NPs on a photoanode.

As for laser surface structuring, fs laser interaction with silicon and copper targets using optical vortex beams, generated by a *q*-plate, was investigated. Here, the variation of the produced surface structures was analyzed as a function of the number of incident laser pulses, *N*, and laser polarization, ***P***, at a laser fluence slightly above the ablation threshold value. As *N* increased, the structures passed from a rough surface to rudiments of ripples and, then, to ordered ripples, eventually transforming into columnar structures for $N \approx 1000$. Interestingly, the center of the laser spot, corresponding to the central singular region of the vortex beam with nearly zero intensity, developed into a micro-needle with a cauliflower-like NPs assembled structure on the top. Our experimental findings suggest the importance of a cumulative effect on the formation of periodic ripples (on silicon) and interesting micro/nano patterns (on copper) which are not achievable by the more standard beams with Gaussian intensity profile.

7.2 Future Directions

Future studies on fs laser ablation offer a number of opportunities related to a deeper understanding of the intriguing, fundamental mechanisms and to its possibilities in a variety of applications. In chapter 4 we have discussed different diagnostic methods to analyze the fs laser produced plume in a wide range of laser intensities going from 1.6×10^{13} to 2.2×10^{15} W/cm^2. The spectrally resolved ICCD imaging method, currently applied to fs LPP of copper and silicon, can be applied to other samples as well with a suitable selection of band-pass interferometric filters. The analysis of the fluence dependence of ion yield showed the presence of three different regimes. In particular, the high intensity regime is still seldom investigated. In order to clarify the material characteristics like absorption, reflection etc. in the intense field, especially at intensity $>10^{15}$ W/cm^2, more fs laser ablation experiments and theoretical models should be developed. The fluence dependence of the copper ions angular distribution was also analyzed, a broader ion component was observed at larger angles for fluences larger than ≈10 J/cm^2, indicating that a well suited model is required to explain plume shape and evolution in the high intensity regime.

In chapter 5, we have investigated both experimentally and theoretically the role of laser pulse fluence on expansion dynamics and size distribution of the NPs produced by irradiating a metallic target with an ultrashort laser pulse in a vacuum. The NP size distribution remains essentially the

same in our investigated regime of laser fluence from ≈2×F_{th} to ≈20×F_{th}. For instance, contradictory experimental results and theoretical predictions exist about the role of the laser pulse fluence on the process of NPs generation, and their final properties (as for example the NPs size and size distribution, the amount of material which decomposed into NPs, etc.), and more research has to be still done to further clarify the current scenario. Moreover, NPs size distribution in a wider range of intensity regimes is an issue which has not yet fully explored. The average size of NPs observed in our experiments is ≈10-15 nm, and the NP-assembled films using fs laser ablation have been utilized in bio-sensing and PEC applications. Results suggest an improved sensitivity compared to standard methods. The higher surface to volume ratio of NPs-assembled films obtained with fs laser ablation can be also utilized in other applications.

In chapter 6, the ablation and subsequent material surface structuring using fs optical vortex pulses was reported. This is a hot topic with numerous applications in material processing. Most of the works reported in this field since 2010 are with nanosecond vortex beams and the same with fs pulses are still in its infancy. A *q*-plate was used to generate an optical vortex beam with fs pulse duration through spin-to-orbital conversion of the angular momentum of light. The *q*-plate is a new optical device with more flexibility (*q*-value) to change the orbital angular momentum of a laser beam. Here, the variation of the produced surface structures was investigated as a function of the number of incident laser pulses, *N*, and laser polarization, *P*, at laser fluences slightly above the ablation threshold value. More work has to be done to clarify the effect of laser fluence, *q*-value, material properties, and ambient conditions on the final surface structure, and underlying formation mechanisms.

Appendix

A. Chirped Pulse Amplification (CPA) and Single Shot Autocorrelator (SSA)

Introduction of chirped-pulse amplification (CPA) in laser system enabled the latest revolution in production of high peak powers from laser through amplification of very short (femtosecond) laser pulses to pulse energies previously available only from long-pulse lasers. The breakthrough of ultrafast solid-state lasers happened with the discovery of the Ti:Sapphire laser medium which was the first solid-state laser medium that was able to support ultrashort pulses without cryogenic cooling.

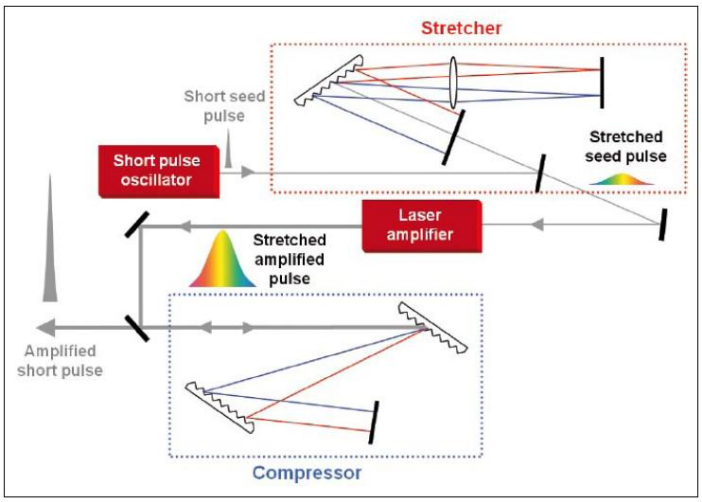

Figure A1: Conceptual schematic of a chirped-pulse amplification-based laser system.

The concept of CPA system is shown in Fig. A1. Reversible manipulation of the temporal characteristics of ultrashort laser pulses is possible if a conjugate set of optical devices termed stretcher (or expander) and compressor is used (see Fig. A1). An inherent property of ultrashort pulses that can be used for their controlled stretching and recompression is their broad spectral bandwidth. Short pulse duration can be achieved only if coherent light consists of a range of wavelengths which are carefully and orderly synthesized – such as the pulses produced by mode-locked lasers. The stretcher operates by introducing large, well-characterized dispersion, i.e. time delay of different spectral components of the ultrashort pulse to produce a long, chirped optical pulse. The compressor operates on the same principle, with dispersion that closely matches that produced by the stretcher, but opposite in sign. Thus the ultrashort pulse initially generated in a mode-locked laser first undergoes stretching in the pulse stretcher (to ps-ns durations),

amplification to high energies in the laser amplifier, followed by compression close to its original pulse duration in the pulse compressor.

A single shot autocorrelator can be used to extract the pulse duration of the amplified beam. The Single shot autocorrelator (Coherent Inc.) is used to measure the second order autocorrelation of amplified ultrafast pulses with durations as short as 30 femtosecond (fs) and as long as 4 picoseconds (ps). The SSA is designed for use over a broad range of energies and wavelength making it well-adapted to a variety of laser systems including Ti:Sapphire, Nd:Glass, Nd:YAG, and dye amplifiers.

In the SSA, the laser pulses are split into two beams, which are then non-collinearly frequency-doubled in a nonlinear crystal (KDP). The relative wavefront tilt produces a spatial time delay in the frequency-doubled signal, resulting in an autocorrelation of the temporal intensity profile of the ultrafast pulse. The autocorrelation signal is detected by a CCD array, which is read out on the standard laboratory oscilloscope.

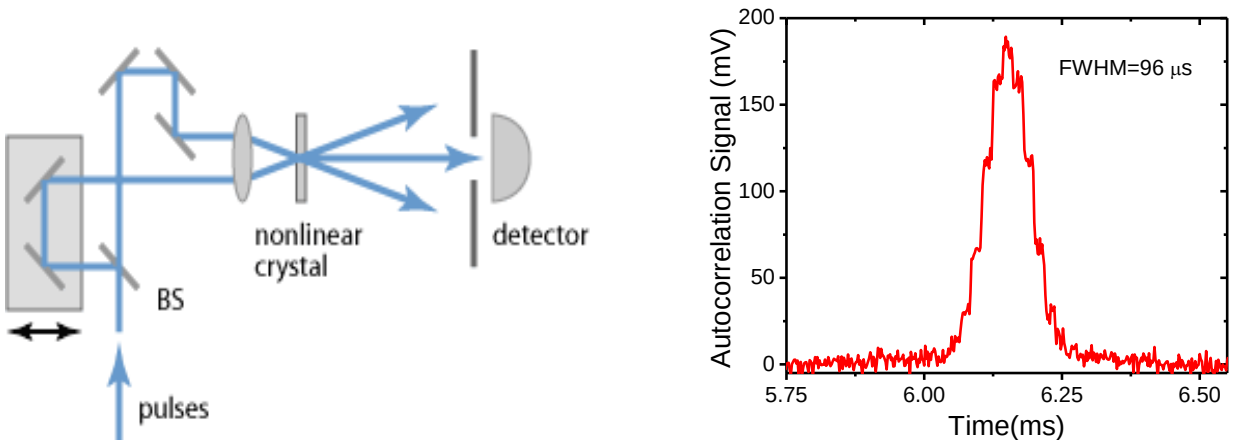

Figure A2: (a) Setup of an intensity autocorrelator. BS = beam splitter. (b) Typical autocorrelation signal of Ti: Sapphire laser pulses with 35 fs pulse duration.

The SSA has two basic modes of operation: femtosecond and picosecond. In femtosecond mode the geometric wavefront tilt introduced by non-collinearly crossing the beam in the crystal is sufficient to measure subpicosecond pulses. In picosecond mode, one of the mirrors is replaced by a diffraction grating, introducing additional wavefront tilt and allowing accurate measurement of pulses with a FWHM of up to 4 ps. In both cases, a variable delay line is included, providing accurate synchronization of the two beams.

B. Atomic Force Microscopy (AFM)

The size characteristics of the deposited NPs were measured by an AFM (Digital Instruments Nanoscope IIIa) in tapping mode. The Nanoscope IIIa is a versatile, high-resolution imaging tool that performs AFM techniques for surface characterization, shapes and sizes. Powerful software and a compact hardware design enable the Nanoscope AFM to easily acquire data from micro- to atomic-scale images. The system's Nanoscope 3D controller can scan from the maximum scan size (100 microns) to a few nanometers with full 16-bit resolution on all scan waveforms and on each axis. Tapping mode is one of several different imaging modes used in atomic force microscopy. AFM is a type of scanning probe microscopy. These microscopes do not use light, as in conventional microscopes, but rather scan a sharp probe over a surface to image extremely small surface structures. With an AFM it is possible to image a surface at 10 nm resolution, and generate a 3D map of the sample surface.

The probe used in an AFM is a sharp tip, typically less than 5 μm tall and often less than 10 nm in diameter at the apex. The tip, typically made from Si_3N_4 or Si, is located at the free end of a cantilever that is usually 100–500 μm long. Forces between the tip and the sample surface cause the cantilever to bend, or deflect. Tapping Mode AFM, the most commonly used of all AFM modes, that maps topography by lightly tapping the surface with an oscillating probe tip. The cantilever's oscillation amplitude changes with sample surface topography. A detector measures the cantilever deflections as the tip is scanned over the sample, or the sample is scanned under the tip. Most AFMs use optical techniques to detect the position of the cantilever. In the most common scheme [Fig. 3.4(b)], a light beam from a laser diode bounces off the back of the cantilever and onto a position-sensitive photo-detector (PSPD). As the cantilever bends, the position of the laser beam on the detector changes. Several forces typically contribute to the deflection of an AFM cantilever. To a large extent, the distance regime (i.e., the tip-sample spacing) determines the type of force that will be sensed.

The measured cantilever deflections allow a computer to generate a map of surface topography by exploiting image analysis software (NanoScope v5.31). After performing deconvolution on each AFM image, in order to avoid the tip size effect, the particles average size in a plane parallel and orthogonal to the substrate can be evaluated. This allows the reconstruction of three-dimensional view of the deposits and its size characterization.

C. Field Emission Scanning Electron Microscope (FESEM)

The vacuum system, electron optics, specimen chamber and stage, and signal detectors are the four major components of any SEM system. The FESEM uses a focused beam of electrons to generate an image or to analyze the specimen. The focused electron beam scans the surface of the specimen. The vacuum is essential to operate the electron gun and to prevent collision of electrons with gas molecules. The pre-vacuum pump and turbo pump evacuate the specimen chamber. In the gun head there is an ultra-high vacuum, which is maintained by ion getter pump. All electron optics occur at the Gemini column, which is the area of the FESEM where electrons are emitted from the Schottky field emitter, accelerated, bundled, focused, and deflected. The main characteristics of Gemini optics are the beam booster and an objective lens that consists of combined electrostatic and electromagnetic lenses. The deflection system consists of a set of scan coils that move the electron beam in a point-to-point scan across the specimen. The scan coil deflect the beam in the X and Y directions relative to the electron-optical axis. The dimensions of specimen chamber is 330 mm inner diameter and 270 mm height. The standard specimen stage is a 5-axis (X, Y, Z, Rotation, and tilt) motorized cartesian stage that is controlled by SmartSEM user software or dual joystick controller.

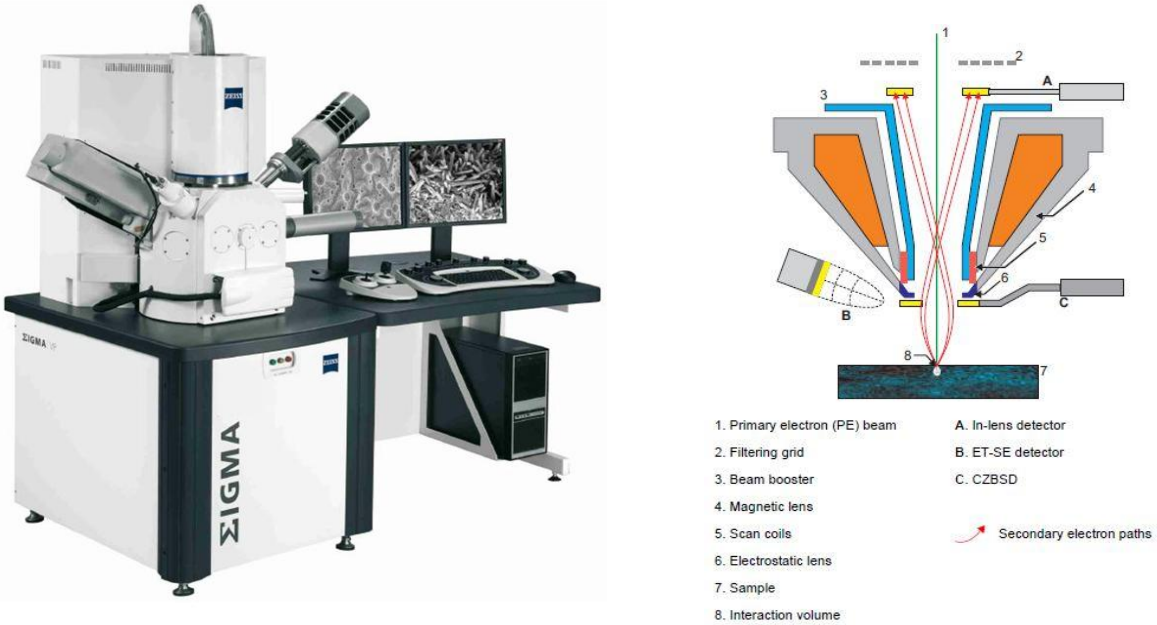

Figure A3: Photograph of a ZEISS SIGMA FESEM system (on left) and alignment of three major electron detectors in the system (on right).

When a primary electron beam hits a sample, certain electron beam interaction processes occur, secondary electrons (SEs) and back scattered electrons (BSEs) are, then, generated. Secondary electrons ejected from the outer atomic shell of the sample material upon impact by the primary electron beam. Secondary electrons have low energy, less than 50 eV. All the electrons with energy higher than 50 eV are known as BSEs. BSEs are generated by elastic scattering in a much deeper range of the interaction volume and carry depth information. Specific types of detectors are able to detect the SEs and BSEs, and the detector signals can be used to create images and produce information about the properties of the sample. Three major detectors used for topography and surface structure are In-lens detector (annular SE detector), ET-SE detector (Everhart-Thornley type), and back scattered electron detector (CZBSD). The main benefit of using an In-lens detector is its high detection efficiency, particularly at very low acceleration voltages, and the almost pure detection of secondary emission electrons. It provides an ideal tool to map the surface of a sample. The ET-SE detector is mounted on the walls of the specimen chamber, which views the specimen laterally and allows detection of secondary electrons with a small backscattered component. When the high energy electrons hit the scintillator layer of ET-SE detector, photons are generated inside the scintillator. These photons are directed out of the vacuum system through a light pipe and are transferred to the photomultiplier tube. The photomultiplier multiplies the flashes of light and outputs a signal that can be used for imaging. Because of its lateral position in the chamber with respect to sample, ET-SE detector provides good surface information. All other detectors (In-lens and BSE) view the sample from above, providing only limited information about specimen's topography. Surface tilted towards the detector provide more surface detail with brighter edges; samples tilted away from the detector display shadowing effects and less surface detail. A signal source commonly used in electron microscopy is the backscattered electron detector (CZBSE). The use of this type of detector makes it possible to effectively display compositional differences in the specimen. One major reason for this ability is the position of the CZBSE detector, which is located below the final lens and views the specimen from above. This position offers a very large solid angle that can be used for the detection of backscattered electrons. Its performance with respect to contrast is based on the backscattered coefficient, which increases with increasing atomic number. If different phases exist on the specimen, those with higher average atomic number display higher brightness than those with smaller atomic number. The positions of three detectors, electron optics are shown in Fig. A3(b) with details.